

Workshop of **Experimental Nuclear and Particle Physics** 2020

12.–18. 01. 2020, Bílý Potok

Faculty of Nuclear Sciences and Physical Engineering
Czech Technical University in Prague

Workshop of Experimental Nuclear and Particle Physics 2020

Editors:	L. Novotný, R. Novotný
Issued by:	Czech Technical University in Prague Faculty of Nuclear Sciences and Physical Engineering
Address:	KF FJFI ČVUT, Břehová 7, 115 19 Praha 1 novotr14@fjfi.cvut.cz, +420731891801

Available at https://indico.fjfi.cvut.cz/event/123/wejcf2020_proceedings.pdf

First edition. 96 pages.

Contents

Observation and measurements of vector-boson scattering at the ATLAS detector Ondřej Penc	1
PBSPro Batch System Zdenek Hubacek	3
RDataFrame Zdenek Hubacek	5
The Forward Diffractive Detector Solangel ROJAS TORRES	8
b-dependent BK in all its beauty Marek Matas	11
Assessment of Various Standard-Model Phenomena Awareness at $t \sim 13.8$ Ga and Non-Vanishing Net-Baryon Density at the WEJCF Experiment - 4th Edition Robert Licenik	14
Proton structure - a short introduction to parton distributions Dagmar Bendová	17
Systematic uncertainty of mass composition of cosmic rays interpreted from measurements of depth of shower maximum using different Monte Carlo generators Karolína Syrokvaš	21
Measurement of Double Differential Jet Substructure in p+p collisions at $\sqrt{s} = 200$ GeV at STAR Georgij Ponimatkin	24
Tips and tricks with RooFit - Tutorial Leszek Kosarzewski	27
Study of $\pi^+\pi^-$ and K^+K^- production in central exclusive processes with the STAR detector at RHIC Tomáš Truhlář	30
Photoproduction of J/ψ in ultra-peripheral collisions David Grund	33
Influence of modified hadronic interactions on properties of cosmic-ray showers Nikolas Denner	36
Heavy-ion collisions and Lambda hyperon polarization Ondřej Lomický	38

Study of charm quark production in jets Jitka Mrázková	41
Study of cold nuclear matter effects with charm mesons Michal Svoboda	44
Muon Forward Tracker for the ALICE upgrade Diana M. Krupova	47
Study of jet substructure in Au+Au collisions with the STAR experiment Monika Robotková	49
European Strategy of Particle Physics 2020 Katarína Křížková Gajdošová	52
STAR Zero Degree Calorimeter Jan Vaněk	55
Jet evolution Josef Bobek	58
Anisotropic flow measurements with the ALICE experiment Daniel Mihatsch	61
Performance of the upgraded electronics for Cherenkov and scintillator detectors of the Pierre Auger Observatory Margita Majerčáková	64
Measurement of HBT radii in 1.23A GeV Au+Au collisions from UrQMD simulations Jakub Štěrba	67
Complexity out of simplicity in atomic nuclei Petr Veselý	69
Heavy flavor physics in heavy-ion collisions Jakub Česka	70
Nucleation and nanoparticle growth under the influence of ionizing radiation beta, gamma and UV-VIS photons of various wavelengths Karolína Šollová	73
Muons in cosmic ray showers Antonín Kravka	76
A study of radiation tolerance of the monolithic silicon detectors Václav Trličík	79

Collective effects in emission of a set of single-photon emitters Daniel Babjak	82
Coherent J/ψ photoproduction in ultra-peripheral Pb–Pb collisions with ALICE at the LHC Roman Lavicka	84
Nonlinear dynamics Tomáš Novák	87
Synthesis of elements Pavel Špíšek	91

Foreword

This year, for the 14th time, students, graduates, and teachers from the field of Experimental Nuclear and Particle Physics at FNSPE CTU met at the annual winter workshop. The meeting was held during the week of 12.–18. 01. 2020 at Penzion Krakonoš in the Jizera Mountains in the Czech Republic. The main goal of the workshop is to follow the progress of students, discuss problems and experiences and also to get to know each other better. Each participant gave a talk about their work or progress during the previous year. Extended abstracts of these talks are published in the proceedings you are holding now.

Editors

OBSERVATION AND MEASUREMENTS OF VECTOR-BOSON SCATTERING AT THE ATLAS DETECTOR

Ondřej Penc

1 Introduction

ATLAS, the state-of-the-art high energy physics detector threaded on the LHC ring at CERN, has been running for two data-taking periods and has collected enough data to probe very unique processes of the Standard Model (SM). This enables the ATLAS collaboration to measure high-profile final-states of a very specific set of processes as vector-boson scattering (VBS) is. The scattering consider interactions of the massive vector bosons in all possible Mandelstam channels including Higgs boson exchange. The scattered bosons posses of longitudinal polarization, which makes the process sensitive to high-energy asymptotic behavior. Imperfect cancellation of the divergent scattering realizations would violate tree unitarity as a necessary condition for perturbative renormalizability. Since the electro-weak bosons rise up in the SM by virtue of the embedded $SU(2)$ gauge symmetry group the VBS probes the non-abelian gauge structure of SM as well as the electro-weak symmetry breaking. The process encompasses all the mediators related to the mechanism as long as the Higgs boson plays a role in the scattering. The VBS is also sensitive to the physics beyond SM which would manifest itself in a form of increase in differential distributions of particular observables. This paper brings up an overview of the first measurements and observations towards the VBS. This can bring better understanding of the physics behind and future theoretical interpretations and limit settings for possible anomalous phenomena.

2 Summary

The searches for electroweak (EW) di-boson production represent the first step towards the VBS studies and accept great attention from the collaborations working in the EW sector of SM. All considered fully-leptonic final-states achieved to exclude the no-signal hypothesis with more than 5 standard deviations. All the channels observed the EW production and have opened the door for the further scrutiny of the VBS phenomena. The semi-leptonic final state channels are still waiting for the first evidence, but since only 35.5 fb^{-1} of Run 2 was processed with resulting 2.7σ , it is high likely to hold at least an evidence when exploiting the full dataset. Summary of signal strengths, significances, and cross sections of all channels are highlighted in table 1. The measurements are in a good agreement with the SM as the signal strengths (ratio of the data and MC modeled cross sections) are near to the value of one within the

Table 1: Electro-weak di-boson production summary table [2, 1, 4, 3, 5].

Process	Signal strength $\sigma_{\text{data}}/\sigma_{\text{MC}}$	Cross section $[\sigma_{EW}^{\text{fid.}}] = \text{fb}$	Significance observed/expected
$W^{\pm}W^{\pm}jj\text{--}EW(\ell^{\pm}\ell^{\pm})$	$1.44^{+0.26}_{-0.24}(\text{stat.})^{+0.28}_{-0.22}(\text{syst.})$	$2.89^{+0.51}_{-0.48}(\text{stat.})^{+0.29}_{-0.28}(\text{syst.})$	6.5/4.4
$WZjj\text{--}EW(\ell\ell\nu)$	$1.77^{+0.44}_{-0.40}(\text{stat.})^{+0.26}_{-0.21}(\text{syst.})$	$0.57^{+0.14}_{-0.13}(\text{stat.})^{+0.07}_{-0.06}(\text{syst.})$	5.3/3.2
$ZZjj\text{--}EW(\ell\ell\ell\ell)$	$1.54^{+0.37}_{-0.37}(\text{stat.})^{+0.05}_{-0.05}(\text{syst.})$	$1.27^{+0.12}_{-0.12}(\text{stat.})^{+0.08}_{-0.08}(\text{syst.})$	5.5/3.9
$ZZjj\text{--}EW(\nu\nu\ell\ell)$	$0.73^{+0.57}_{-0.57}(\text{stat.})^{+0.08}_{-0.08}(\text{syst.})$	$1.22^{+0.30}_{-0.30}(\text{stat.})^{+0.18}_{-0.18}(\text{syst.})$	1.2/1.8
$VVjj\text{--}EW(\text{semi lep.})$	$1.05^{+0.20}_{-0.20}(\text{stat.})^{+0.37}_{-0.34}(\text{syst.})$	$45.1^{+8.6}_{-8.6}(\text{stat.})^{+15.9}_{-14.6}(\text{syst.})$	2.7/2.5

uncertainty range. The presented channels provide very sensitive tests of SM and also possibility to discover new physics beyond the SM from differential cross-section distributions when extended dataset would be used.

3 Outlook

The fully-leptonic channels are all dominated by the statistical uncertainty. While the $WWjj$ and $WZjj$ channels can still exploit the second half of Run 2 the $ZZjj$ needs to wait for Run 3 to decrease the overall uncertainty. The semi-leptonic channel is dominated by experimental systematics because of higher dependency on the jet reconstruction. The problem of the semi-leptonic channel is, the Run 3 will provide even more busy environment for the measurement as a trade off for higher luminosity, so, the pileup contamination and jet reconstruction will be more demanding. The VBS physics program of Run 3 will advance forward to make the measurements more precise and differential and will enable polarisation studies employing the enlarged dataset.

References

- [1] <https://doi.org/10.1103/PhysRevLett.123.161801>
- [2] <https://doi.org/10.1016/j.physletb.2019.05.012>
- [3] <https://cds.cern.ch/record/2682845>
- [4] <https://doi.org/10.1103/PhysRevD.100.032007>
- [5] <https://cds.cern.ch/record/2655303>

PBSPRO BATCH SYSTEM

Zdenek Hubacek

1 Introduction

Today's huge datasets and advanced theoretical calculations are very CPU intensive and require large computing data centers in order to be processed. A small computing cluster `sunrise` [1] is available to students and employees of the Department of Physics at the Faculty of Nuclear Sciences and Physical Engineering of the Czech Technical University in Prague (FNSPE CTU). PBS Professional (PBSPRO) [2] batch system is the software responsible for scheduling the user jobs. Both the cluster and the software are going to be briefly described in this short note.

2 Computing Cluster sunrise

A small computing cluster `sunrise` (`sunrise.fjfi.cvut.cz` or IP address 147.32.5.210) is operated at the department. The cluster physically located in the Brehova 7 building basement consists at the time of writing (January 2020) of about 500 CPU cores split into two parts mainly by the age of the corresponding machines. The older part has about 256 cores on Intel Xeon architecture and currently runs on SLC6 operating system, the newer part also has around 256 cores (AMD EPYC) and the operating system is CentOS7. The plan is to migrate all nodes on CentOS7 in the near future and also to switch the old main sunrise login node to a new one with more CPUs and larger memory. A disk array with about 200TB of disk space is connected to the cluster. The resources are available to everyone at the department. Please contact the administrators for creating a computing account.

3 PBSPRO

In order to manage the resources, a batch system (job scheduler or distributed resource management system) is operated on the cluster. The system at the moment is PBS Professional 14.1.0 (PBSPRO). Users log into the main login node (either to old `sunrise.fjfi.cvut.cz` or to the newer `sunrise7.fjfi.cvut.cz` which will replace the old one in the future) and submit their jobs (tasks) from there to the batch system. The system manages all worker nodes (`sunset01` - `sunset28`) and the distribution of jobs to them automatically. Schematic diagram how the batch system works is shown in Fig. 1.

3.1 Basic PBSPRO Commands

The basic PBSPRO commands are listed below. The available space of this note is not sufficient to describe the details. Please refer to the documentation for more information.

- **qstat** is the main command to display status of PBS batch jobs, queues, or servers.
- **qsub** is the command to submit a job to the batch system. In the simplest case, the submission script is `qsub user_script.sh`.
- **qdel** deletes a job which a user deems is no longer required to run (or to finish).

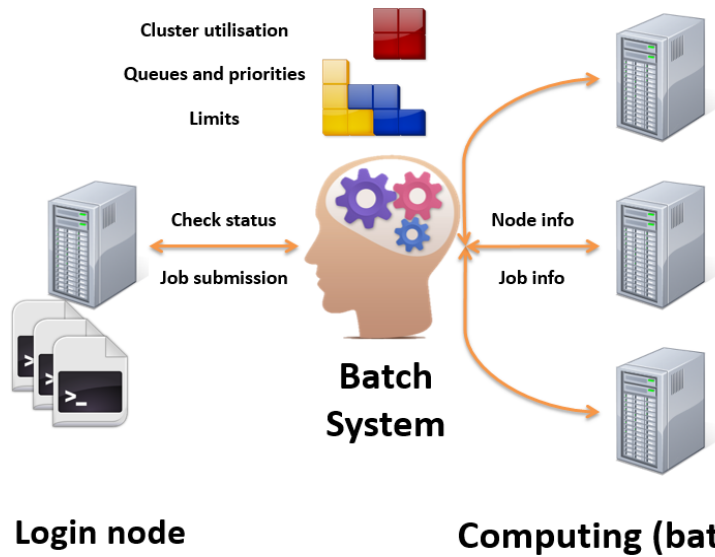


Figure 1: A schematic diagram of the computing batch system. Figure taken from [3].

A fairshare is a mechanism which allows information on historical resource utilization of individual users to be incorporated into job scheduling and to prioritize its decisions. Currently only a minimal fairshare system is used on the cluster.

The batch system could be monitored either using the *qstat* command or via a web page [4].

4 Summary

A small computing cluster is operated for the users at the Department of Physics of FNSPE CTU. A PBSPro batch system is used for managing the computing resources and for distributing user jobs among the worker nodes of the cluster. All users are encouraged to use the cluster following some simple rules and the common sense.

References

- [1] Computing cluster sunrise: <https://nms.fjfi.cvut.cz/wiki/Sunrise.fjfi.cvut.cz>
- [2] Altair Engineering, Inc., PBS Professional 14.2 User's Guide, 2017
- [3] Batch Systems, <https://confluence.ecmwf.int/display/UDOC/Batch+Systems>, accessed January 2020
- [4] Sunrise computing resources information: <http://http://sunrise.fjfi.cvut.cz/ganglia>, accessed January 2020

RDataFrame

Zdenek Hubacek

1 Introduction

The large event datasets available today require the use of a common and a simple framework in order to be analyzed efficiently. Several options exist in the ROOT scientific software toolkit [1]. Ignoring the frameworks unique to each high energy physics (HEP) experiment, several basic options available in ROOT are mentioned and a new option called `RDataFrame` [2] is briefly presented.

2 Event Loop

HEP events (either data collected by experiments or simulated Monte Carlo samples) are generally stored in the `TTree` columnar format [3]. A certain kind of loop over all events (rows in the record) is needed in order to process the whole dataset. Simple event loops include:

- **MakeClass**-type loop – the simplest loop generated automatically by the `TTree::MakeClass(...)` method.
- **MakeSelector**-type loop (legacy) – a more advanced loop generated with the `TTree::MakeSelector(...)` method. It also offers a method for parallelization of the loop for multiple processors.
- **TTreeReader**-type loop – a `TTreeReader` class which could be used in a loop either directly via `TTreeReader::Next()` method or inside a `TSelector` generated above.
- **RDataFrame** – a new type of event loop to be presented below.

3 RDataFrame

A new type of loop is available in the latest version of the ROOT toolkit (version 6.18.04 as of January 2020). The `RDataframe` class offers a high level interface for analyses of data stored in `TTree` data format. The user analysis is expressed as a chain of actions and transformations on the dataset (a graph) and `RDataFrame` deal with their execution. Data I/O and other details are generally hidden from the user who can concentrate on details of his/her analysis. In a simplified view, the `RDataFrame`'s way of event loop could be described as *declarative* programming while the original event loop types are *imperative* [4].

3.1 RDataFrame class

`RDataFrame` is the main class which allows to analyze and manipulate the data. It can be automatically constructed from a `TTree` in the user's dataset. Following the definition of the `RDataFrame`, either transformations or actions could be applied to it.

3.2 Transformations

Transformations are ways to manipulate the data. The transformations include `Define` to add a new variable in the dataset *on-the-fly* and `Filter` to filter (apply a cut) on the dataset. Other transformation types could be found in the

documentation. The result of each transformation is a new `RDataFrame`. Transformations are chained together to create the analysis workflow.

3.3 Actions

Actions are ways to produce a result out of the data. The simplest actions are `Count` to keep track of the number of events which passed the last transformation or `Histo1D` for plotting a 1-D histogram of a selected observable. Other types of actions are available as well. The result of each action is stored in a `RResultPtr` smart pointer which could be used in the program. There are two kinds of actions defined in the code - *instant* actions are executed when they are called, *lazy* actions, on the other hand, only trigger the event loop when one of the results is accessed for the first time.

3.4 RVec

`ROOT::RVec` is a special container or a `std::vector`-like collection of values which implements a handy operation to analyse them. This operation enables e.g. a simple collection filtering without coding the explicit loop over items in the collections. This class is extensively used in the `RDataFrame` code to analyze and filter the collections effectively. See Ref. [5] for details and examples.

3.5 Analysis

The user analysis is finally a list of transformations and actions chained together. The framework offers a simple option to create a graph of the user analysis so it could be checked for mistakes in the analysis flow. An example of a simple analysis graph is shown in Fig. 2. A cutflow of processed filters is easily available as well. The framework implementation automatically puts in place several optimisations such as a multi-thread parallelization which could be turned on with a simple `ROOT::EnableImplicitMT()` command. The user merely needs to guarantee the thread safety of his/her own code.

4 Summary

A new type of event loop available in the latest version of the ROOT toolkit is shortly presented. It offers an interesting option to perform an analysis which can be easily adapted to run on multiple CPU cores.

References

- [1] R. Brun and F. Rademakers, ROOT - An Object Oriented Data Analysis Framework, Proceedings AIHENP'96 Workshop, Lausanne, Sep. 1996, Nucl. Inst. & Meth. in Phys. Res. A 389 (1997) 81-86. See also <http://root.cern.ch/>
- [2] `RDataFrame` class description, https://root.cern/doc/master/classROOT_1_1RDataFrame.html, accessed January 2020
- [3] `TTree` class description, <https://root.cern.ch/doc/master/classTTree.html>, accessed January 2020
- [4] For some basic examples and discussions, see: https://en.wikipedia.org/wiki/Declarative_programming and https://en.wikipedia.org/wiki/Imperative_programming, accessed January 2020
- [5] `RVec` class description, https://root.cern/doc/master/classROOT_1_1VecOps_1_1RVec.html, accessed January 2020

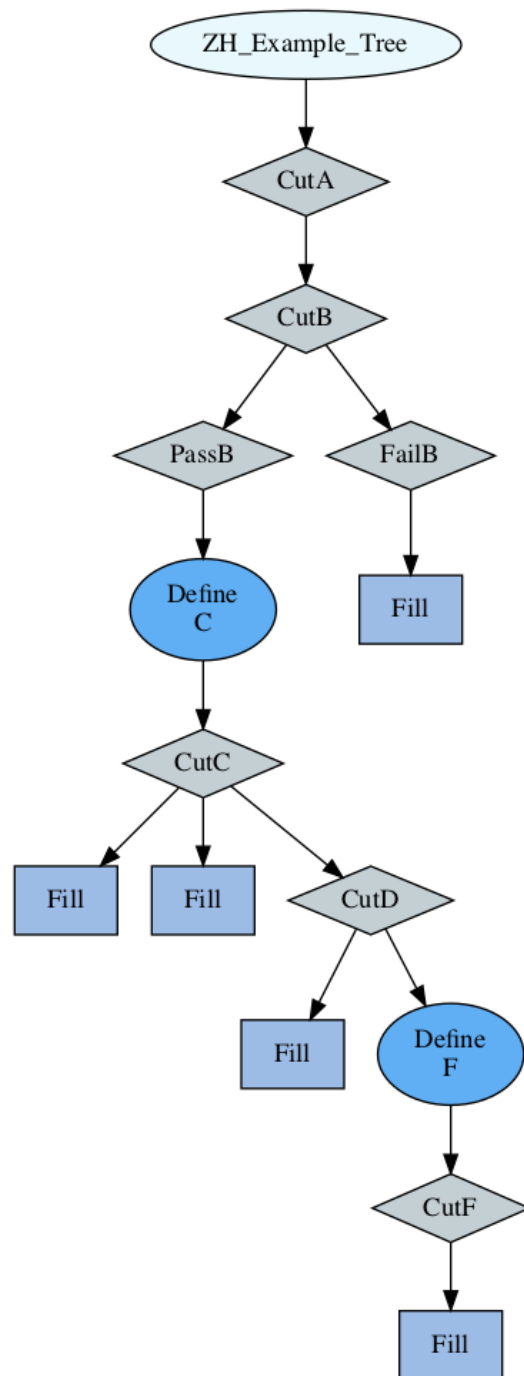


Figure 2: A graph representing a simple analysis.

THE FORWARD DIFFRACTIVE DETECTOR

Solangel ROJAS TORRES

1 Introduction

The ALICE Collaboration has built a dedicated heavy-ion detector to exploit the unique physics potential of nucleus-nucleus interactions at LHC energies [1]. The aim is to study the physics of strongly interacting matter at extreme energy densities, where the formation of a new phase of matter, the Quark-Gluon Plasma (QGP), is expected. ALICE have 19 detectors and systems, that allow the experiment have an excellent particle identification capabilities.

During Run-2 of the LHC the ALICE Diffractive (AD) detector was installed to extend the pseudorapidity coverage of ALICE, increasing its capacities to trigger diffractive and ultra-peripheral events [2]. The Forward Diffractive Detector (FDD) is the upgrade of AD to fulfill the new requirements of the LHC conditions and will be integrated in the new ALICE environment. FDD keep the same geometry and placement of its predecessor but with improvements in materials used for its construction and will be part of Fast Interaction Trigger system.

2 ALICE upgrade

The ALICE Collaboration has built a dedicated heavy-ion detector to exploit the unique physics potential of nucleus-nucleus interactions at LHC energies, to study mainly the QGP properties using its excellent particle identification allowed by using 19 different detectors and systems, as the Inner Tracking System (ITS), Time Projection Chamber (TPC), scintillator and Cherenkov detectors in the forward regions, among others.

After the ongoing second Long Shutdown (LS2), the LHC will progressively increase its luminosity and collision rate: $\mathcal{L} = 6 \times 10^{-27} \text{cm}^{-2} \text{s}^{-1}$ and 50 kHz for Pb-Pb collisions; and $\mathcal{L} = 10^{-34} \text{cm}^{-2} \text{s}^{-1}$ and 1 MHz for protons beams. The new proposed scenario represent a challenge for ALICE. In order to face the conditions expected for the Run-3 and Run-4, a significant upgrade of the system and detector is undergoing, such as a new TPC, ITS, and the Fast Interaction Trigger (FIT). The Central Trigger Processor will implement an important change, including a continuous readout mode in addition to running in the trigger mode.

2.1 Fast Interaction Trigger

The FIT detector is formed by three subdetectors: V0+, T0+ and FDD, which are the upgrades of V0, T0 and ALICE Diffractive (AD) respectively [3]. T0+ is a Cherenkov quartz radiators array using MCP-PMTs, while V0+ and FDD are made of plastic scintillator, using optical fibers to transport the light signals to a fine mesh PMT [6]. The three subdetectors will be placed in the forward regions respect to the interaction point and integrated in a common readout and Detector Control System.

The subdetectors of FIT system will deliver the lowest trigger level and different trigger classes:

- Multiplicity: V0+ (LM)
- Luminosity: T0+, V0+ and FDD (L0)
- Collision time and vertex: T0+ (LM)
- LHC background (BG): V0+ and FDD (L0)
- VETO (UPC, electromagnetic and diffractive interactions): T0+, V0+ and FDD (L0)

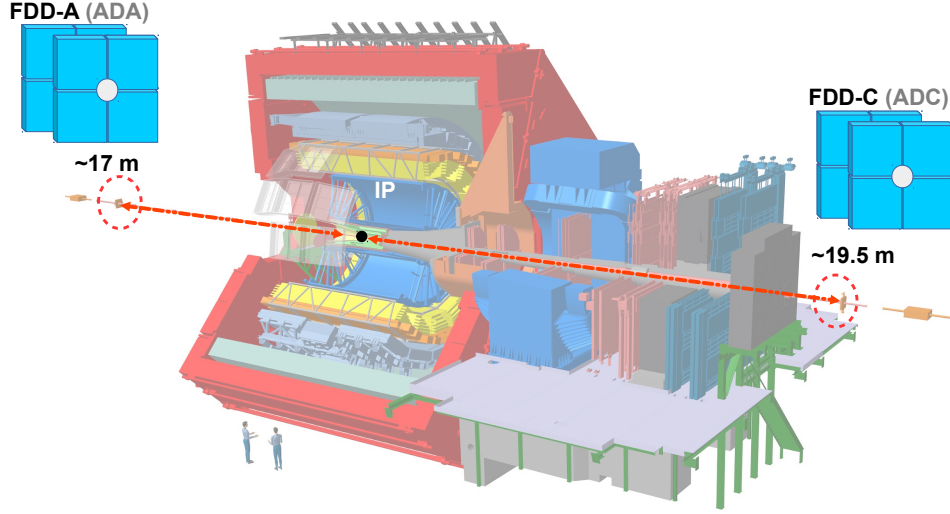


Figure 3: Segmentation and placement of the FDD (former AD) respect to the interaction point.

3 Diffraction in ALICE

There is a rich physics which take place close to the forward directions, where elastic processes can be detected and have an important contribution to the p-p cross section. The inelastic processes are usually further categorized into diffractive and non-diffractive contribution [4]. Where in diffractive events one or both incoming particles either remain intact or dissociate into products emitted at very small angle when exchange a virtual particle (the Pomeron) that carries no color. The experimental signature of diffractive processes are regions in rapidity devoid of particle production called rapidity gaps. Around of 30% of p-p interactions are diffractive processes.

3.1 Run 1

During Run-1 of the LHC, measurements of cross sections of inelastic, single- and double-diffractive cross section of p-p where made in ALICE, at three centre-of-mass energies: 0.9, 2.76 and 7 TeV. For those measurements V0, SPD and FMD detectors where used as trigger for the selection of minimum-bias events [5], covering a continuous acceptance over a pseudorapidity interval of 8.8 units. The TPC and the whole ITS were used in this study only to provide the interaction vertex position, from reconstructed tracks. A study of gaps in the pseudorapidity distributions of particles produced in pp collisions at the LHC was used to measure the fraction of diffractive events in inelastic pp collisions at $\sqrt{s} = 0.9, 2.76$ and 7 TeV. The ALICE result on diffractive fractions with a center-of-mass energies are consistent with the UA5 at 0.9 TeV and with those from ATLAS [7], CMS and TOTEM [8] at 7 TeV .

3.2 ALICE Diffractive detector

During the long shutdown 1 (LS1) the AD detector was successfully constructed, installed in 2014, to enlarge the pseudorapidity coverage ($4.7 < \eta < 6.3$ and $-6.9 < \eta < -4.9$) and to improve the sensitivity to lower diffractive masses in ALICE experiment [2]. AD detector consist of two sub-detectors, placed in A- and C-side of the ALICE cavern along the beam-pipe at 17 and 19.5 meters respectively, each sub-detector or station is an assembly of two layers segmented in four pads, as can be seen in fig. 3. The pads were made of plastic scintillator, two Wavelength Shifting bars (WLS bars) are coupled in two sides of the pads; they are separated by 0.4 millimeters of air to maximize the light transmission to the Wavelength Shifting bars and collect the light produced inside scintillators. To transport the light of each pad, a bundle of 192 fibres (96 for each WLS bar) are coupled to one Photomultiplier Tube (PMT), converting the light into an electronic signal.

AD has provided the measurements of centrality in the most forward regions, worked as beam quality monitoring (distinguishing clearly beam-beam and beam-gas interaction) and also as been used as veto detector for an ultra-peripheral studies [9] with ALICE.

4 Forward Diffractive Detector

The FDD is an instrument that currently is under the research and development process, with the goal to be ready for installation and commissioning at the end of the year (2020). FDD will keep the same geometry and the placement position as AD [2]. Nevertheless, the main improvements made for FDD respect to AD, are faster plastic scintillators and WLS bars used for the construction.

A key point for the performance of the detector is the new WLS bar: the NOL-38 wavelength shifter bar have a decay time of about 1 ns, which will allow us to have a narrower signal pulse in comparison with the 8.5 ns decay time of the AD WLS bar (EJ-280). The plastic scintillator will be changed to the BC-420, in order to match the absorption wavelength of the WLS bar. The optical fibers will be the same as AD (Kuraray PSM-Clear) and the PMT will be changed to a fine mesh 19 dynodes of produced for hamamatsu (H8409-70).

The integration of the detector to the ALICE Data Acquisition and Central Trigger will be made through the Front-End Electronics designed for FIT, to operate FDD together with V0+ and T0+. This FIT electronics will allow to configure, control and readout the detector, as well as operate in the new continuous readout and trigger mode.

5 Final comments

Since the AD detector worked successfully during Run 2 and with the experience obtained, we expect that with the upgrade, we can achieve the characteristics required for the new LHC conditions. The full characterization and construction is ongoing, as well as the studies to tune the electronic boards. The detector will be installed and commissioned along the last semester of 2020 in order to be ready for the ALICE global commissioning and integration.

References

- [1] Abelev, B and others. Upgrade of the ALICE Experiment: Letter Of Intent. J. Phys. G41, pages 087001, 2014. [10.1088/0954-3899/41/8/087001](https://doi.org/10.1088/0954-3899/41/8/087001).
- [2] Akiba, K and others. LHC forward physics. Journal of Physics G: Nuclear and Particle Physics, pages 110201, 2016. [10.1088/0954-3899/43/11/110201](https://doi.org/10.1088/0954-3899/43/11/110201).
- [3] Antonioli, P and Kluge, A and Riegler, W and others. Upgrade of the ALICE Readout and Trigger System. *CERN-LHCC-2013-019. ALICE-TDR-015*, 2013.
- [4] yskin, M.G., Martin, A.D. and Khoze. High-energy strong interactions: from ‘hard’ to ‘soft’. Eur. Phys. J. C, vol. 71, 2011. doi.org/10.1140/epjc/s10052-011-1617-2.
- [5] Abelev, Betty and others. Measurement of inelastic, single- and double-diffraction cross sections in proton–proton collisions at the LHC with ALICE. Eur. Phys. J., vol. 73, 2013. *ARXIV:1208.4968*.
- [6] Wladyslaw Henryk Trzaska. New Fast Interaction Trigger for ALICE Nuclear Instruments and Methods in Physics Research Section A, vol. 845, 2017. doi.org/10.1016/j.nima.2016.06.029.
- [7] Aad, Georges and others. Measurement of the Inelastic Proton-Proton Cross-Section at $\sqrt{s} = 7$ TeV with the ATLAS Detector Nature Commun., vol. 2, 2011. *ARXIV:1104.0326*.
- [8] G. Antchev and others. First measurement of the total proton-proton cross-section at the LHC energy of $\sqrt{s} = 7$ TeV. Europhysics Letters, vol. 96, 2011. [10.1209/0295-5075/96/21002](https://doi.org/10.1209/0295-5075/96/21002).
- [9] S. Acharya and others. Coherent J/Ψ photoproduction at forward rapidity in ultra-peripheral Pb–Pb collisions at $\sqrt{s_{NN}}=5.02$ TeV. Physics Letters B, vol. 798, 2019. doi.org/10.1016/j.physletb.2019.134926.

B-DEPENDENT BK IN ALL ITS BEAUTY

Marek Matas

Abstract

This is a complementary material for a talk I gave at Workshop of the EJCF group at Bily Potok. I have focused on a thorough review of the BK formalism starting with a simplified derivation of the equation, then going over some of its features including how it relates to the observables and ending with its application to the b-dependent processes and cases of heavy nuclei. This work expands on the talk and adds a few details, that were not covered in the slides for the sake of simplicity and pace of the lecture.

1 Introduction

In my talk, I have focused on evolution equations in high-energy QCD, explaining the differences between Balitsky-Kuraev-Fadin-Lipaton (BFKL) equation [1, 2] that incorporates gluon branching processes and Balitsky-Kovchegov (BK) evolution equation [3, 4, 5] that includes non-linear terms incorporating saturation effects. I have described how this equation can be utilized for obtaining impact-parameter dependent solutions in the collinearly improved framework [6]. This talk is based on the work covered in [7, 8].

2 The Balitsky-Kovchegov equation

The BK equation with impact parameter dependence reads

$$\begin{aligned} \frac{\partial N(r, b; Y)}{\partial Y} = & \int d\vec{r}_1 K(r, r_1, r_2) \left(N(r_1, b_1; Y) \right. \\ & \left. + N(r_2, b_2; Y) - N(r, b; Y) - N(r_1, b_1, Y)N(r_2, b_2; Y) \right), \end{aligned} \quad (1)$$

where $\vec{r}_2 = \vec{r} - \vec{r}_1$ and $|\vec{r}_i| \equiv r_i$. The variables b_1 and b_2 denote the magnitudes of the impact parameters of the daughter dipoles.

The collinearly improved kernel that suppresses large daughter dipole contribution [6] is

$$K(r, r_1, r_2) = \frac{\bar{\alpha}_s}{2\pi} \frac{r^2}{r_1^2 r_2^2} \left[\frac{r^2}{\min(r_1^2, r_2^2)} \right]^{\pm \bar{\alpha}_s A_1} \frac{J_1(2\sqrt{\bar{\alpha}_s \rho^2})}{\sqrt{\bar{\alpha}_s \rho}}. \quad (2)$$

The value of A_1 is 11/12 and the sign in the third factor is chosen positive when $r^2 < \min(r_1^2, r_2^2)$ and negative otherwise. $\rho \equiv \sqrt{L_{r_1 r} L_{r_2 r}}$, J_1 is the Bessel function and $L_{r_i r} \equiv \ln(r_i^2/r^2)$. The smallest dipole prescription was chosen for the running coupling: $\alpha_s = \alpha_s(r_{\min})$, where $r_{\min} = \min(r_1, r_2, r)$ as in [9].

The initial condition for the evolution described in my talk was

$$N(r, b, Y = 0) = 1 - \exp \left(-\frac{1}{2} \frac{Q_s^2}{4} r^2 T(b_{q_1}, b_{q_2}) \right), \quad (3)$$

where b_{q_i} are the impact parameters of the individual quark and antiquark of the initial bare dipole and

$$T(b_{q_1}, b_{q_2}) = \left[\exp\left(-\frac{b_{q_1}^2}{2B}\right) + \exp\left(-\frac{b_{q_2}^2}{2B}\right) \right]. \quad (4)$$

It combines the approach of the GBW model [10] and exponential fall-off for the proton [11]. More thorough details about the initial condition, evolution and parameters can be found in [7].

3 Results

Fig. 4 shows the computed scattering amplitude as a function of rapidity, impact parameter and transverse dipole size. Coulomb tails in the large- b regions are strongly suppressed [7] in this framework. Computed structure function compared with data is shown in fig 5.

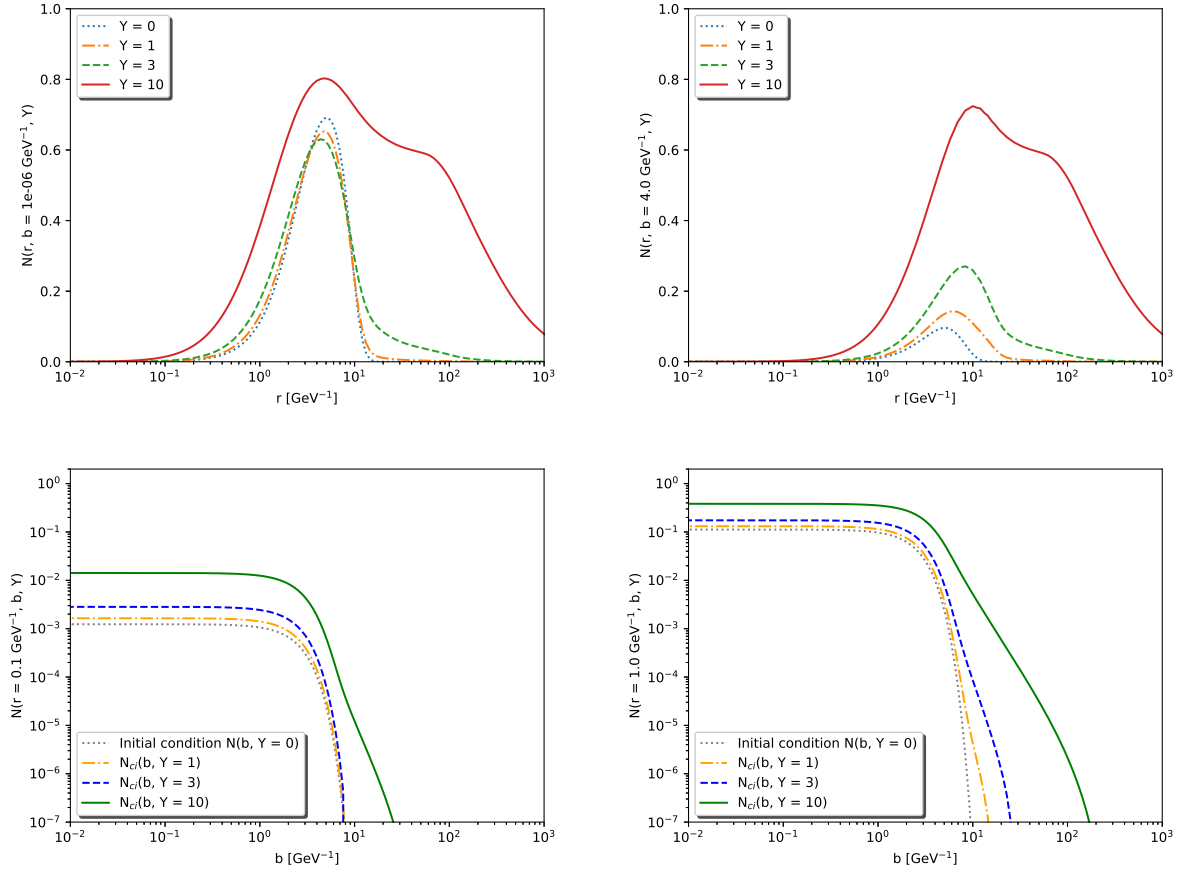


Figure 4: The scattering amplitude as a solution to the BK equation with the collinearly improved kernel as a function of r for $b = 10^{-6} \text{ GeV}^{-1}$ (upper left) and $b = 4 \text{ GeV}^{-1}$ (upper right), and as a function of b at $r = 0.1 \text{ GeV}^{-1}$ (lower left) and at $r = 1 \text{ GeV}^{-1}$ (lower right). Figure taken from [7].

4 Summary

The collinearly improved kernel along with the impact-parameter-dependent BK equation suppresses large daughter dipole contribution to the evolution and this in turn enables us to use the scattering amplitude for further phenomenological applications [7].

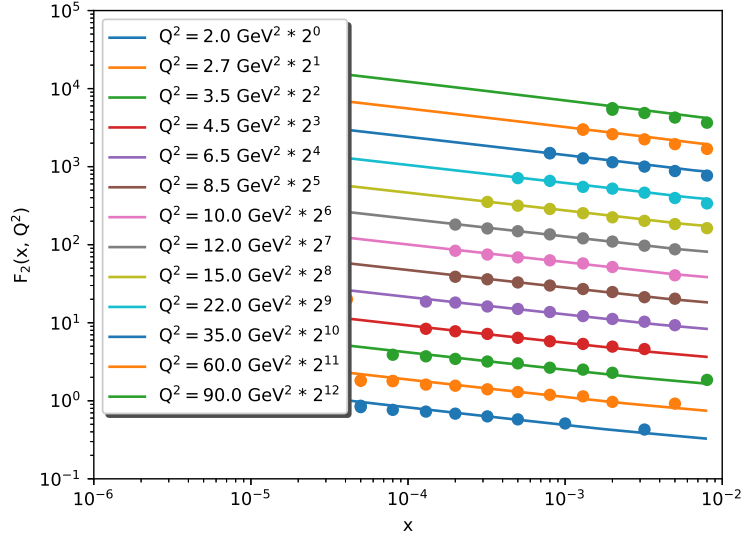


Figure 5: Comparison of the structure function data from HERA [12] (solid circles) to the prediction of the impact-parameter dependent BK equation with the collinearly improved kernel (lines). Figure taken from [7].

References

- [1] E. A. Kuraev, L. N. Lipatov, and Victor S. Fadin. The Pomeranchuk Singularity in Nonabelian Gauge Theories. *Sov. Phys. JETP*, 45:199–204, 1977. [*Zh. Eksp. Teor. Fiz.*72,377(1977)].
- [2] I. I. Balitsky and L. N. Lipatov. The Pomeranchuk Singularity in Quantum Chromodynamics. *Sov. J. Nucl. Phys.*, 28:822–829, 1978. [*Yad. Fiz.*28,1597(1978)].
- [3] I. Balitsky. Operator expansion for high-energy scattering. *Nucl. Phys.*, B463:99–160, 1996.
- [4] Yuri V. Kovchegov. Small x $F(2)$ structure function of a nucleus including multiple pomeron exchanges. *Phys. Rev.*, D60:034008, 1999.
- [5] Yuri V. Kovchegov. Unitarization of the BFKL pomeron on a nucleus. *Phys. Rev.*, D61:074018, 2000.
- [6] E. Iancu, J. D. Madrigal, A. H. Mueller, G. Soyez, and D. N. Triantafyllopoulos. Resumming double logarithms in the QCD evolution of color dipoles. *Phys. Lett.*, B744:293–302, 2015.
- [7] D. Bendova, J. Cepila, J. G. Contreras, and M. Matas. Solution to the Balitsky-Kovchegov equation with the collinearly improved kernel including impact-parameter dependence. *Phys. Rev.*, D100(5):054015, 2019.
- [8] J. Cepila, J. G. Contreras, and M. Matas. Collinearly improved kernel suppresses Coulomb tails in the impact-parameter dependent Balitsky-Kovchegov evolution. *Phys. Rev.*, D99(5):051502, 2019.
- [9] E. Iancu, J. D. Madrigal, A. H. Mueller, G. Soyez, and D. N. Triantafyllopoulos. Collinearly-improved BK evolution meets the HERA data. *Phys. Lett.*, B750:643–652, 2015.
- [10] Krzysztof J. Golec-Biernat and M. Wusthoff. Saturation effects in deep inelastic scattering at low Q^2 and its implications on diffraction. *Phys. Rev.*, D59:014017, 1998.
- [11] Henri Kowalski and Derek Teaney. An Impact parameter dipole saturation model. *Phys. Rev.*, D68:114005, 2003.
- [12] F. D. Aaron et al. Combined Measurement and QCD Analysis of the Inclusive e^+p Scattering Cross Sections at HERA. *JHEP*, 01:109, 2010.

ASSESSMENT OF VARIOUS STANDARD-MODEL PHENOMENA AWARENESS AT $t \sim 13.8$ GA AND NON-VANISHING NET-BARYON DENSITY AT THE WEJCF EXPERIMENT - 4TH EDITION

Robert Licenik

1 Introduction

In continuation of the previous editions of this assessment [1, 2, 3], the 4th edition was conducted on January 13 2020 at the 15th *Workshop EJČF* conference, with the main aims to entertain the attendants, to bring the 3rd-year students closer to the EJČF group and also to assess the general knowledge of the participants. The assessment was carried out by the form of a pub-style quiz (see [4] for example), containing 56 questions from various semi-randomly chosen topics, presented by the Moderator to 6 teams of 6 or 7 members (see Tab. 3). A point was awarded to each team for each correct answer (in some cases, half-points for an incomplete answer are awarded). The questions were divided into 10 topics, two topics per round, with each round containing one additional guessing question to award a point to the team whose guess was the closest to the correct answer. To ensure smooth flow of the quiz, the following rules were established: *Answers are turned in at the end of each round and are final, Only acceptable devices are pen and paper, Write short, clear and easy-to-read answers, By default, last name/genus is sufficient, when applicable, The Moderator is the ultimate authority, All teams must include at least one 3rd year student* and last - informal - rule *Each team must share a drink with the Moderator*. This last rule was ignored by some of the teams (shame on them). The final ranking was determined based on the following criteria:

Table 2: Ranking criteria (higher number is better, unless specified otherwise).

Priority	Criterion
1	Total points
2	Total points without guessing questions
3	Number of team members (lower)
4	Number of 3rd year students in a team
5	56th answer (more accurate)
6	Brawl between teams in front of the guest house

The winner of the quiz was given a prize consisting of a bottle of rum and never-ending fame among the participants. The 56th question was asked after the determination of the winner and, in addition to serving as a potential tie-breaker, served as an opportunity for a consolation prize for all non-winning teams. Whichever team was the closest to the correct answer to the 56th question received a round of beers for their table. If this team were the same that won the quiz, this prize would be awarded to the team with the second-closest answer.

2 Questions

For each of the 5 rounds, two topics that link the 5 questions together in a obvious or less-obvious ways were semi-randomly selected. The quiz traditionally opened with a current-event themed topic, containing questions such as

Druhého ledna 2020 oslavil své 55. narozeniny pořad vysílaný na České televizi, jehož znělka je nejstarší stále používanou znělkou v Česku. Jak se pořad jmenuje? - with the correct answer being *Večerníček*, followed by a topic dedicated to World's wonders, where the contestants had to answer for example this question: *Jak se jmenoval řecký bůh, kterého znázorňovala socha Rhodský kolos? Náповědou vám může být, že byl později sjednocován s Apollónem.*, with the correct answer being *Hélios*. The questions were shown on a screen and read aloud by the Moderator, who waited around one minute before moving forward with the next question. After collecting and evaluating the answer sheets, the correct answers were presented to the participants and the ranking was revealed. In order to make the quiz less repetitive, several formats of questions were used. While the majority of the questions were open-answer, some were multiple-choice questions, simple yes-no questions, cross-matching questions and ordering questions. Some questions featured a hint to adjust the difficulty of that question, while sometimes a supporting image was shown.

The second round featured a *Could they meet?* topic regarding pairs of famous historical figures including queens *Cleopatra* and *Boudicca (Ne)* or activists *Yasser Arafat* and *Greta Thunberg (Ano)*, where the only criterion was whether they lived at the same time (even one day). The other topic featured in this round was *Lord of the Rings*, which was a special topic selected in an online poll by the would-be participants about a month before the quiz. A question example is *Jak je trpaslíky nazýván balrog, kterého potká Společenstvo prstenu v Morii a se kterým svede souboj Gandalf?* - *Durnova zhouba*.

The third round opened with a topic called *Heights*, which featured questions such as *Která z těchto staveb je nejvyšší stavbou v ČR?* A) Vysílač Liblice B) AZ Tower v Brně C) Komín elektrárny Pruněřov II D) Žižkovská televizní věž, where the correct answer is A. The second part of the third round - this year called *It's not in the name* - is usually devoted to music, where the Moderator plays a song snippet and the questions usually ask for the author and/or song name. Songs played this year were *Eagles - Hotel California*, *Don McLean - American Pie*, *System of a Down - Chop Suey!*, *Jaromír Nohavica - Malé české blues* and *R.E.M. - Losing My Religion*.

In the fourth round, the first topic was centered around *Races* with questions such as *Kvízový závod je v plném proudu, tak pojďme na další téma! Nejslavnější motoristický závod v Česku (Grand Prix ČR) se jezdí na brněnském závodním okruhu. Jak se okruh jmenuje?*, where the correct answer is *Masarykův okruh*, while the latter part of this round featured questions about *Extinct animals*, for example *Lidská činnost měla v průběhu let za následek vyhynutí velkého množství živočišných druhů. Typickým příkladem vyhubeného tvora je nelétavý pták Dronte mauricijský, známý také jako dodo, případně pod jménem s iniciálami BN. Napište jej a máte bod.*, with *Blboun Nejapný* being the correct answer.

The final round of this year's quiz opened with questions about *Presidents of the USA*, for example: *Zatím posledním zesnulým bývalým prezidentem USA je George H. W. Bush, který zemřel 30. listopadu 2018 ve věku 94 let. Nepočítaje současného prezidenta Donalda Trumpa, kolik bývalých prezidentů USA je stále naživu?* - 4. The last topic of the quiz is usually reserved for image-recognition. This year, five snippets from either the first or last chapter of famous books were presented and the task was to identify the author and the name of the book. An example can be seen in Fig. 6. The answer to this question is intentionally not revealed, so the reader can test his/her knowledge.

The guessing questions in general (and especially the 56th) were selected so that multiple closest answers were unlikely, such as *Kolik liber si vydělal vítěz nejslavnějšího dostihového závodu v Evropě, The Grand National (známý v Česku také jako Velká Liverpoolská), v roce 2019?* If multiple teams came the closest to the correct answer (£ 561 300 in the previous case), a point was awarded to all of them.

3 Results and Conclusions

The results of the quiz are summarized in Tab. 3, including the team names, points gained in each round, total points, number of guessing points gained and number of team members. The table is in a descending order by the final rank.

One can conclude the following: *Poslední cukřenka*, which placed 6th was trailing since the first round, totaling 25 points (5 points/round average) with 0 correct guesses. *Federace fyzikálních anarchistů* started slowly and even a devastating finish (10 points in the last round) and one correct guess did not help them move past the 5th place. The

Okraje knih

Ukázka číslo 2:

1. kapitola

V RODNÉM DOMĚ

To, že mi osud určil jako rodiště Braunau an Inn, považuji dnes za předurčení šťastné. Toto městečko leží přece na hranici oněch dvou německých států, jejichž opětné spojení se alespoň nám mladým jeví jako životní úkol, který musíme uskutečňovat všemi prostředky!

Figure 6: An example question from the last topic, also showing the design of the slides.

Table 3: Results of the assessment, including team name, points gained in each round and total points, number of guessing questions won and number of team members.

Tým	1. kolo	2. kolo	3. kolo	4. kolo	5. kolo	bodů celkem	tipovačky	počet členů
Poslední cukřenka	4.5	6	4.5	4.5	5.5	25	0	6
Federace fyzikálních anarchistů	6	4.5	5	7	10	32.5	1	7
Chinese dragons of QCD	7.5	6	7.5	7	5	33	2	7
Nic německého	6	7	8.5	6.5	6.5	34.5	1	7
Nevím, já jsem přinesla propisku	7	5.5	7	8.5	7	35	1	6
Společenstvo prstenu	9	10	5	7.5	6.5	38	1	7

fight for the top 3 was very close throughout the quiz, with contenders *Chinese dragons of QCD (CD)* (a partially international team, which might have had a disadvantage in a Czech-language quiz), *Nic německého (NN)* and *Nevím, já jsem přinesla propisku (NJJPP)* teams being all tied for the 2nd place before the last round with 28 points. In the end *NJJPP* had the strongest finish to place 2nd with 35 points, while *NN* displayed a consistent performance to claim the 3rd place. *CD* were awarded the 4th place after a slower finish, while getting 2 guess points. The race for the first place was essentially over after the first two rounds, where *Společenstvo prstenu* managed to gain 19 points and, even after a small scare in the third (only 5 points), comfortably won the quiz with a 38 points total (7.6 points/round average). The 56th question asked *Kolik stran celkem mají originální knihy trilogie Lord of the Rings: The Fellowship of the Ring, The Two Towers a The Return of the King ve své první edici?*, and the team closest to the correct answer 1192 were *CD*, continuing their tradition of great educated-guessing to enjoy the free beers. Overall, the quiz has been generally described as "hard but good". No strong correlation between the final results and team composition age-, gender-, nationality-, education-, and alcohol-consumption-wise can be observed from the measured data, which means that a similar assessment must be carried-out at the next suitable occasion.

References

- [1] Robert Licenik, Jan Pokorný, Josef Uchytíl. Kvíz na Workshopu EJČF 2017. In 11th Workshop EJČF 2017, Bily Potok, 1/19/2017.
- [2] Robert Licenik. Kvíz na Workshopu EJČF 2018. In 12th Workshop EJČF 2018, Bily Potok, 1/18/2018.
- [3] Robert Licenik. Kvíz na Workshopu EJČF 2019. In 13th Workshop EJČF 2019, Bily Potok, 1/14/2019.
- [4] Hospodský kvíz [online, cit. 1/30/2020], <https://hospodskykviz.cz/>.

PROTON STRUCTURE - A SHORT INTRODUCTION TO PARTON DISTRIBUTIONS

Dagmar Bendová

1 Introduction

This text is a summary of the talk given at Workshop of Experimental Nuclear and Particle Physics 2020 of FNSPE CTU at 17th January in Bílý Potok.

Understanding hadron structure in terms of its constituent quarks and gluons is one of the most challenging problems of Quantum Chromodynamics. An experimental endeavour in this fields dates to early 70's to experiments trying to uncover the inner structure of nucleons in their interaction with electrons. This process is called Deep inelastic scattering and proceeds as follows. The incoming electron emits a virtual photon γ^* which interacts with the nucleon, usually taken to be a proton. As a result of the interaction, the proton is broken and a final state hadronic system is observed. The cross section for such a process depends on the so-called structure functions – denoted as F_1 and F_2 – which include the information about the photon-proton interaction and parametrize the inner structure of the proton, similarly as form factors parametrize the finite size of nuclear targets in low-energy scattering experiments of electrons on nuclei. In the following text, the relation of these structure functions to the distributions of proton's constituents will be briefly introduced. Also, the extension to the case with polarization degrees of freedom, the 3D description of the proton structure in terms of parton's momenta and positions, and the unifying concept to the previous cases will be introduced.

2 Distributions of partons in the proton

2.1 The parton model and collinear parton distribution functions

The DIS cross section can be written as

$$\frac{d\sigma}{dx dQ^2} = \frac{4\pi\alpha^2}{Q^4} \left[(1-y) \frac{F_2(x, Q^2)}{x} + y^2 F_1(x, Q^2) \right], \quad (5)$$

where α is the fine-structure constant, Q^2 is the virtuality of the exchanged photon, and y gives the measure of the inelasticity of the process. In the parton model, this process can be viewed as an interaction of the virtual photon with one of the point-like constituents of the proton, called partons, which we associate with quarks and gluons nowadays. In this approach, we consider partons to be fermions and neglect their transverse motion. Therefore they carry a momentum fraction x of the proton's longitudinal momentum P . Structure functions F_1 and F_2 can be related to the probability of finding parton of type i with the momentum fraction x , called parton distribution function (PDF) in the proton

$$F_2(x) = x \sum_i e_i^2 \cdot f_i(x); \quad F_1(x) = \frac{1}{2} \sum_i e_i^2 \cdot f_i(x), \quad (6)$$

where e_i^2 is the charge of quark. As one can noticed, in the previous relation, the dependence on Q^2 has been omitted. This is a consequence of so called Bjorken scaling, which assumes that the proton structure does not depend on Q^2 which represents a resolution of our probe, i.e. virtual photon. This assumptions is indeed valid at high values of x , however for $x \sim 10^{-2}$ and lower, the Bjorken scaling is broken and a dependence of structure functions on Q^2 is

observed. This is due to the parton branching process described by DGLAP evolution equations. Also when summing over the all quark's momenta, one misses a part of the momentum fraction which tells us that there have to be some other, electrically neutral component which dominates at low values of x . Therefore there are following contributions to the hadron structure – valence quarks which dominate at low x , sea quarks which emerge as $q\bar{q}$ pairs from available vacuum energy and have large contribution in low x region, and gluons, which dominate the low x region.

This traditional descriptions of the parton distributions can be extended when using polarized particles. Traditionally, PDFs are measured considering unpolarized proton and constituent quarks and therefore, they give a measure of number density of partons. However one can also considered either a longitudinally or a transversally polarized proton and a quarks having its spin (anti)aligned with the proton polarization. As a result one obtains two additional PDFs called helicity $g_1 \equiv \Delta q_i(x)$, resp. transversity h_1 . The helicity gives a difference in probabilities to find quarks with their spin aligned or anti-aligned to the spin of the longitudinally polarized nucleon. The transversity then measures the correlation between the transversally aligned spins of the quark and the nucleon. The polarized PDFs give a complete description of the nucleon structure in terms of x and spins and they can be measured in DIS with polarized leptons or nucleons.

2.2 Transverse momentum distributions

In addition to the longitudinal momenta of the partons, we can also consider that they carry their intrinsic transverse momenta, denoted as k_x and k_y . The simplest transverse momentum \vec{k}_T distribution (TMD) is an unpolarized quark PDF with a \vec{k}_T -dependence, denoted as $f_1^q(x, \vec{k}_T)$. The collinear PDF can be then obtained from f_1 by integrating over \vec{k}_T .

For a fast moving parton, the value of its transverse momentum is much smaller compared to its longitudinal momentum, i.e. $k_T \ll xP$, therefore it is experimentally challenging to measure TMDs. However, a transverse spin, which can correlate with parton's \vec{k}_T , can be used as a probe of TMD effects. One of the clear experimental proofs of the existence of transverse motion of partons is the effect called *single spin asymmetry*. It is a "left-right" asymmetry of produced particles from the hadronic scattering of transversally polarized protons by an unpolarized proton. If partons carry only longitudinal momentum component, this effect should vanish. There are also other available processes which allow for measurement of TMDs, e.g. semi-inclusive deep inelastic scattering, Drell-Yan process, diffractive dijet production, etc. In overall, there are eight TMDs at leading order which give a distribution of (un)polarized quarks in an (un)polarized nucleon. Only three of these distributions survive integration over \vec{k}_T – these are the above introduced polarized PDFs. The remaining 5 TMDs, called off-diagonal, vanish when integrating over \vec{k}_T .

Due to its connection and sensitivity to the constituent parton's spin, the TMDs can also serve as a probe in so called *proton spin puzzle*. In 1987, EMC collaboration in CERN reported an unexpectedly small value of quark contribution to the proton spin and till today, it has been estimated to be approx. 30 %. The proton spin can be decomposed to the contribution from its individual components. Based on the scheme, the decomposition can be for example

$$\frac{1}{2} = \frac{1}{2}\Delta\Sigma + \Delta G + L^q + L^g, \quad (7)$$

where $\Delta\Sigma$ is the quark spin contribution, ΔG is the gluon spin contribution, and L^q, L^g are the contributions due to the orbital angular momentum of quarks and gluons. Since TMDs provide a correlations of transverse motion with the quark spin and orbital motion, the five off-diagonal TMDs would vanish for zero orbital momentum of partons.

2.3 Generalized parton distributions

Apart from the transverse momenta, we can also consider the intrinsic transverse positions b_x, b_y of partons with respect to the center of the proton. The parton distributions are then described by 3D functions $f(x, \vec{b})$ called impact-parameter distributions. By using the fact, that the impact parameter \vec{b} is a Fourier conjugate variable to the momentum transfer $\vec{\Delta}$, where $\vec{\Delta}^2 = -(P - P')^2 \equiv -t$, we can construct functions called *generalized parton distributions* (GPD). In the simplest approach, there are six GPDs and as in the case of TMDs, these functions give information

about (un)polarized partons in an (un)polarized nucleon. These functions provide a unification of the concepts of parton distributions and hadronic form factors and are also connected to the orbital angular momentum of partons. In a special case, where we consider zero t and longitudinal momentum fraction ξ , we can obtain standard unpolarized quark PDF and also quark helicity $\Delta q(x)$. These functions are also related to the elastic form factors, which can be obtained by integrating over x . The GPDs can be measured in several suitable exclusive processes, e.g. exclusive vector meson production, or in the so called deep virtual Compton scattering.

Both aspects – momentum and position – of the structure of the proton in the transverse direction can be unified under a common framework of Wigner distributions. These are five-dimensional phase space distributions of partons from which both GPDs and TMDs, and subsequently also collinear PDFs, can be derived. The Wigner distribution is therefore often called a "mother distribution function". An overview of the relation between the above described distributions can be seen in Figure 36.

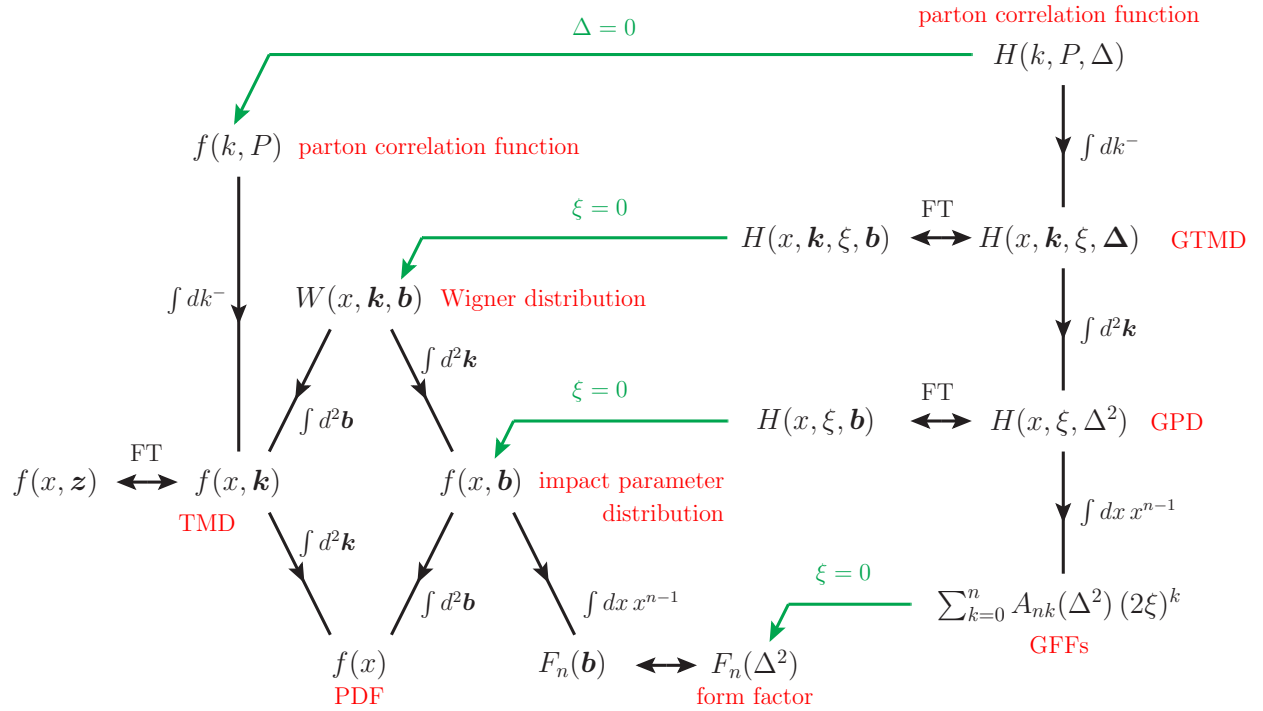


Figure 7: A schematic overview of parton distributions depicting transitions between various functions. Figure taken from [1].

3 Summary

Using specific parton distributions, various observables and effects can be quantified. The distributions can provide information on partonic structure of the proton from different points of view. Therefore a "tomography" of the proton structure can be done in terms of parton's intrinsic momentum, positions, and orbital movements. We can therefore answer such important questions as "How is the overall proton momentum distributed among partons?", "How do they move inside the proton?", "Where are they located?", "Do they carry orbital angular momentum?", "How do they contribute to the proton spin?", etc, and find out the origin of the measured properties of the proton (and other hadrons). There are wide experimental efforts and future plans focused on the solving the puzzle. Many important measurements have been performed in the past or are currently still active at experiments in CERN (EMC Collaboration, COMPASS experiment), JLab, BNL, or in DESY(H1, ZEUS, HERMES). There are also ambitions plans for future experimental

facilities where the above introduced effects could be measured. The probably most famous is a planned electron-ion collider in US [2].

To conclude, the well known concept of collinear PDFs measured in Deep inelastic scattering was introduced in this contribution. An interested reader can find detailed derivations of the relations stated in the text and also further explanations of the introduced concepts in references [3, 4]. Apart from this well-known concept, the more general distributions of partons in the hadrons were introduced. These are polarized PDFs, which account for (anti)aligned quark spin with the proton polarization. Also distributions of transverse momenta, the problem of the origin of the proton spin, and the distributions quantifying transverse positions of partons were introduced. More information about these distributions can be found in references [1, 5, 6].

References

- [1] Diehl, M., *Introduction to GPDs and TMDs*, Eur. Phys. J. A (2016) 52: 149.
- [2] Accardi, A., et al., *Electron-Ion Collider: The next QCD frontier*, Eur. Phys. J. A52, no. 9, 268 (2016).
- [3] Halzen, F., Martin, A.D., *Quarks and Leptons, An Introductory Course in Modern Particle Physics*, 1984. ISBN: 978-0-471-88741-6
- [4] Chyla, J., *Quarks, partons and Quantum Chromodynamics*.
- [5] Bacchetta, A., talk given at EINN2017.
- [6] Hatta, Y., lectures given at CFNS Summer School 2019.

SYSTEMATIC UNCERTANTY OF MASS COMPOSITION OF COSMIC RAYS INTERPRETED FROM MEASUREMENTS OF DEPTH OF SHOWER MAXIMUM USING DIFFERENT MONTE CARLO GENERATORS

Karolína Syrová

1 Introduction

The mass composition of cosmic rays plays a crucial role in the knowledge of the origin of high-energy cosmic rays. [1] Mass spectrum of energies up to 10^{14} eV can be measured directly, whereas for higher energies, one observes extensive air showers (EAS), where the mass of the primary particle can only be obtained from comparisons of experimental observables with air shower simulations. These, however, are subject to uncertainties of hadronic interactions at the highest energies, especially for energies higher than those attainable at particle accelerators. This means that for energies above 10^{20} eV, accelerator data need to be extrapolated. The model uncertainties are the dominant source of systematic uncertainties of the mass composition at the highest energies.

By producing simulations of 5000 showers for different primaries (protons, helium, oxygen and iron nuclei) and fitting the distributions of shower maximum X_{max} at the Pierre Auger Observatory (PAO) using the generated distribution for each primary, one can estimate the fractions of fitted primaries. Simulations were run on the computer farm Goliáš of the Institute of Physics of the Czech Academy of Sciences. The simulation programme is CORSIKA compiled with hadronic interaction models Sibyll 2.3c, EPOS LHC and QGSJET-II 04. The energy range for the simulations is $10^{18} - 10^{19.5}$ eV, and four different atmosphere models are also used in these simulations, along with already existing CONEX simulations in the Goliáš computer farm.

2 Models of hadronic interactions

The selection of a model of hadronic interactions affects resulting observables of the shower, changing the number of muons produced or the depth of the shower maximum. When drawing conclusions of the mass composition, it is important to know which models describe experimental data with best accuracy. Usually more than just one hadronic interactions model is used when identifying the composition of experimental data.

2.1 Sibyll 2.3c

Sibyll is one of the first hadronic interactions models created specifically for the interpretation of the cosmic ray data. [2] This event generator combines the simulation of hadronic particle production with quantum chromodynamics predictions and its development started already in the late 1980. Sibyll uses Hillas splitting algorithm, one of the first Monte Carlo air shower packages, and has fully implemented minijet model, which allows for several independent parton pairs interacting in one single hadronic collision. A large quantity of shower simulations were done with Sibyll, most importantly all simulations used for designing PAO.

From the history of air shower simulations, this model uses simplifications affecting the results in a way that makes it inferior to other, more advanced models. On the other hand, these simplifications shorten the time needed to compute the shower. The newer version Sibyll 2.3c is used in the above mentioned simulations.

2.2 QGSJET-II 04

The QGSJET model uses Quark-Gluon String model and enhanced Pomeron diagrams. [4] This model was developed mainly because of the new strategy of data analysis, mainly put forward by the KASCADE experiment. Regarding these advancements, QGSJET became one of the models best describing accelerator data, and therefore became very popular. Compared to QGSJET-01, the newer version has reduced secondary particle production, and has deeper shower maxima. The greatest disadvantage of this model is its complexity, making it susceptible to development of mistakes. This model is also, from the three models mentioned, the one describing the PAO experimental data worst.

2.3 EPOS LHC

EPOS is currently one of the most advanced hadronic models to date. [3] While a number of simulations are based on 10 years old models which contradict accelerator data, such as those from RHIC. The Hadronic interactions model EPOS LHC takes into account nuclear interactions during the collisions, fits well data from RHIC and LHC. This model produces more muons on ground than the previously mentioned QGSJET-II 04 or Sibyll 2.1, but still less than Sibyll 2.3c. The cost of such sophisticated model has, however, somewhat longer simulation time, especially in the simulation program CORSIKA, rendering this model not very practical for quick computations.

3 Simulation programs

3.1 CONEX

CONEX is one-dimensional hybrid air shower simulation program. [5] This means that the shower is described using cascade equations, using Monte Carlo only at the most energetic part of the shower. This strategy reduces the computation demands. While this hybrid approach is the main idea of CONEX, it can run in full Monte Carlo mode.

3.2 CORSIKA

CORSIKA, short for COsmic Ray SIMulations for KASCADE, is a Monte Carlo program for high energies [6]. It creates three-dimensional simulations that have higher demands on computation time with higher energies of the primary particle than in the case of CONEX. To reduce these demands, CORSIKA has so-called thinning energy E_{thin} , from which it does thin sampling. Thinning means that CORSIKA explicitly simulates only a small fraction of all particles and assigns them a weight factor. When the shower reaches the phase where a great number of particles is produced, one of the secondary particles is randomly selected as a representative of the rest, which is discarded. This approach reduces computing time but raises uncertainties of observables, meaning that the optimal E_{thin} needs to be selected for the individual purposes of a simulation.

References

- [1] K.-H. Kampert, M. Unger. Measurements of the Cosmic Ray Composition with Air Shower Experiments. *Astropart. Phys.* 35 (2012) 660..
- [2] Engel, Ralph & Riehn, Felix & Fedynitch, Anatoli & Gaisser, Thomas & Stanev, Todor. (2017). The hadronic interaction model Sibyll – past, present and future. EPJ Web of Conferences. 145. 08001. 10.1051/epj-conf/201614508001.
- [3] T. Pierog, K. Werner. EPOS Model and Ultra High Energy Cosmic Rays. *arXiv preprint arXiv:0905.1198v1 [hep-ph]*, 8 May 2009.

- [4] Ostapchenko, S. hadronic Interactions in QGSJET-II: Physics and Results, 2005 <https://cds.cern.ch/record/965306>
- [5] T. Bergmann, R. Engel, D. Heck, N. N. Kalmykov, S. Ostapchenko, T. Pierog, T. Thouw, K. Werner. One-dimensional Hybrid Approach to Extensive Air Shower Simulation *arXiv preprint arXiv:astro-ph/0606564v1*, 22 Jun 2006
- [6] Heck, D. and Knapp, J. Upgrade to the Monte Carlo Code CORSIKA to Simulate Extensive Air Showers with Energies $> 10^{20}$ eV. In *Spring Meeting of the Germany Physical Society (DPG) on Particle Physics (In German) Freiburg, Germany, March 23-27, 1998*. <http://bibliothek.fzk.de/zb/berichte/FZKA6097.pdf>.

MEASUREMENT OF DOUBLE DIFFERENTIAL JET SUBSTRUCTURE IN P+P COLLISIONS AT $\sqrt{s} = 200$ GeV AT STAR

Georgij Ponimatkin

1 Introduction

Jet substructure measurements play an important role in the theoretical as well as experimental understanding of parton shower evolution both in vacuum and dense nuclear medium. Previously the STAR experiment provided results [1] on groomed shared momentum fraction (z_g) and jet mass measurements in p+p collisions at $\sqrt{s} = 200$ GeV, which serve as an important baseline. In this article, we show first results on the measurement of double-differential distributions of groomed shared momentum fraction (z_g) and transverse radiation strength ($\log(k_T)$) dependent on jet transverse momentum (p_T) as well as ΔR distance between sub-jets. Such measurements are of a particular interest as they are able to constrain different models of parton shower evolution in vacuum and dense QCD medium [2, 3].

Most of the substructure observables rely on the reclustering of the anti- k_T jet with the Cambridge-Aachen algorithm, which restores the angular ordering of the jet evolution. After that, we look for a split in the jet, such that the condition (called Soft Drop [4])

$$z_g = \frac{\min(p_{T,1}, p_{T,2})}{p_{T,1} + p_{T,2}} > 0.1. \quad (8)$$

If such split exists, the jet is accepted as groomed jet. We also define the $\log(k_T)$ observable, where k_T is defined as

$$k_T = p_{T,b} \sin(\Delta R_{a,b}), \quad (9)$$

where $p_{T,b}$ is transverse momentum of the emission at the split that passes the Soft-Drop condition and $\Delta R_{a,b}$ is a distance between splits in $\eta - \varphi$ plane.

2 Measurement of Double-Differential Jet Substructure

In this analysis we used p+p collisions at $\sqrt{s} = 200$ GeV, recorded by the STAR experiment in 2012 and triggered by the JP2 trigger, which requires presence of at least 8.4 GeV/c of deposited energy in one of the sectors of the electromagnetic calorimeter (BEMC). For jet finding we select charged tracks that lie in $|\eta| < 1$ and have $p_T \in (0.2, 30)$ GeV/c and BEMC clusters with $|\eta| < 1$ and whose E_T after 100% hadronic correction is in the range (0.2, 30) GeV. The jets are then reconstructed with FastJet [5, ?] package using the anti- k_T algorithm [7] with a resolution parameter $R = 0.6$ and reclustered with the Cambridge-Aachen [9, ?]. We select jets for which $20 < p_T^{\text{jet}} < 40$ GeV/c as in this range the JP2 trigger is fully efficient. In order to remove the detector effects from measured variables we utilize 2D Bayesian unfolding [10], unfolding $z_g / \log(k_T)$ and ΔR simultaneously. We use PYTHIA6 [11] model that was tuned to the underlying event that is observed by the STAR experiment to generate particle level and aforementioned events with GEANT3 [12] to generate detector level data in order to construct response matrices. Unfolded spectra for z_g distribution can be seen in Fig. 8 and for $\log(k_T)$ in Fig. 9.

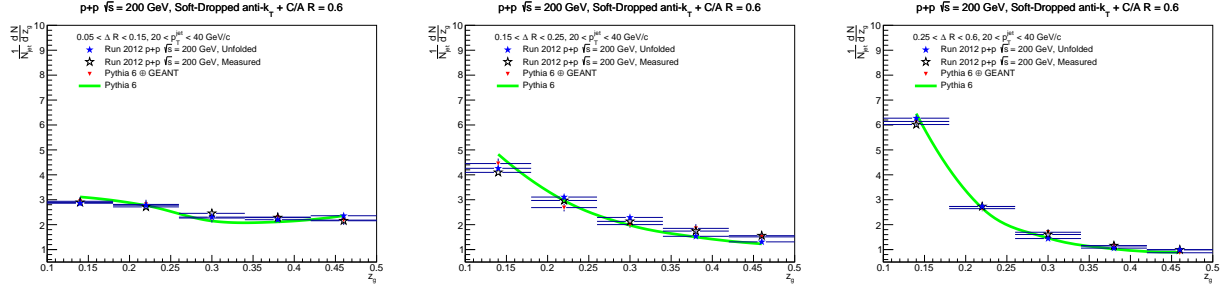


Figure 8: Dependence of z_g distributions measured in p+p collisions at $\sqrt{s} = 200$ GeV on the distance between two subjects ΔR .

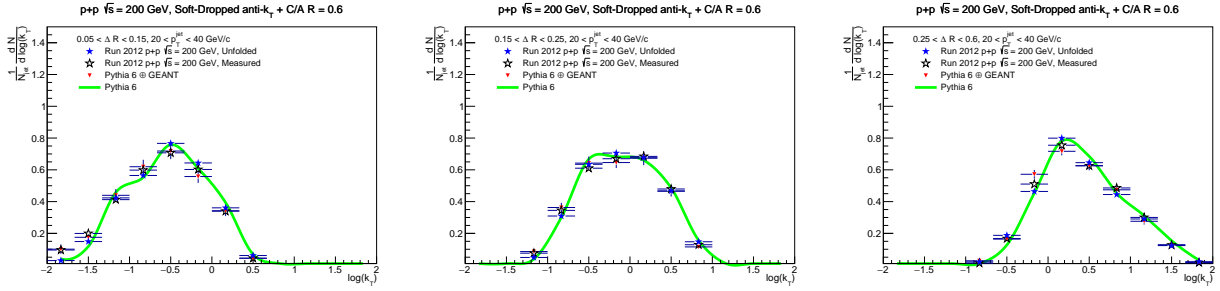


Figure 9: Dependence of $\log(k_T)$ distributions measured in p+p collisions at $\sqrt{s} = 200$ GeV on the distance between two subjects ΔR .

3 Discussion

In this article we presented a preliminary measurements of the double-differential groomed jet substructure. These measurements extend previous jet substructure measurements at STAR by adding the dependence on the splitting angle. From Fig. 8 we see that an increase in the opening angle leads to the softer split, which is consistent with the standard wide angle radiation picture, while the collinear emission leads to the harder split. Fig. 9 on the other hand shows, that the intensity of the transverse radiation is strongest for wide angles, while for the small angles the radiation is softer. In future, we plan to finish the unfolding procedure by taking into the account shifting of the jets in the p_T bins as well as to estimate the systematic errors of the measurement.

References

- [1] R. K. Elayavalli (for the STAR Collaboration). Jet sub-structure and parton shower evolution in p+p and Au+Au collisions at STAR. arXiv:1906.05129 [nucl-ex]
- [2] F. A. Dreyer, G. P. Salam, G. Soyez. The Lund Jet Plane. JHEP 1812 (2018) 064
- [3] Harry A. Andrews et al. Novel tools and observables for jet physics in heavy-ion collisions. CERN-TH-2018-186
- [4] A. J. Larkoski, S. Marzani, G. Soyez, J. Thaler. Soft Drop
- [5] M. Cacciari, G.P. Salam and G. Soyez. FastJet user manual. Eur.Phys.J. C72 (2012) 1896
- [6] M. Cacciari, G.P. Salam. Dispelling the N^3 myth for the k_t jet-finder. Phys.Lett. B641 (2006) 57-61.
- [7] M. Cacciari, G. P. Salam, G. Soyez. The anti- k_t jet clustering algorithm. JHEP 0804 (2008) 063.
- [8] Y. L. Dokshitzer, G.D. Leder, S. Moretti, B.R. Webber. Better jet clustering algorithms. JHEP 9708 (1997) 001.
- [9] M. Wobisch, T. Wengler. Hadronization corrections to jet cross-sections in deep inelastic scattering. arXiv:9907280 [hep-ph]

- [10] G. D'Agostini. A multidimensional unfolding method based on Bayes theorem. NIM A 362 (1995) 487.
- [11] T. Sjostrand, S. Mrenna, P. Z. Skands. PYTHIA 6.4 Physics and Manual. JHEP 0605 (2006) 026.
- [12] R. Brun, F. Bruyant, F. Carminati, S. Giani, M. Maire, A. McPherson, G. Patrick, L. Urban. GEANT Detector Description and Simulation Tool. CERN-W5013.

TIPS AND TRICKS WITH ROOFIT - TUTORIAL

Leszek Kosarzewski

1 Introduction to RooFit

Physics analysis often requires fitting of curves to experimental or simulated data in order to extract yields or estimate backgrounds. RooFit [?, ?] is a very easy to use C++ based package which is well designed for this purpose. In addition it also allows to easily generate data from a model using Monte-Carlo methods. RooFit is a part of ROOT [?] data analysis framework and can be included in ROOT macros. In addition GooFit [?], a version of RooFit utilizing Graphics Processing Units has been developed. It is based on NVIDIA CUDA [?] and increases speed of fitting. For users, there is a very good documentation for RooFit [?] including core documentation [?], a quick start guide [?] and a "RooFit in 20 minutes" webpage [?]. In addition, many examples are located in \$ROOTSYS/tutorials/roofit directory as well as a webpage [?]. An important feature of RooFit is that it's classes reflect mathematical concepts as shown in Fig. 36.

Concept	Math Symbol	RooFit class name
Variable	x, p	RooRealVar
Function	$f(\vec{x})$	RooAbsReal
PDF	$F(\vec{x}; \vec{p}, \vec{q})$	RooAbsPdf
Space point	\vec{x}	RooArgSet
Integral	$\int_{\vec{x}_{min}}^{\vec{x}_{max}} f(\vec{x}) d\vec{x}$	RooRealIntegral
Derivative	dF/dx	RooDerivative
-log(Likelihood)	$-\sum_{data} \log(F(x_i, \vec{p}))$	RooNLLVar
List of space points	\vec{x}_k	RooAbsData

Figure 10: RooFit classes correspond to mathematical concepts [?]

This proceedings briefly illustrates some of the RooFit capabilities useful for fitting.

2 Fitting

2.1 Fitting step by step

Fitting problem typically consists of a few steps:

1. Preparing data in the form of histograms(binned) or datasets and trees(unbinned)
2. Choose a relevant shape of the model, fitting function
3. Determine starting parameters values and limits
4. If needed, constrain the parameters using external constraints from simulation, other fits etc.
5. Perform a maximum likelihood or minimum χ^2 fit and visualize uncertainties
6. Test for goodness of fit, check the correlation matrix for strong correlations and excessive parameters

7. Test different shapes of the model, possibly replace the fitting function
8. Try to vary starting parameters and limits, in order to check the stability or even estimate possible systematic uncertainties

2.2 Using external constraints

If additional information about the model can be gained from a different source like simulation, initial or other fits. Such information can be applied to a fitting problem within RooFit in the form of a multivariate gaussian PDF for the model parameters. In order to extract it from the previous fit a HessePDF has to be obtained from the original fit result. Such a PDF includes correlations between parameters. This can then be used for a subsequent fit by adding ExternalConstraints() to the fitTo() command as shown below.

```
RooAbsPdf *paramPDF = result->createHessePdf(RooArgSet(mean));
RooFitResult *result = model->fitTo(*data,ExternalConstraints(*paramPDF),Save());
```

2.3 Fitting ranges

Various ranges can be defined independently. Each different for different operations. They can even overlap with each other. For example a sum of 2 disjoint ranges can be used for fitting, while a third one can be used to calculation of χ^2 or normalization. A range is defined by:

```
x.setRange("narrow", -5.0, 5.0);
x.setRange("full", -10.0, 10.0);
RooFitResult *result = model->chi2FitTo(*hist,Range("narrow"),Save());
```

3 Testing fits

3.1 Visualizing uncertainties including correlations

When fitting, it is important to visualize uncertainties and take correlations between fit parameters into consideration. After fitting is done, the covariance matrix is stored in the fit result. This matrix can be used to visualize uncertainties using MC sampling when kFALSE option is selected. If kTRUE is set, then a linear propagation method is used, which fails in the presence of strong correlations.

```
gauss->plotOn(frame, NormRange("narrow"),Range("full"),VisualizeError(*result,1),kFALSE);
result->Print(); // Print results
result->correlationMatrix().Print(); // check correlations!
```

Also, the printout from the fit result allows to check if the fit succeeded or if a parameter hit a limit. Printing the correlation matrix allows to look for redundant parameters, which usually exhibit strong correlations.

3.2 Chi-square test

One of the basic tests of goodness of fit is χ^2 test. This is complementary to a likelihood fit. The value of χ^2 can be calculated, by first extracting the number of floating parameters and then calculating χ^2 between the last plotted data and model. If needed, both can be specified.

```
int npar = model->getParameters(*hist)->selectByAttrib("Constant",kFALSE)->getSize();
double chi2ndf = frame->chiSquare(npar); // calculate chi2/ndf
```

3.3 Pull

Pulls provide information about how well the data is described by the fit scaled by the uncertainty of the data. Pulls are useful for investigating possible systematic shifts between the data and the model as well as identifying outliers. In order to calculate the pull, the difference between the i -th data point x_i and the value of the fitted model f_i is divided by the uncertainty on the data point $\sigma(x)_i$. This is shown in Eq. 10.

$$g_i = \frac{x_i - f_i}{\sigma(x)_i} \quad (10)$$

In RooFit, a pull is calculated in the following way:

```
RooHist* hpull = frame->pullHist("h_hist", "gauss_Norm[m_{ee}]_Range[full]_NormRange[full]");
```

The arguments of the above function are the name of the histogram and the name of the function respectively.

3.4 Kolmogorov-Smirnov test

The Kolmogorov-Smirnov test [?] is a test evaluating if 2 distributions are compatible. The calculated value is the probability that the compared distributions originate from the same underlying distribution. ROOT implementation compares 2 discrete distributions using histograms.

```
TH1* h_func = model->createHistogram("h_func", x);
TH1* h_data = hist->createHistogram("h_data", x);
double KStest = h_data->KolmogorovTest(h_func);
```

4 Summary

A short example guide to some of the features of the RooFit package was presented along with the guidelines for fitting. It is useful for typical fitting problems encountered during physics analysis. These ideas can be easily generalized to multidimensional fitting. A collection of useful links for reference and further reading is also included.

STUDY OF $\pi^+\pi^-$ AND K^+K^- PRODUCTION IN CENTRAL EXCLUSIVE PROCESSES WITH THE STAR DETECTOR AT RHIC

Tomáš Truhlář

1 Introduction

Central exclusive production (CEP) is gluon-rich environment and it is considered to be a potential source of gluon bound states, called glueballs. The glueball has not been yet unambiguously confirmed, although its theoretical predictions. Its experimental confirmation would be yet another strong support for the validity of the quantum chromodynamics theory.

It is expected that CEP through Double Pomeron¹ Exchange mechanism is dominant at high energies. The Double Pomeron Exchange was first observed at the CERN Intersecting Storage Rings and since then it has been studied at numerous colliders such as the Sp \bar{p} S collider at CERN, the Tevatron at Fermilab, the Relativistic Heavy Ion Collider (RHIC) at Brookhaven National Laboratory and last but not least at the Large Hadron Collider at CERN.

CEP is process $p + p \rightarrow p + X + p$, where the colliding protons emerge intact, and for which all central particles X are fully measured. Furthermore, the outgoing protons are well separated from the produced central state X by rapidity gap $\Delta y > 3$. The diagram of CEP through Double Pomeron Exchange can be seen in Fig. 11.

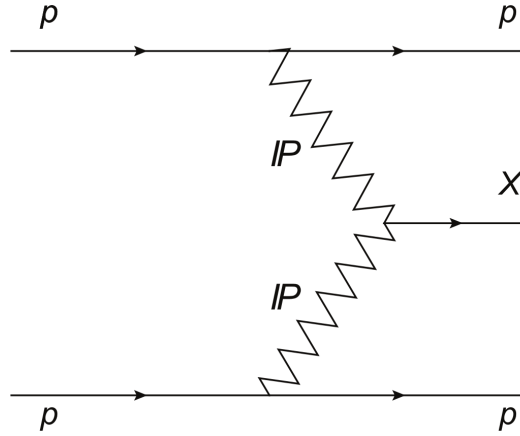


Figure 11: The diagram of central exclusive production through Double Pomeron Exchange. Taken from Ref. [1].

2 Experimental setup

The STAR experiment at RHIC is very suitable for measuring CEP processes, because of its unique capabilities. The tracks of centrally produced system X are reconstructed in the central detector of STAR using high-resolution tracking of centrally produced charged particles in the Time Projection Chamber. Particles are identified using the ionization energy loss and the time of flight method. The diffractively scattered protons, moving intact inside the RHIC beam

¹The Pomeron is color singlet object with internal quantum numbers of the vacuum 0^{++} . However, its exact nature still remains elusive.

pipe after the collision, are measured in the Roman Pots system allowing full control of the interaction's kinematics and verification of its exclusivity. Furthermore, the rapidity gap is ensured by the Beam-Beam Counter detectors covering forward rapidity $2.1 < |\eta| < 5.0$.

The Roman Pots at the STAR experiment is system of forward detectors used to detect and measure forward protons from elastic or inelastic scattering. The current layout of the RP system, called Phanse II*, is shown in Fig. 12. On each site of the interaction point, there are two RP stations at a distance of 15.8 m and 17.6 m. Each station consists of two RP vessels containing Silicon Strip Detector package and a scintillation counter for trigger. The RP detectors are located between DX and D0 dipole magnets and they enable the reconstruction of the proton momentum by measuring the track angle and its position, since the constant and uniform magnetic field of the DX magnet works as a spectrometer.

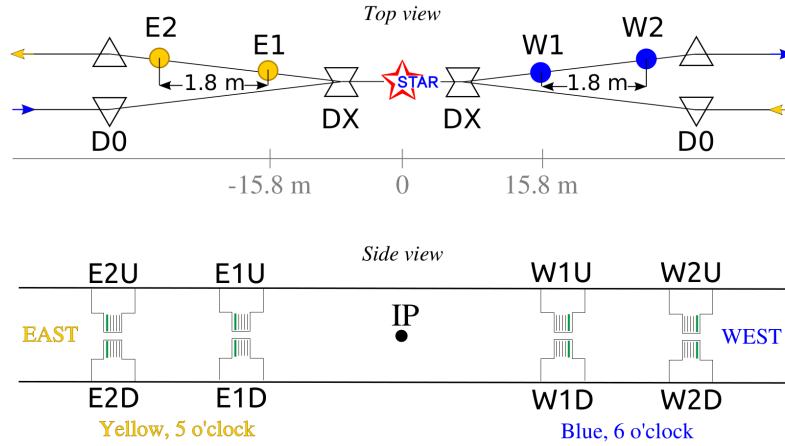


Figure 12: The Roman Pot Phase II* layout. Top view with highlighted Roman Pot stations E1, E2, W1, W2 and dipole magnets DX, D0. Side view with depicted Roman Pots. Taken from Ref. [1].

3 Results in central exclusive production

At present, the CEP processes are studied at the STAR experiment and at CERN experiments: COMPASS, CMS, ATLAS, LHCb and ALICE. However, experiment such as LHCb and ALICE do not measure the outgoing protons and therefore they are not able to measure the exclusivity of the process.

In 2017, The STAR experiment at RHIC measured proton-proton collisions at the center-of-mass energy $\sqrt{s} = 510$ GeV to study CEP $pp \rightarrow pXp$ through Double Pomeron Exchange mechanism. Nevertheless, the results have not yet been approved by the STAR collaboration for public presentation and therefore they cannot be presented here.

The most recent published measurement of CEP with $\pi^+\pi^-$, K^+K^- pairs by the STAR experiment is a measurement in proton-proton collisions at $\sqrt{s} = 200$ GeV [2]. The invariant mass spectra of exclusively produced $\pi^+\pi^-$ and K^+K^- pairs with small squared momentum transfers $0.03 < |t_1|, |t_2| < 0.2$ GeV² can be seen in Fig. 13. The measured $\pi^+\pi^-$ spectrum shows well known features as an rapid increase followed by a sharp drop at 1 GeV/c², attributed to the negative interference with $f_0(980)$ wave, and a bump between 1100 and 1500 MeV/c², considered to be $f_2(1270)$ resonance. These features have been seen in the $\pi^+\pi^-$ spectra since measurement by the AFS Collaboration [3]. However the interpretation of these features is still not clear. The $\pi^+\pi^-$ spectrum was compared to theoretical models of non-resonant CEP that can qualitatively describe data only up to 0.7 GeV/c², which indicates significant role of resonance production. In the K^+K^- spectra, there is a noticeable peak at about 1.5 GeV/c² which can be interpreted as the $f_0(1500)$ state. There is also a bump at about 1.3 GeV/c² which can be the $f_2(1270)$ state, nevertheless the region is well describe by the non-resonance model [2].

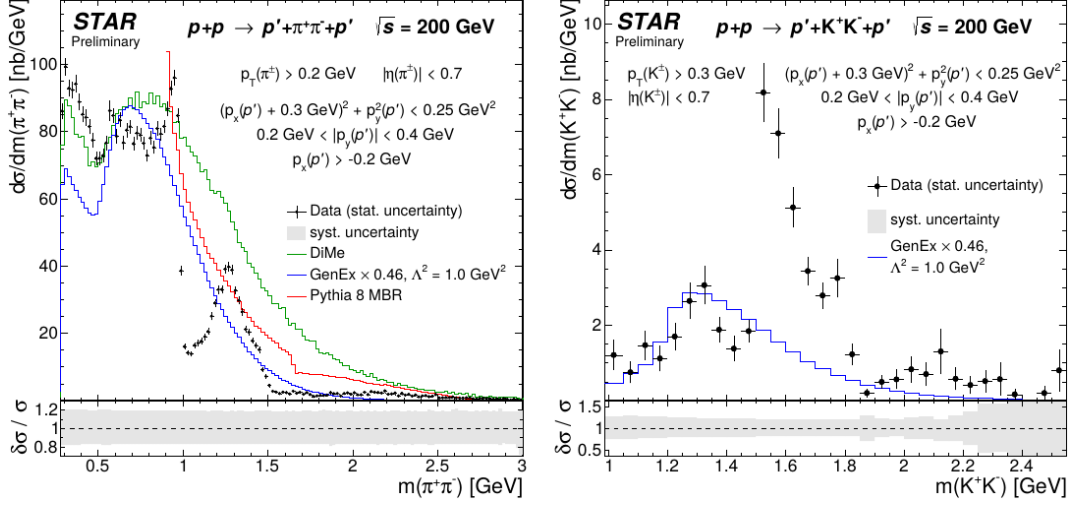


Figure 13: Preliminary results on differential fiducial cross section as a function of invariant mass of $\pi^+\pi^-$ (left) and K^+K^- (right) compared to models. Taken from Ref. [2].

References

- [1] Włodek Guryn, et al. Central Exclusive Production in Proton-Proton Collisions with the STAR Experiment at RHIC. In *EPJ Web of Conferences*, vol. 120, no. 1, p. 5, 2016.
- [2] Rafał Sikora, Recent results on Central Exclusive Production with the STAR detector at RHIC. In *Acta Physica Polonica B Proceeding Supplement*, vol. 2018, no. 1, p. 6, 2018.
- [3] Torsten Akesson, et al., A study of exclusive central hadron production at the ISR as a search for gluonium states. In *Phys. Lett. B* 133 (1983) 268.

PHOTOPRODUCTION OF J/ψ IN ULTRA-PERIPHERAL COLLISIONS

David Grund

1 Introduction

Ultra-peripheral collisions (UPCs) [1] measured at the LHC are of a great importance since they provide an opportunity to study high-energy QCD physics, i.e. with small values of Bjorken- x . In these interactions, the participants collide with an impact parameter b larger than the sum of their radii. Due to the short range of the strong force, the UPC events are induced by virtual photons emitted by one of the participating nuclei. One type of a UPC process is the photoproduction of a vector meson, such as J/ψ , whose differential cross-section is sensitive to the distribution of a target matter in the impact parameter plane. For example, in case of p-A collisions, one can thus probe the gluon distribution of a proton in the low Bjorken- x region.

The first attempts to examine the structure of hadrons, which paved the way for the origin of QCD physics, were the deeply inelastic scattering experiments carried out at the end of the 1960s. According to early results and observed Bjorken scaling of the structure functions, hadrons were believed to be composed of point-like constituents named partons. Later, based on further experimental observations, partons were identified with quarks, introduced independently by M. Gell-Mann and G. Zweig in 1964. Currently it is known that Bjorken scaling is only an approximate phenomenon (when $x \sim 0.1$), meaning the structure of hadrons evolves and becomes finer with increasing energy of a lepton probe. The structure functions of hadrons are expressed in terms of parton distribution functions (PDFs) which describe the quark and gluon content. Gluon saturation, which is eventually expected to occur in a region with sufficiently low Bjorken- x , is nowadays not fully understood and needs to be accessed experimentally.

2 Vector Meson Photoproduction

Since the photon flux created by a moving nucleus is proportional to Z^2 , the photons are considered to be emitted only by the heavy nuclei in both p-A and A-A collisions. Types of the photoproduction can be categorized as follows:

- p-A collisions:
 - *Exclusive*: the target proton does not break up after the interaction, the transverse momentum p_T of the J/ψ is roughly 300 MeV/c.
 - *Dissociative*: the proton is excited and is dissociated. The produced system thus can have p_T higher than 1 GeV/c.
- A-A collisions:
 - *Coherent*: the photon interacts coherently with the whole nucleus which does not break up. The final p_T of the J/ψ is rather small (around 60 MeV/c).
 - *Incoherent*: the photon interacts with the inner structure of the nucleus (with a nucleon). The target nucleus breaks up and the p_T of the produced J/ψ is approximately 300 MeV/c.

The created J/ψ is typically measured via its di-leptonic decay. The cross section of the J/ψ photoproduction is factorized into the emission of a virtual photon by a heavy nucleus (photon flux) and the subsequent interaction of the photon with a target proton or nucleus. The latter can be modelled e.g. using the colour dipole model in which the photon fluctuates into a quark-antiquark pair that interacts with the target by the strong interaction. It is then the

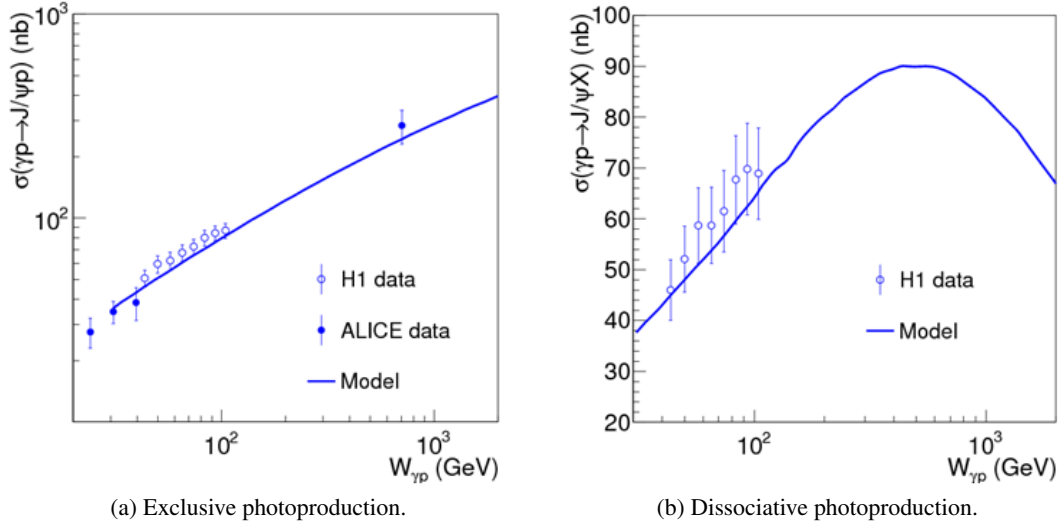


Figure 14: The total cross section of the J/ψ photoproduction as a function of centre-of-mass energy of the photon-proton system. Model (solid lines) is compared to experimental results (bullets). Figures are taken from [2].

amplitude of the photon-target cross section which carries the information about the transverse structure of a target, $T(\vec{b})$, where \vec{b} is the oriented impact parameter.

3 Energy-dependent hot-spot model

An energy-dependent hot-spot model [2, 3] aims to employ rather simple description of the transverse structure of the hadrons which would be efficient in describing the cross sections of the photoproduced J/ψ . The results of this model were compared to data from ALICE, H1 or RHIC on γ -p and heavy ion collisions.

3.1 γ -p collisions

In this approach, the transverse structure of a proton is thought to be a sum of N_{hs} high gluon density hot spots with Gaussian distributions. Positions of the hot spots themselves are chosen randomly with a Gaussian distribution centred at $\vec{b} = (0, 0)$ and corresponding to the size of a proton. The important contribution of this model is that the number of hot spots N_{hs} grows with decreasing Bjorken- x as

$$N_{hs} = p_0 x^{p_1} (1 + p_2 \sqrt{x}) \quad (11)$$

where p_i are parameters and p_1 is negative. This evolution reflects the experimental data on the PDFs.

Besides being able to describe the energy dependence of the exclusive J/ψ photoproduction (see Fig. 14-a), the model predicts a saturation of the dissociative cross section at $W_{\gamma p} \approx 500$ GeV followed by a steep decrease (see Fig. 14-b). This corresponds to ca. 10 hot spots present in a proton, meaning a sizeable overlap occurs. Being within the energy range of the LHC, the measurement of the dissociative cross section has a potential to provide a signature for gluon saturation.

3.2 Pb-Pb collisions

The extension to photonuclear interactions is carried out employing the Glauber-Gribov formalism (GG) or geometrical scaling (GS). The former relates the dipole-proton cross section to dipole-nucleus cross section using the transverse nuclear profile $T_A(\vec{b})$, while the latter completely factorizes the \vec{b} dependence ($T_A(\vec{b})$) from the x -dependence.

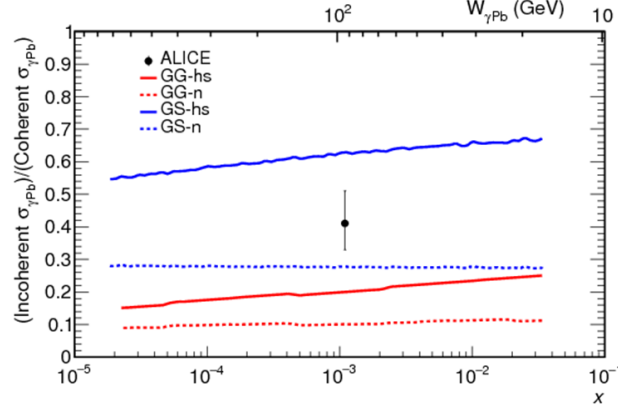


Figure 15: The ratio of the incoherent to the coherent cross section as a function of Bjorken- x or centre-of-mass energy $W_{\gamma\text{Pb}}$. Figure is taken from [3].

The fluctuating transverse nuclear profile is modelled in two ways. Either the nucleus is regarded to be composed of A nucleons only (n) or the subnucleonic degrees of freedom are included, where each nucleon is composed of N_{hs} Gaussian hot spots (hs). Again, the number of hot spots evolves with Bjorken- x as in (11). The model again succeeds in describing the x -dependence of both the coherent and the incoherent J/ψ cross sections as well as their rapidity dependencies. In the incoherent case, it appears that the inclusion of hot spots leads to better agreement with experimental data.

However, one of the key results is that the existence of subnucleonic structure introduces the x -dependence of ratio of the incoherent to the coherent cross section as can be seen in Fig. 15. Without considering the subnucleonic structure, this ratio would be constant. To verify this dependence, more data on the incoherent cross section with smaller uncertainties are needed.

4 Conclusion

The importance of the vector meson photoproduction in ultra-peripheral collisions lies in its sensitivity to the structure of hadrons and nuclei. Measurements of the photoproduction cross sections can help us accessing several predicted QCD phenomenons, such as gluon saturation. One of the goals of future work will be to obtain new data on the incoherent J/ψ photoproduction which could make the predictions of an energy-dependent hot-spot model more accurate.

References

- [1] J.G. Contreras, J. D. Tapia Takaki: Ultra-peripheral heavy-ion collisions at the LHC, *International Journal of Modern Physics A* 30(8), 1542012 (2015).
- [2] J. Cepila, J. G. Contreras, J. D. Tapia Takaki: Energy dependence of dissociative J/ψ photoproduction as a signature of gluon saturation at the LHC, *Phys. Lett. B* 766, 186-191 (2017).
- [3] J. Cepila, J. G. Contreras, M. Krelina: Coherent and incoherent J/ψ photonuclear production in an energy-dependent hot-spot model, *Phys. Rev. C* 97(2), 024901 (2018).

INFLUENCE OF MODIFICATED HADRONIC INTERACTIONS ON PROPERTIES OF COSMIC-RAY SHOWERS

Nikolas Denner

1 Introduction

Cosmic-ray physics is filled with a lot of unanswered questions. One of these questions is the behaviour of air showers produced by collisions of primary particles with Earth's atmosphere. Energies of such collisions are much bigger than those accessible on particle accelerators. Thus, the properties of these hadronic interactions are not properly explored and can be described only by extrapolations of accelerator measurements, made by various phenomenological models. Also, Monte Carlo generators are used to simulate the development of said air showers, but the model uncertainties of such simulations are very hard to estimate.

My thesis deals with Monte Carlo generator CONEX in which cosmic-ray showers with various primary parameters are simulated and afterwards some of the generated observables (e.g. shower maximum or muon number) of these showers are compared. Also, it compares new results with results of Ralf Ulrich published in [?]. The study of relation between modifications of primary parameters and air shower properties leads to knowledge about how the systematic uncertainties of air shower productions influence the predictions for different air shower observables.

2 The Pierre Auger Observatory

The largest facility studying secrets of high-energy cosmic ray physics is the Pierre Auger Observatory. It consists of 1660 surface detector stations and 27 fluorescence telescopes covering an area of 3000 km² in western Argentina. [?] The idea of developing a very large detector was first brought up by Jim Cronin and Alan Watson on the International Cosmic Ray Conference in Dublin in 1991. [?] The construction itself began in 2000 and lasted 8 years, during which time the observatory has already started getting physical results.

The Pierre Auger Observatory uses two independent methods for detection of high-energy cosmic rays. Surface detectors are water tanks placed 1.5 km away from each other. They can measure the energy of incoming particles through production of Cherenkov light in the water and the direction the cosmic ray shower came from by slight differences in detection time in different tanks. Fluorescence telescopes, on the other hand, are situated in 4 places and are able to observe the development of the shower through ultraviolet light emitted by charged particles interacting with atmospheric nitrogen.

3 Modified interactions

3.1 CONEX

CONEX is a code used for simulation of shower profiles which combines Monte Carlo simulation of high energy interactions with a fast numerical solution of cascade equations. [?] For primary parameters, such as energy logarithm, high energy interaction model or particle type, the program calculates for example energy deposit profile or charged particle longitudinal profile. These profiles as well as fits and other results are then written to a ROOT tree. Available high energy hadronic interaction model are EPOS LHC, QGSJETII-04, QGSJET01 and SIBYLL 2.3c.

3.2 CONEX extension

Ralf Ulrich came up with the extension of CONEX which uses the equation

$$f(E, f_{19}) = 1 + (f_{19} - 1)F(E), \quad (12)$$

where

$$F(E) = \frac{\log_{10}(E/1PeV)}{\log_{10}(10EeV/1PeV)}, \text{ for } E > 1PeV, \quad (13)$$

to extrapolate characteristics of hadronic interactions, such as cross-section, multiplicity or elasticity. [?] The extension adds primary parameter f_{19} from (12) for mentioned characteristics. With this, f_{19} can be used as a variable and one can observe how the generated air shower properties depend on its different values.

3.3 Conclusions of Ralf Ulrich's research

After generating 1000 proton and iron showers with energy of $10^{19.5}$ eV for each chosen value of f_{19} , graphs for every relevant observable in dependence on f_{19} for various characteristics of hadronic interactions were plotted. [?] Some of the most important conclusions of these simulations are summarized in following points:

- Fluctuations in shower maximum is a good parameter to study hadronic cross-sections at ultra-high energies.
- Secondary particle multiplicity strongly influences electron and muon number ratio in air showers.
- The dependence of air shower observables on mass of the primary particle has similar magnitude as the influence of the extrapolation of hadronic interaction characteristics on these observables.

HEAVY-ION COLLISIONS AND LAMBDA HYPERON POLARIZATION

Ondřej Lomický

1 Heavy-ion collisions

Heavy ion collisions lead to formation of a relatively new state of matter where quarks and gluons are deconfined, ie. the quark-gluon plasma (QGP). The collisions at different energies enable exploration of different regions of the QCD phase diagram which can be seen in Figure 16. There are three states of matter: the hadronic matter, the QGP and the colour superconductor. The critical point which is represented by the yellow point is defined as a value of the temperature and the baryon-chemical potential at which the QGP and the hadronic matter cannot coexist. The red dashed line represents a crossover and the green solid line shows the first order transition. However, this point is still not sufficiently explored and the existence of the first order transition is a result from QCD lattice.

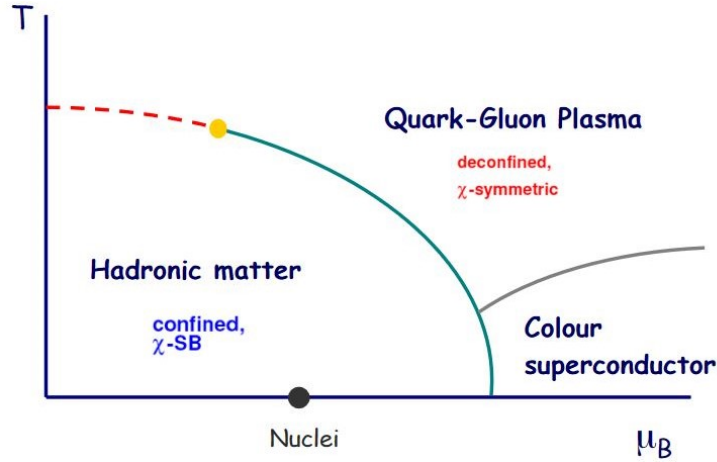


Figure 16: The QCD phase diagram where T is temperature and μ_B is baryon-chemical potential [1].

The existence of the QGP can be confirmed by several measured parameters. The medium effects can modify scaling of the produced high p_T particles. Therefore one of the important parameters is a modification factor

$$R_{AA} = \frac{1}{\langle N_{coll}^{AA} \rangle} \frac{\frac{d^2 N^{AA}}{dp_T d\eta}}{\frac{d^2 N^{PP}}{dp_T d\eta}}, \quad (14)$$

which is a ratio between the number of produced particles in A+A collision and in P+P collision, scaled by the mean number of A+A collisions. The value of R_{AA} equals 1 when there is no medium effect.

The next example of a phenomenon which is related to presence of the QGP is jet quenching. Jets, which can be occur in the heavy-ion collisions, are groups of particles with relative similar distance in momentum space. On account of the conservation of momentum, another jet is created on the opposite side of the first jet, being called away-side

jet. If the QGP is not created, the away-side jet is approximately as significant as the first jet. For instance, in Au+Au collision, there is the away-side jet substantially suppressed, as can be seen in the Figure 17. The phenomenon where the jet is absorbed in a dense medium is called jet quenching.

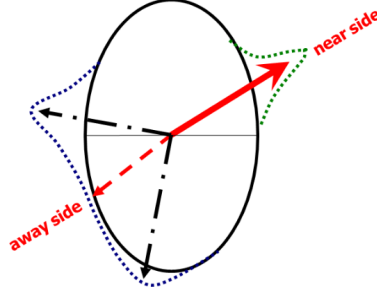


Figure 17: Schematic view of the path length difference for the two shoulders associated with away-side when trigger is selected at an angle relative to the reaction plane (indicated by the horizontal line) [2].

2 Hyperon Λ polarization

Hyperons are baryons containing one or more strange quarks, but no charm, bottom or top quarks – specifically the Λ hyperon consists of u-, d- and s-quark. It was first discovered in 1950 by V. D. Hopper and S. Biswas of the University of Melbourne. The most important decay channels (branching fraction $(63.9 \pm 0.5) \%$) for Λ and $\bar{\Lambda}$ are $p + \pi^-$ and $\bar{p} + \pi^+$, respectively. These daughter particles are identified by using dE/dx information from the TPC and the time-of-flight information from the TOF detector.

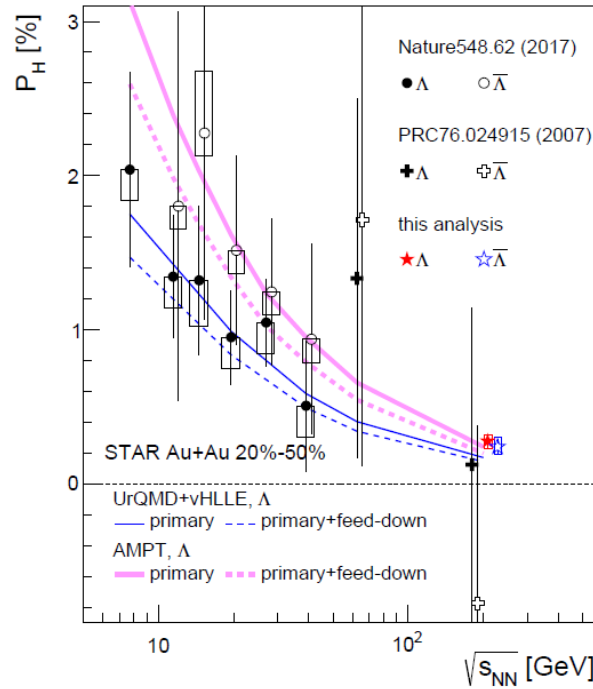


Figure 18: Global polarization of Λ and $\bar{\Lambda}$ as a function of the collision energy $\sqrt{s_{NN}}$ for 20-50% centrality Au+Au collisions [3].

Polarization of Λ hyperon opens new direction in the study of the hottest, the least viscous and the most vortical fluid ever observed. A polarized particle is defined as a particle whose spin is aligned with a certain direction. The Λ particles have the interesting property - they are self-analysing. It means that their polarization is aligned with the overall angular momentum of the QGP. The degree of the polarization P_H is obtained by

$$P_H \equiv \frac{8}{\pi\alpha_H} \frac{\langle \sin(\Psi_1 - \phi_p^*) \rangle}{Res(\Psi_1)}, \quad (15)$$

where the subscript H is specific for Λ and $\bar{\Lambda}$, $\alpha_\Lambda = -\alpha_{\bar{\Lambda}} = 0.642 \pm 0.013$, Ψ_1 is an azimuthal angle of the angular momentum of the first-order event plane, ϕ_p^* is an azimuthal angle of the daughter p momentum in the Λ or $\bar{\Lambda}$ frame and $Res(\Psi_1)$ means resolution of the Ψ_1 .

The results of three measurements of polarization P_H of the Λ hyperon can be seen in Figure 18. The oldest one did not reveal clearly the polarization because of the high error of the measurement. But the two newer measurement reveal polarization with decreasing tendency for increasing energy of the collision. The results also indicate a vorticity of the QGP of $\omega \approx (9 \pm 1) \times 10^{21} \text{ s}^{-1}$ which is the highest known vorticity in the universe.

References

- [1] Ncatlab.org. (2019). Quark-gluon plasma in nLab. [online] Available at: <https://ncatlab.org/nlab/show/quark-gluon+plasma> [Accessed 12 Jan. 2020].
- [2] InSPIRE, (2009). [online] Available at: <http://inspirehep.net/record/815778/plots> [Accessed 12 Jan. 2020].
- [3] Anon, (2018). Researchgate. [online] Available at: https://www.researchgate.net/publication/325118641_Global_polarization_of_Lambda_hyperons_in_AuAu_collisions_at_sqrts_NN_200_GeV [Accessed 12 Jan. 2020].

STUDY OF CHARM QUARK PRODUCTION IN JETS

Jitka Mrázková

1 Introduction

The aim of the following text is to introduce the main subject of my bachelor's degree project. First of all, it would be appropriate to introduce a term jet. Jet is a collimated spray of energetic hadrons, which has an origin in partons that went through fragmentation and hadronization. Jets are used for a wide range of physics analyses for example identification of heavy particles (e.g. Higgs boson, top-quark) and tomographic study of the quark-gluon plasma in high-energy heavy-ion collisions. They can also provide important tests for Quantum-Chromodynamics (QCD) calculations.

There are three different types of jets: parton-level jet (described by pQCD), particle jet (a collection of hadrons) and calorimeter jets, which are registered by a detector. The goal of experimenters is to find a link between those types of jets.

2 Jet algorithms

Jet is defined by a jet algorithm – a set of rules for grouping particles into jets. The ideal jet algorithm should satisfy the following conditions: maximal reconstruction efficiency, order independence (the same jets are found at parton, particle, and detector level), infrared and collinear safety (algorithm should be insensitive to soft radiation and should also find jets that are insensitive to collinear radiation) etc.

There are two broad categories of jet algorithms: *cone algorithms* and *sequential recombination jet algorithms*. An example of the former type of algorithm is an infrared safe SIScone algorithm. Cone algorithms are based on the interpretation of jets as cones with their axes in the direction of dominant energy flow. Sequential recombination jet algorithms, for example k_T and anti- k_T algorithms, depend on distance measures. They introduce distances d_{ij} between entities (particles and pseudojets) and a distance d_{iB} between entity and beam and choose the smallest of the distances. They are (for k_T , anti- k_T algorithm ...) defined as follows:

$$d_{ij} = \min(p_{Ti}^{2k}, p_{Tj}^{2k}) \frac{\Delta_{ij}^2}{R^2}, \quad (16a)$$

$$d_{iB} = p_{Ti}^{2k}, \quad (16b)$$

where $\Delta_{ij}^2 = (y_i - y_j)^2 + (\phi_i - \phi_j)^2$, p_{Ti} , y_i and ϕ_i are respectively the transverse momentum, rapidity and azimuth of particle i . R is the radius parameter and the parameter k is associated with the particular type of algorithm and governs the relative power of the energy versus geometrical scales.

3 Study of charm quarks in jets

Study of charm quark production in high-energy collisions allows us to carry out tests of QCD theory. According to the perturbation theory, one can distinguish two different types of c-quark production: direct charm flavour creation

processes ($gg \rightarrow c\bar{c}$ and $q\bar{q} \rightarrow c\bar{c}$) and higher order processes (e.g. gluon splitting $g \rightarrow c\bar{c}$). The latter processes are not negligible in the charm production and may be an interesting subject of study.

Let us now focus on the experiment “Measurement of the production of charm jets tagged with D^0 mesons in pp collisions at $\sqrt{s} = 7$ TeV” [3], which was conducted at the LHC by ALICE collaboration. The following description of this experiment will reveal some of the methods of analysis that will make a part of my project in the future.

In order to study the heavy quark production and fragmentation, the jets containing charm hadrons were reconstructed. Charm jets were identified by the presence of a D^0 meson among their constituents (D^0 -tagging). The D^0 mesons were reconstructed via their hadronic decay $D^0 \rightarrow K^-\pi^+$ with a branching ratio of $(3.89 \pm 0.04) \%$ and the transverse momentum interval $3 < p_{T,D} < 30$ GeV/c according to the detector acceptance and the reconstruction efficiency. As for the jet reconstruction, it was performed with the anti- k_T algorithm ($R = 0.4$, transverse momentum interval $5 < p_{T,jet} < 30$ GeV/c and $|\eta_{jet}| < 0.5$) [3].

The jet raw yields were extracted with an invariant mass analysis of the D^0 mesons. Figure 19 shows the invariant mass distribution with the peak region (red area) and side-band region (green area). The side-band region is considered to be far enough from D^0 meson peak to be signal-free. The raw yield was (basically) gained by a subtraction of background.

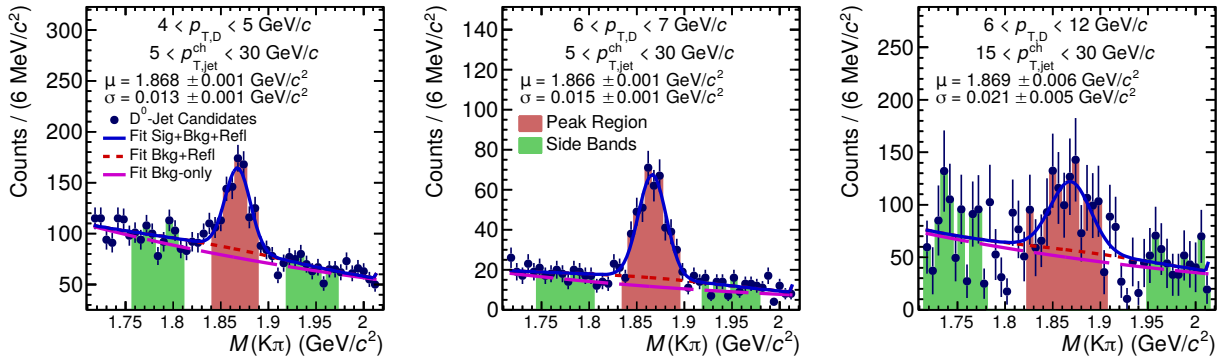


Figure 19: Invariant mass distribution of D^0 -tagged jets candidates with $5 < p_{T,jet} < 30$ GeV/c (left and center) and $15 < p_{T,jet} < 30$ GeV/c (right) [3].

As the next step of analysis, corrections of experimental data were made in four stages (reconstruction efficiency, subtraction of the b-jet contribution, unfolding and systematic uncertainties).

Finally, the figure 20 shows the p_T -differential cross section of charm jets containing a D^0 meson in pp collisions at $\sqrt{s} = 7$ TeV – one of the results of the preceding analysis [3]. All in all, agreement of the measurements with calculations provided by the particular Monte Carlo generators indicates that the studied observables are well described by pQCD.

Future goals of my project include a reconstruction of D-tagged jets using an anti- k_T algorithm on data from RHIC (STAR collaboration). The resulting analysis will be performed without corrections.

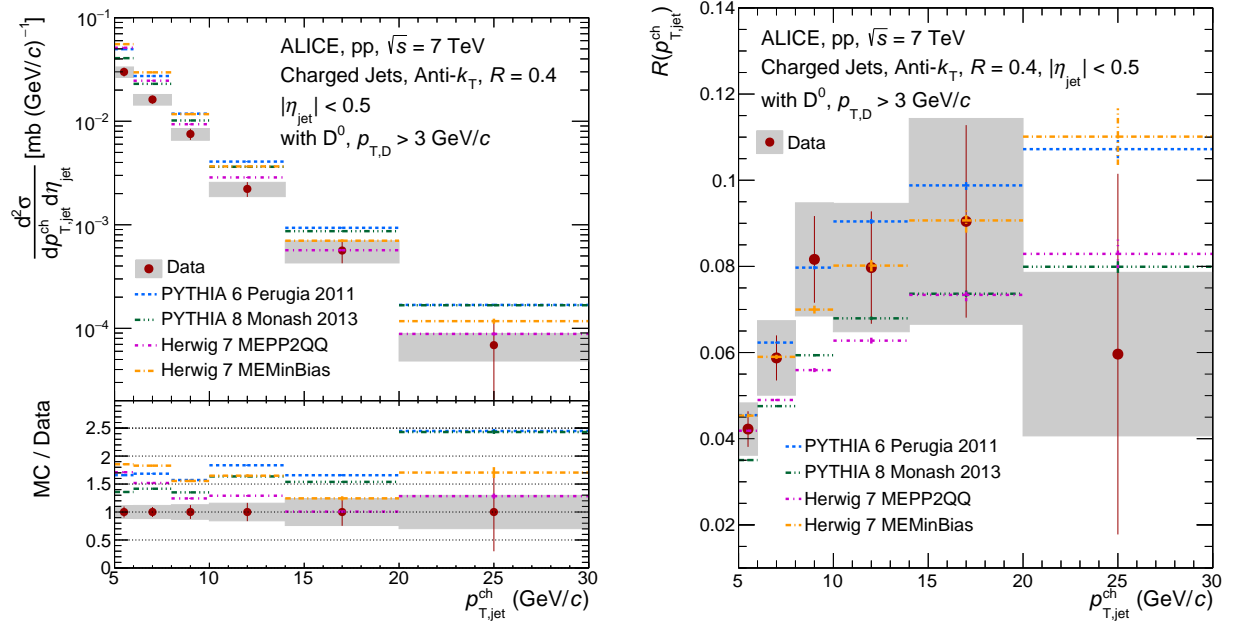


Figure 20: p_T - differential cross section of D^0 -tagged jets (left) and its ratio to the inclusive jet cross section (right) in pp collisions at $\sqrt{s} = 7$ TeV. The measurements are compared with Monte Carlo generators. [3].

References

- [1] Sourav Sarkar, Helmut Satz, Bikash Sinha. The Physics of the Quark-Gluon Plasma (Introductory lectures), pages 285–339. Springer, 2010.
- [2] Matteo Cacciari and Gavin P. Salam, Gregory Soyez. The anti- k_t jet clustering algorithm *arXiv preprint arXiv:0802.1189*, 2008.
- [3] Acharya, S. et al. Measurement of the Production of Charm Jets Tagged with D^0 Mesons in pp Collisions at $\sqrt{s} = 7$ TeV. *arXiv preprint arXiv:1905.02510*, 2019.

STUDY OF COLD NUCLEAR MATTER EFFECTS WITH CHARM MESONS

Michal Svoboda

ABSTRACT: In the collisions of heavy ions at particle accelerators such as RHIC (Relativistic Heavy Ion Collider) in the USA or LHC (Large Hadron Collider) in Switzerland, hot and dense nuclear state called quark-gluon plasma (QGP) is created. There could be found deconfined quarks and gluons during this state. It is expected that same conditions had early universe microseconds after the big bang. QGP can not be observed directly but there could be used its properties with for example nuclear modification factor or elliptic flow. If QGP that appears in heavy ion collisions is supposed to be described correctly, it is important to understand effects caused by the presence of a nucleus called Cold nuclear matter effects (CNM). For the study of these effects collisions of proton-lead (p+Pb) at LHC or proton-gold (p+Au) a deuteron-gold (d+Au) at RHIC are used.

1 Introduction

Quark-gluon plasma (QGP) is a hot and dense state that may be created in ultrarelativistic collisions of heavy ions. Protons are collided in p-p collisions which serve as baseline for collisions of ions (A-A). However, quantitative understanding of the effects of heavy nuclei in the initial stage is needed for studying of QGP properly. For this are used proton-nucleus (p-A) collisions. It is expected that energy density in these collisions is low to produce thermalized medium but still this dense environment could alter participants in the collision.

These CNM effects are studied in proton-gold (p-Au) and deuteron-gold (d-Au) collisions at the Relativistic Heavy Ion Collider (RHIC) in the Brookhaven National Laboratory (BNL) and in proton-lead collisions at Large Hadron Collider (LHC) in CERN.

For description and comparison of particle production in different systems we use nuclear modification factor. If particle yield in p-A collision of centrality c and particle production in p-p collision with particle production cross section σ_{pp} are compared, nuclear modification factor is defined as

$$R_{pA}^c = \frac{N_{pA}^c}{\langle T_{pA}^c \rangle \sigma_{pp}} \quad (17)$$

where $\langle T_{pA}^c \rangle$ is average overlap function for the pA collision of centrality c . This value is usually obtained with Glauber model. Nuclear modification factor is equal or close to unity if the CNM effects in p-A collision are small. Important role in description of properties of particles has Parton Distribution Function (PDF). It is defined as the probability density for finding a particle with a certain longitudinal momentum fraction x at resolution scale Q^2 . Partons can not be observed as free particles so probability densities can not be obtained directly and are acquired by fitting observables to experimental data.

2 Cold nuclear matter effects

It is expected that heavy quarks are created during hard processes (early stages of collision). This makes them great probe of nuclear matter and its effects. The most important CNM which could be studied with heavy quarks are:

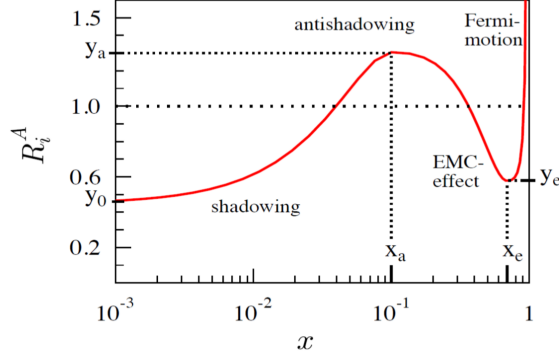


Figure 21: Dependency of the R_i^A on the Bjorken x with different regimes of PDF modification. Taken from [3]

- Modification of effective PDF of nucleons in colliding nuclei, with respect to proton-proton collision - It is expected that dynamics of partons differs in free partons and in nucleus in colliding nuclei. Density of partons could largely grow in relativistic heavy ions and thus affect parton distribution. It depends on the Bjorken scaling x and on the scale of parton-parton interaction Q^2 and could be expressed by a shadowing factor

$$R_i^A(x, Q^2) = \frac{f_i^A(x, Q^2)}{f_i^{nucleon}(x, Q^2)} \quad (18)$$

where A is the number of nucleons in the colliding nucleus, f_i^A is the bound nucleon PDF for parton flavour i and $f_i^{nucleon}$ is free nucleon PDF. Values of shadowing factor for different Bjorken x are in the Figure 21.

- Parton saturation at small x - It is described using Colour Glass Condensate. At smaller x nucleon appears denser and at certain point gluons begin to recombine.
- Multiple scattering of partons - It occurs in the nucleus before and/or after the hard scattering. This leads to parton energy loss and broadening of the transverse momenta, which is called the Cronin effect.
- Final-state inelastic interactions - It is aswell called nuclear absorption of quark-antiquark bound state when passing through the nucleus. The important parameter during this process is the absorption cross section.
- Possible heavy quarkonia dissociation by so called comovers - It is still questionable if medium with some collectivity could be produced in p-A collisions.

3 Results and conclusions

In the Figure 22 can be seen nuclear modification factor of heavy flavour decay leptons from RHIC in d-Au collision. The results at forward and backward rapidity are similar to peripheral collisions, but there is an evidence of deviation for the most central rapidity. At forward rapidity data are described by the model considering nPDFs, k_T broadening and CNM energy loss. Data for backward rapidity can not be described using only nPDFs.

In the Figure 23 are results from ALICE at $\sqrt{s_{NN}} = 5,02$ TeV. There are shown the nuclear modification factors R_{pPb} of prompt D^0 , D^0 and D^{*+} mesons in the left panel and their average, along with the R_{pPb} of D_s^+ mesons, in the right panel. The R_{pPb} is compatible with unity over the p_T interval covered by the measurements and it is also compatible for non-strange and strange D mesons.

Heavy flavour is not only great tool for study of QGP but serves for investigating different CNM effects aswell. These effects are studied at LHC and RHIC. Main problem of the results is low statistics. There is needed more measurements and more precise to correctly quantify the data in the results. There is suppression for forward rapidities in the most central region as seen in results from measurements of the nuclear modification factor of heavy flavour leptons in d-Au collisions at RHIC. For backward rapidity in the most central collisions, nuclear modification

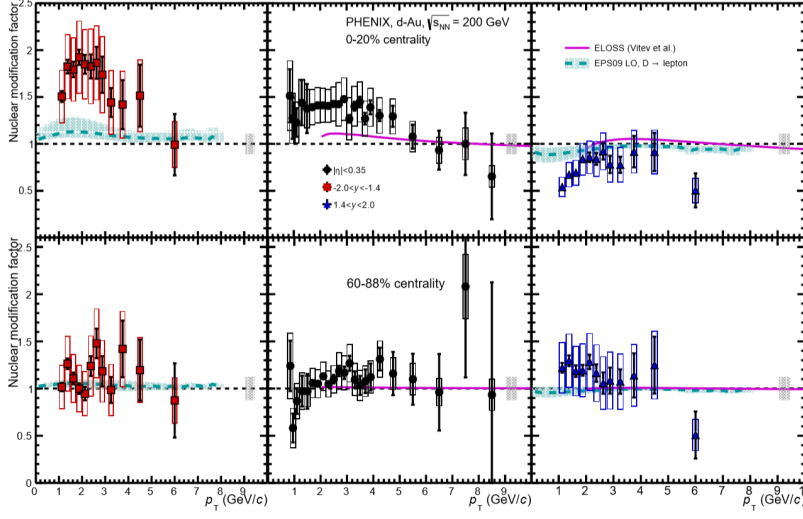


Figure 22: Nuclear modification factor of heavy flavour decay leptons in d-Au collision at $\sqrt{s_{NN}} = 200$ GeV as a function of transverse momentum in the 0 - 20 % and 60 - 88 % centrality classes as measured with PHENIX detector. A PYTHIA calculation considering EPS09 LO is also shown. Taken from [1]

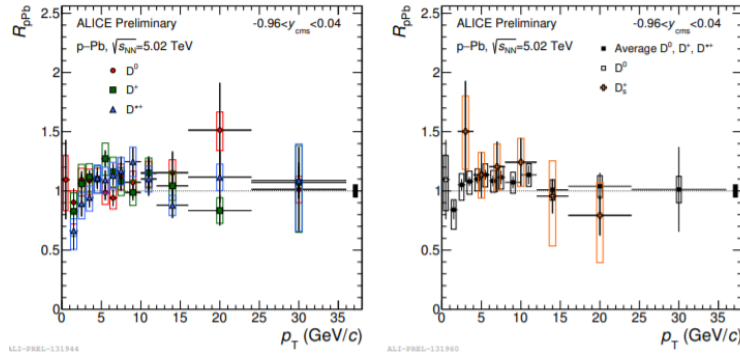


Figure 23: Nuclear modification factor R_{pPb} of prompt D mesons in p-Pb collisions at $\sqrt{s_{NN}} = 5.02$ TeV. Left: R_{pPb} of D^0 , D^+ and D^{*+} mesons. Right: average R_{pPb} of the three non-strange D-meson species and R_{pPb} of D_s^+ mesons. The vertical error bars and the empty boxes represent the statistical and systematic uncertainties, respectively. The black-filled box at $R_{pPb} = 1$ represents the normalisation uncertainty. Taken from [4]

factor is larger than unity. Nuclear modification factor is consistent with unity in the mid-rapidity region and in full transverse momentum range according to results from ALICE at LHC from p-Pb collisions.

References

- [1] A. Andronic, et al. Heavy-flavour and quarkonium production in the LHC era: from proton-proton to heavy-ion collisions. In *arXiv:1506.03981 [nucl-ex]*, 2015.
- [2] X. Luo. Exploring the QCD Phase Structure with Beam Energy Scan in Heavy-ion Collisions. In *arXiv:1512.09215 [nucl-ex]*, 2015.
- [3] K. J. Eskola, H. Paukkunen, C. A. Salgado EPS09: A New Generation of NLO and LO Nuclear Parton Distribution Functions. In *arXiv:0902.4154 [hep-ph]*, 2009.
- [4] ALICE Collaboration Measurement of D^0 , D^+ , D^{*+} and D_s^+ production in Pb-Pb collisions $\sqrt{s_{NN}} = 5.02$ TeV In *arXiv:1804.09083 [nucl-ex]*, 2019.

MUON FORWARD TRACKER FOR THE ALICE UPGRADE

Diana M. Krupova

1 Introduction

The Large Hadron Collider at CERN is the largest and the most powerful particle accelerator ever built for high energy physics. The highest center-of-mass energies reached in the collisions are 13 TeV (proton-proton) and 5.5 TeV (Pb-Pb) [1]. ALICE is one of the four main experiments at the LHC and its main purpose is to study the hot and dense matter created in heavy ion collisions.

The Muon Forward Tracker (MFT) is a part of the ALICE upgrade during the long shutdown 2 in 2019-2021. The MFT was proposed to be added to the ALICE detector system to add vertexing capabilities to the current Muon Spectrometer, as the position of the MFT inside ALICE will be between the interaction point and the hadron absorber.

One of the main physics goals is the separation of charm and beauty hadron production [3]. Thanks to the MFT, it will be possible, for example, to distinguish between prompt and displaced J/ψ production.

2 Detector design

The MFT is a pixel semiconductor detector, using ALPIDE silicon chips [4], that have been developed for both the Inner Tracking System (ITS) and the MFT. The silicon sensors consist of 512×1024 pixels with a total active area of $30 \times 15\text{mm}^2$, they are designed to be back-biased in order to increase the charge collection and the radiation hardness. The silicon pixel sensors are integrated on mechanical ladder structures. A ladder consists mainly of the flexible printed circuit with 2 to 5 pixel sensors laser-soldered to it. The ladders are assembled on the five disks that constitute the MFT (divided into top and bottom half, see Figure 24).

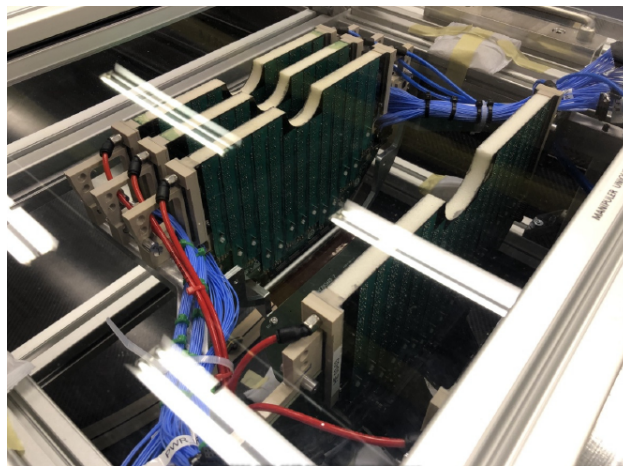


Figure 24: Assembled bottom half-cone of the detector.

3 Qualification tests

All the ALPIDE chips on the ladder need to be characterized to evaluate their behaviour [2]. To perform the qualification tests, each ladder is connected to the test bench and MOSAIC board that performs readout and configuration.

The qualification procedure consists of several different tests:

- readout test - to eliminate any communication errors,
- FIFO (first in, first out) scan - to test the organizing and processing of data,
- digital scan - to verify the correct behaviour of the digital part of sensor internal circuit,
- threshold scan, which tests also the analog part of the chip,
- noise occupancy scan - to measure fake-hit rate, a probability of registering a hit not due to the passage of a particle,
- eye measurement - to analyze digital waveforms.

The non-conformal ladders, where at least one of the tests fails, need an intervention before further use. We divide the conformal ladders - where all the tests are performed without any issues - into three categories: gold, silver, bronze. This result determines their position on the disk.

4 Conclusions

With the MFT, ALICE will be able to further explore important phenomena in particle physics, such as J/ψ production. The detector uses silicon chip sensors to measure particles in the forward direction. The sensors need to be tested and qualified to determine the characteristics of the detector performance later on.

References

- [1] ALICE Collaboration. Performance of the ALICE Experiment at the CERN LHC. <http://inspirehep.net/record/1281831>. 2014.
- [2] ALICE Collaboration. Technical Design Report for the Muon Forward Tracker. <https://cds.cern.ch/record/1981898>. 2015.
- [3] ALICE Collaboration. Addendum of the Letter of Intent for the Upgrade of the ALICE Experiment: The Muon Forward Tracker. CERN-LHCC-2013-014 (2013).
- [4] G. Aglieri *et al.* Monolithic active pixel sensor development for the upgrade of the ALICE inner tracking system. JINST8, C12041 (2013).

STUDY OF JET SUBSTRUCTURE IN AU+AU COLLISIONS WITH THE STAR EXPERIMENT

Monika Robotková

1 Introduction

Jets, collimated sprays of hadrons, are a good probe to study a hot dense matter of partons called quark-gluon plasma (QGP). During the propagation of the jets through the QGP, jet quenching can occur. This phenomenon is caused by the interaction between hard partons and coloured medium, which leads to parton energy loss.

Experimentally we can investigate jet quenching through the inclusive properties of the jets or modification of the jet substructure. This study focuses on the jet substructure, namely the observable *jet splitting function* z_g .

2 Jet substructure

The study of jet substructure can provide new insight into medium induced effects during the parton shower evolution in the QGP. One of the many observables that can be used is the jet splitting function z_g . This observable characterizes the parton splitting and emerges as a "by-product" of the SoftDrop [1] grooming technique.

The SoftDrop technique uses clustering history to remove soft wide-angle radiation from a sequentially clustered jet. First, we take the jet defined with the anti- k_t algorithm. This jet is reclustered using the C/A algorithm and we get two subjets from the original jet by undoing the last stage of C/A clustering. We look if these subjets pass the Soft Drop condition

$$\frac{\min(p_{T,1}, p_{T,2})}{p_{T,1} + p_{T,2}} > z_{cut} \left(\frac{\Delta R_{12}}{R_0} \right)^\beta, \quad (19)$$

where z_{cut} and β are parameters, $p_{T,i}$ are transverse momenta of the subjets, ΔR_{12} is their distance and R_0 the jet radius. If this condition is met, then the original jet is the final soft-dropped jet. Otherwise, the subjet with the higher p_T is taken as the new original jet and the process is repeated.

The jet splitting function z_g is then defined as

$$z_g \equiv \frac{\min(p_{T,1}, p_{T,2})}{p_{T,1} + p_{T,2}}. \quad (20)$$

An example of the z_g measurement in Au+Au collisions with energy $\sqrt{s_{NN}} = 200$ GeV is shown in Figure 36.

3 Background subtraction

In heavy ion collisions, jets receive a large contribution from a soft background. There are several methods used to subtract the background from the jets and two of them briefly discussed below.

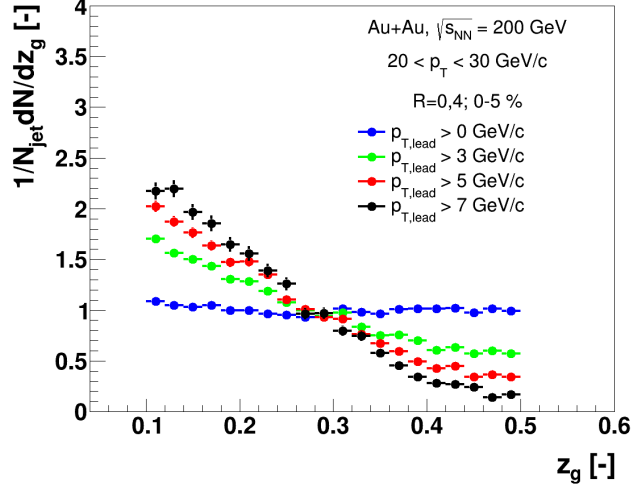


Figure 25: The uncorrected z_g distribution in Au+Au data at $\sqrt{s_{NN}} = 200$ GeV for charged jets.

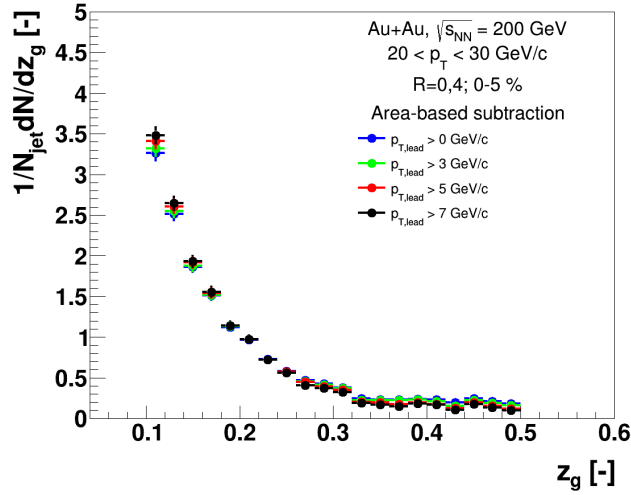


Figure 26: z_g distribution in Au+Au data at $\sqrt{s_{NN}} = 200$ GeV for charged jets corrected with area-based method.

3.1 Area-based subtraction

This method is based on subtraction of median jet energy density ρ multiplied by the jet area A from the reconstructed jet transverse momentum $p_{T,jet}^{raw,ch}$

$$p_{T,jet}^{corr,ch} = p_{T,jet}^{raw,ch} - A \times \rho. \quad (21)$$

The median jet energy density is calculated as $\rho = \text{med} \left\{ \frac{p_{T,jet}^i}{A_i} \right\}$, where the index i goes over all jets in a given event. An example of this method is displayed in Figure 37.

3.2 Soft Killer

The Soft Killer method [2] consists of subtraction of the particles with low p_T . First, the rapidity-azimuth plane is divided into square patches of size $a \times a$. Then we estimate the median energy density as $\rho = \text{med} \left\{ \frac{p_T^i}{A_i} \right\}$, where i goes over all patches. For each patch i , we determine the transverse momentum $p_{T,i}^{max}$ of the hardest particle in that patch. Then we can calculate "cut-off" p_T^{cut} as

$$p_T^{cut} = \text{med} \{ p_{T,i}^{max} \}. \quad (22)$$

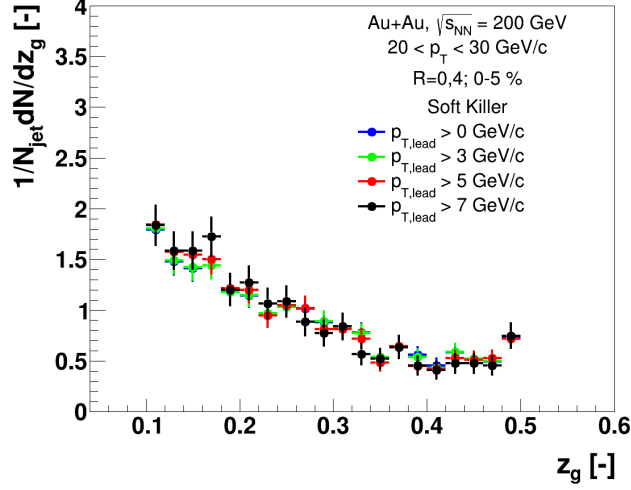


Figure 27: z_g distribution in Au+Au data at $\sqrt{s_{NN}} = 200$ GeV for charged jets corrected with Soft Killer method.

The particles with $p_T < p_T^{cut}$ are subtracted from the event, so half patches remain empty. An example of this method is shown in Figure 38.

4 Discussion

The first look at the measurements of the jet splitting function z_g in Au+Au collisions at $\sqrt{s_{NN}} = 200$ GeV was presented. We applied several background subtraction methods, such as area-based subtraction or Soft Killer. The next step in this analysis will be to apply other background subtraction methods and compare their effectiveness by creating response matrices.

References

- [1] Andrew J. Larkoski, Simone Marzani, Gregory Soyez and Jesse Thaler. Soft Drop. *arXiv preprint arXiv:1402.2657*, 2014.
- [2] Matteo Cacciari, Gavin P. Salam, Gregory Soyez. SoftKiller, a particle-level pileup removal method. *arXiv preprint arXiv: 1407.0408v2*, 2016.

EUROPEAN STRATEGY OF PARTICLE PHYSICS 2020

Katarína Křížková Gajdošová

1 Introduction

In 2006, the CERN Council launched the European Strategy of Particle Physics, which is a document that is supposed to set the road of European particle physics in the future, in coordination with projects from around the world, such that particle physics benefits the most. In 2013, an update to the Strategy was published, and now, in the year 2020, we are about to define a new Strategy, which is particularly important because it should promote one of the scenarios of large future collider projects. The Physics Preparatory Group (PPG) prepares the scientific contribution from the community to the European Strategy Group (ESG), which drafts a proposal of the European Strategy for Particle Physics to the CERN Council to make a final decision.

2 The timeline of the Strategy

The first call for scientific input was in February 2018. It took several months until the PPG and ESG were formed, and inputs from all the participating countries were collected. These were then discussed during an Open Symposium in May 2019 in Granada, Spain. The output of this symposium was summarised in a Physics Briefing Book [1], after which the community was allowed to review it and comment on it. A drafting session was organised in January 2020 in Bad Honnef, Germany, to start the process of creating the Strategy document, which is planned to be submitted to the CERN Council in March 2020. Council's approval is supposed to happen in May 2020.

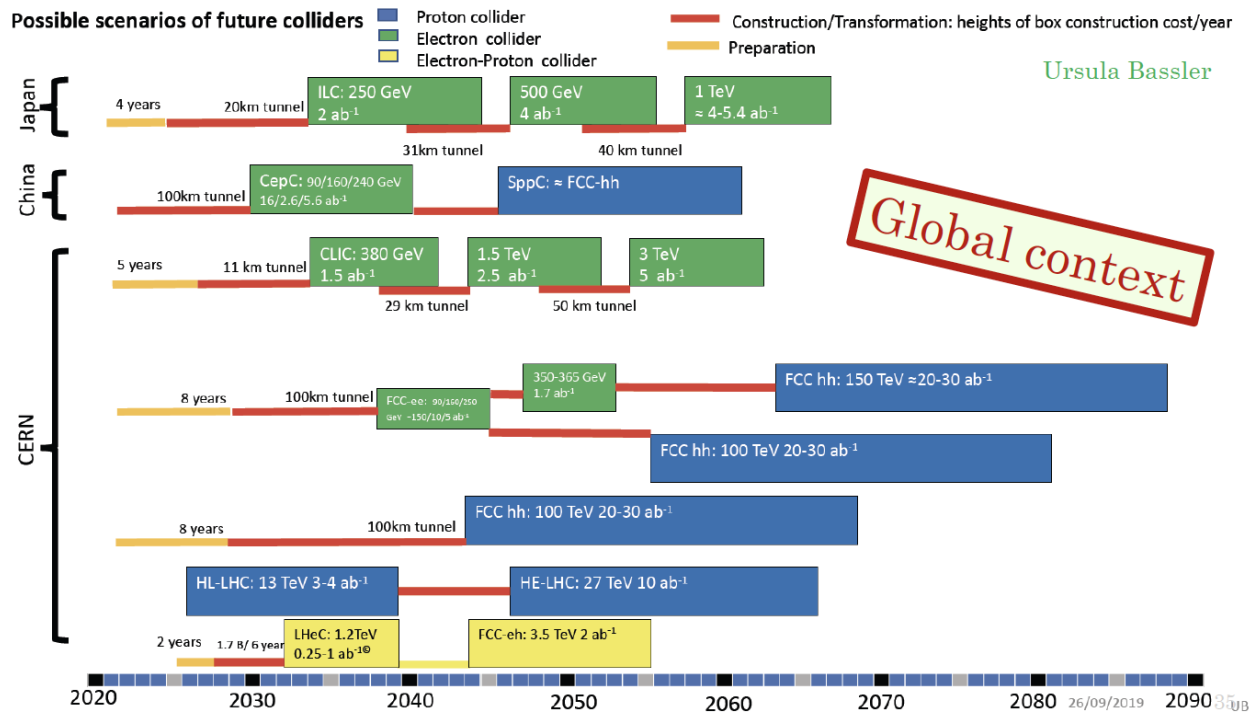
During the time dedicated to the review of the Physics Briefing Book, ECFA (European Committee for Future Accelerators) invited Early-Career Researchers (ECR) to contribute to the discussion, since this year's Strategy will have a large impact on the far future of the field, affecting mostly the career of the ECR. The ECR's met at CERN on 15th November with the aim to discuss the contents of the Briefing Book, and identify points of great importance to the ECR community. The outcome of this discussion is briefly summarised in Section 3.

2.1 Proposals for possible future accelerators

There are several proposals of future accelerators supposed to be built around the world (at CERN, Japan or China). All of them have clear motivation for a specific part of physics to be studied. A schematic diagram of the accelerators with the estimated time of preparation and realisation is shown in Fig. 28. The Briefing Book outlines 5 possible scenarios of these future accelerators to lead the discussion, which are shown in Table 29. The final decision on whether an accelerator will be built at CERN, and if yes, what kind, depends on the status of the projects in other countries around the world.

3 Early-Career Researchers debate

Around 180 ECR met at CERN on 15th November 2019 to discuss the Physics Briefing Book and possible scenarios of the future of the field once the Strategy is defined. The outcome of the discussion was formulated in a short Report [3] sent to the ECFA chair, who promised to consider our comments, suggestions and concerns, and possibly raise them during the Drafting Session of the Strategy in January. This is the first time when ECR's were invited to participate



	2020-2040	2040-2060	2060-2080
		1st gen technology	2nd gen technology
CLIC-all	HL-LHC	CLIC380-1500	CLIC3000 / other tech
CLIC-FCC	HL-LHC	CLIC380	FCC-h/e/A (Adv HF magnets) / other tech
FCC-all	HL-LHC	FCC-ee (90-365)	FCC-h/e/A (Adv HF magnets) / other tech
LE-to-HE-FCC-h/e/A	HL-LHC	LE-FCC-h/e/A (low-field magnets)	FCC-h/e/A (Adv HF magnets) / other tech
LHeC-FCC-h/e/A	HL-LHC + LHeC	LHeC	FCC-h/e/A (Adv HF magnets) / other tech

Figure 29: Possible scenarios of future accelerators built around the world. Taken from [2].

in such a discussion. We strongly encouraged such meetings in the future, and possibly forming a permanent ECR committee as part of ECFA.

The discussion started offline around two weeks before the meeting at CERN, and was split in the following topics:

- Electroweak and Strong Physics
- BSM, Dark Matter and Dark Sector
- Neutrino, Flavour and Cosmic Messenger Physics
- Accelerator and Detector R&D
- Computing and Software
- Environment and Sustainability

However, after the meeting, it was realised that another important topic should be included and considered when forming the Strategy document: Human and sociological factors. The ECR felt that the field needs a substantial change in the way research positions are being held. Based on a survey filled by a large fraction of the ECR, majority of them experience work related stress mainly because working extra hours is necessary to secure their academic

career, and because it is very hard to maintain a healthy work-life balance. It was suggested in the document to change the project-oriented short-term funding of research positions into more base-funding projects, enabling a larger fraction of permanent positions. Furthermore, measures should be taken in order to decrease the importance of attendance at conferences/workshops, such that researchers can afford to have children while not damaging their scientific career.

These are just few examples of the many comments and suggestions listed in the ECR Report. We hope that the next European Strategy of Particle Physics will be the starting point for inclusion of human and sociological factors into the important discussions about the future of our field.

4 Summary

In summary, the European Strategy for Particle Physics was introduced, and the outline of the next one, defined in May 2020, was presented. In addition, results of the debate of Early-Career Researchers about the Strategy were shown.

References

- [1] European Strategy for Particle Physics Preparatory Group, Physics Briefing Book, arXiv: 1910.11775.
- [2] J. d'Hondt (chair of ECFA), presentation at JENAS 2019, <https://jenas-2019.lal.in2p3.fr>
- [3] N. Andari et al., Report on the ECFA Early-Career Researchers Debate on the 2020 European Strategy Update for Particle Physics, arXiv: 2002.02837.

STAR ZERO DEGREE CALORIMETER

Jan Vaněk

1 Introduction

The STAR detector is a very complex machine which consists of many sub-systems. The best known ones are those placed in the central barrel, such as the Time Projection Chamber (TPC) or the Heavy Flavor Tracker, which are used for tracking and particle identification. Equally important is one of the less known detectors – the Zero Degree Calorimeter (ZDC) which is important for monitoring of the RHIC beam quality, it is a critical part of STAR trigger system and it helps with heavy-ion collision centrality determination. In these proceedings, a brief description of the ZDC design and experimental operations is provided.

2 Design

The ZDC consists of two modules which are located 18 m from the center of the STAR detector and are placed between the RHIC beam pipes, as shown in Fig. 30. This placement was chosen as the ZDC is designed to detect spectator neutrons from ultra-relativistic heavy-ion collisions. Such neutrons continue on a straight line from the Intersection Point (IP) after a A+A collision, any protons or nucleus fragment are deflected by a RHIC steering dipole magnet away from the ZDC. The combination of the distance from the IP, placement between the beam pipes and physical dimensions of the ZDC ensures that majority of measurable signal is from the spectator neutrons.

Each of the two ZDC modules (east and west module) consist of three identical towers. A schematic cross-section of one of the towers is shown in Fig. 31. The sensitive part is a sandwich of 5 mm thick tungsten plates and PMMA fibers. When a ultra-relativistic neutron hits the plates, it generates a shower of charged particles which then pass through the optical fibers at velocity higher than that of light (in the PMMA). As a result, Cherenkov light is emitted and subsequently transported through the fibers into a photomultiplier. The plates and fibers are tilted by 45° with respect to the beam axis in order to improve efficiency of collection of the Cherenkov light.

The ZDC is designed to detect primarily neutrons at RHIC top energy, i.e. 100 GeV. In that case, the gain of individual ZDC towers should be in ratio of 6:3:1 where the highest gain corresponds to the tower closest to the IP. Also the total gain should be the same for both, east and west, ZDC module. The gains can be tuned by adjusting the high voltage (HV) applied to the individual photomultipliers. The procedure for tuning the ZDC HV is briefly described in the following section.

3 Experimental operation

At the beginning of each data taking period, the ZDC needs to be checked and calibrated to meet the gain condition mentioned above. The basic check is just to verify that all HV and the readout electronics work properly which is rather straightforward. More interesting is the calibration procedure. First, a dedicated data sample is collected which is then further analyzed. The ADC distributions for each individual tower are fitted in order to locate and integrate the single neutron peak. If the HV applied to the photomultipliers is correct, the ratio of the integrals should be 6:3:1 and the integral for sum for east and west ZDC should be the same (magnitude of the signal in east ZDC module has to be the same as in the west ZDC module). In case one of the conditions is not met, the HV are changed accordingly

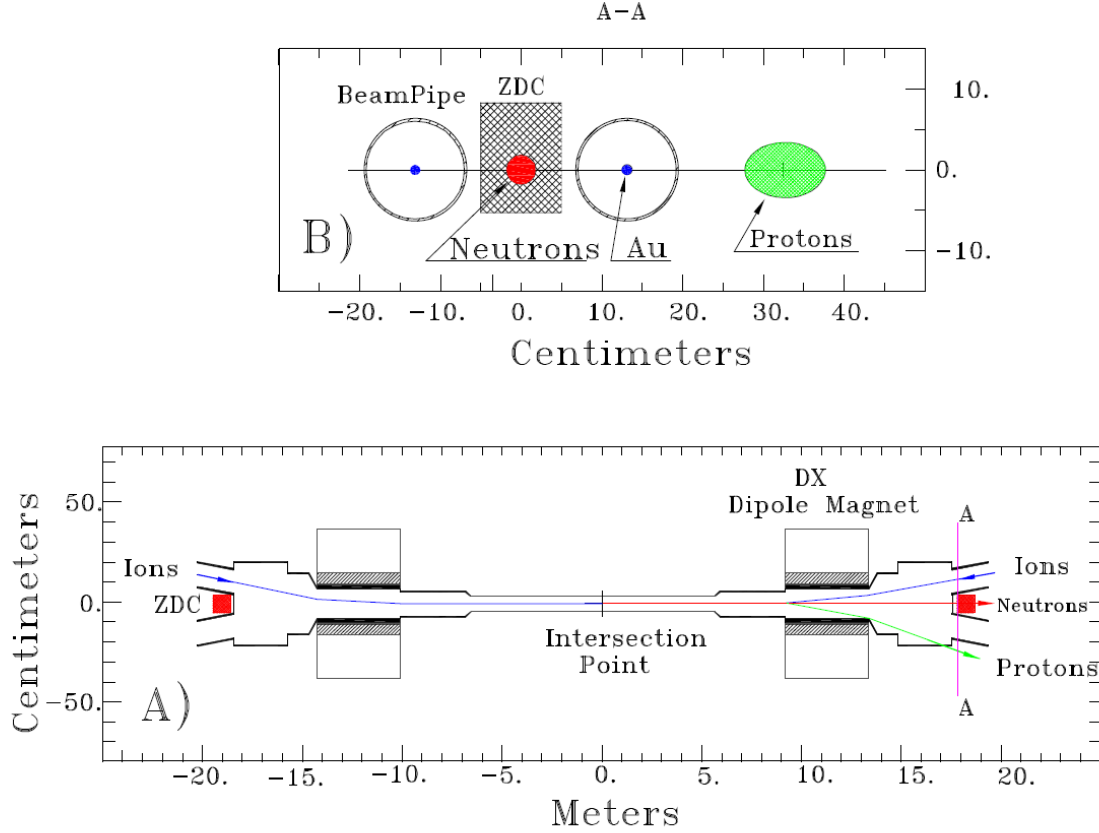


Figure 30: Schematic view of ZDC location with respect to the intersection point (center of the STAR detector) and its placement between RHIC beam pipes. Taken from Ref. [1].

and the whole process is repeated. An example of the ADC distributions with clearly visible single neutron peak are shown in Fig. 32.

Once the ZDC is calibrated, it can be used during data taking and for experimental analyses. During the data taking period, the ZDC has two main functions. The first one is that it is used for monitoring of the beam in RHIC. As both beams are steered into STAR IP, the ZDC rates start to rise. When the rate achieves desired value, the Collider Accelerator Department adjusts the beam properties to preserve the luminosity for as long as technically possible. Once the ZDC rate drops below certain value, the beams are dumped and then the RHIC is filled with new ones.

In addition, the ZDC is part of the STAR trigger system. Coincidence of signal in east and west ZDC module, within preset time window, gives signal to the trigger electronic. Then, multiple properties of such event are checked, usually based on signal from fast detectors, such as the Time Of Flight. If all criteria are met, the information from central barrel detectors is stored. Another two detectors can be used the same way as the ZDC for triggering. They are the Vertex Position Detector and the Beam-Beam Counter.

The ZDC is also very important for many data analyses. One of the most important is the heavy-ion collision centrality determination. One way is to measure number of spectator neutrons in a given collision. The less spectator neutrons measured, the more central a collision is. This method is not used at STAR tho. The centrality at STAR is determined from charged particle multiplicity in the TPC. The shape of the event multiplicity distribution depends on luminosity, as the TPC tracking efficiency also depend on it. The information from ZDC is therefore vital for centrality determination at STAR.

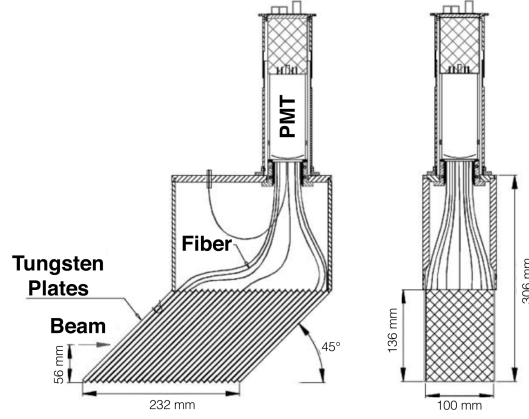


Figure 31: Schematic cross-section of one ZDC tower. Taken from Ref. [1].

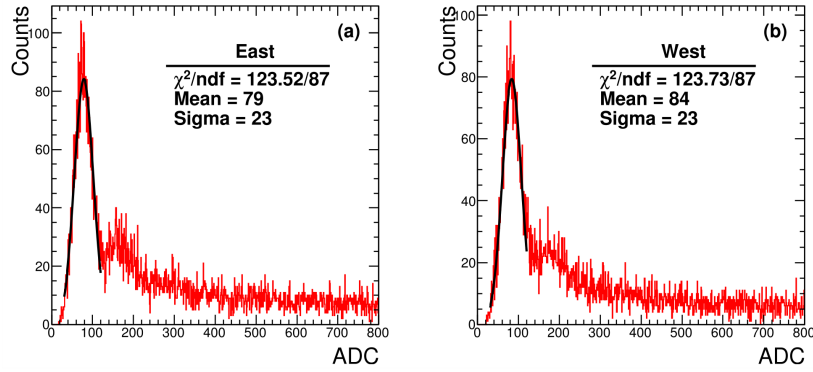


Figure 32: Single neutron peak measured by east and west STAR ZDC in data from Run14. Taken from Ref. [2].

4 Summary

The STAR ZDC is a vital sub-system of the STAR detector. It is used during the data taking period for monitoring of the RHIC beam quality and as a trigger detector for STAR. It also plays very important role for analyses of ultra-relativistic heavy-ion collisions because it is used as a part of collision centrality determination.

References

- [1] Clemens Adler *et al.* The RHIC zero degree calorimeter. In *Nuclear Instruments and Methods A470*, pages 488–499. 2001.
- [2] Yi-Fei Xu, *et al.* Physics performance of the STAR zero-degree calorimeter at relativistic heavy ion collider. In *Nuclear Science and Techniques* 27, 126. 2016.

JET EVOLUTION

Josef Bobek

1 Introduction

We can divide the definition of the jet into two categories. First is the detector level and the second one is a parton level. The first one, how we define jet from the data using jet reconstruction algorithms, I covered last year and this year of EJČF workshop I decided to cover the second one. That includes how we can factorize inclusive jet cross-section for proton-proton collisions and then modify it with weight function to get an inclusive jet cross-section for heavy-ion collisions.

2 Jet evolution

Jet is a hard probe. This means it is caused by the hard scattering of two partons (real and virtual quarks and gluons) leading to creating highly penetrating observable particles. In this case, it is high transverse momentum p_T that causes high penetration. After the collision, parton with high p_T can radiate gluons, gluons can decay into $q\bar{q}$ pair and with asymptotic freedom of $q\bar{q}$ pairs more pairs can be created. This continues, cascade then hadronize and we record it in the detector.

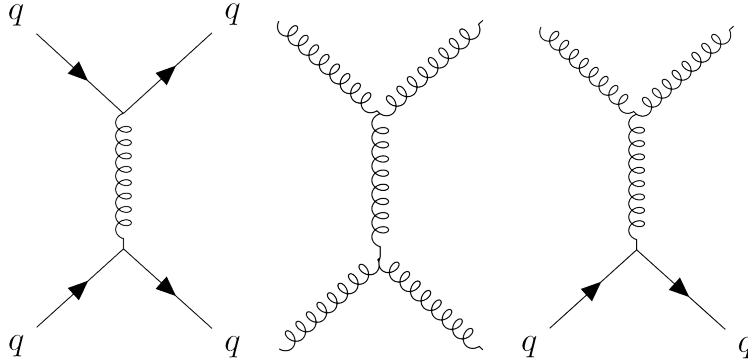


Figure 33: Feynman diagrams for hard scattering of two partons.

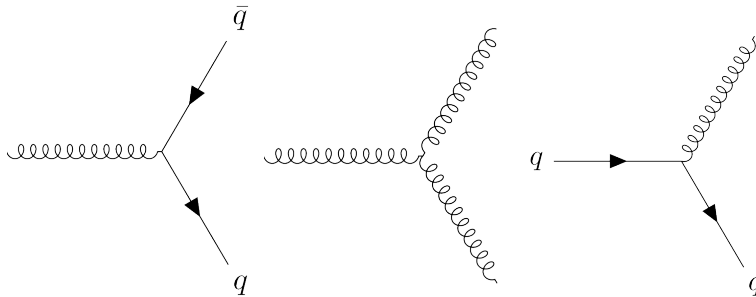


Figure 34: Feynman diagrams for gluon decay, gluon radiates gluon and quark radiates gluon.

2.1 Inclusive jet cross section for proton-proton collisions

First, let's factorize inclusive jet cross-section like

$$\frac{d\sigma^{p+p \rightarrow jet+X}}{dp_T d\eta} = \sum_{ab} f_{a/p} \star f_{b/p} \star \mathcal{H}_{ab}^{jet}, \quad (23)$$

where $f_{i/p}(x_i)$ is the parton distribution function (PDF) for flavor i , the four-momentum p as a function of the fraction of total momentum x_i . The operator \star denotes the convolution with respect to the fractions of total momentum. \mathcal{H}_{ab}^{jet} are hard parts of the scattering of partons a and b that produced jet and finally, p_T is the transverse momentum and η is pseudorapidity.

2.1.1 Parton distribution functions

Parton distribution functions are probability distribution functions of finding parton with a fraction of total momentum x in a hadron with an energy scale Q . The fraction of total momentum is defined as $x = \frac{p_a}{p_N}$, where p_a is the momentum of parton with flavor a and p_N is the total momentum of nucleon N .

PDFs meet DGLAP (Dokshitzer-Gribov-Lipatov-Altarelli-Parisi) evolution equation

$$Q^2 \frac{\partial f_{a/p}}{\partial Q^2} = \sum_b \int_x^1 dy \frac{1}{y} \frac{\alpha_s}{2\pi} P_{ab}(y) f_{b/p}\left(\frac{x}{y}\right), \quad (24)$$

where $P_{ab}(y)$ is the probability of parton with flavor b and with a fraction of total momentum y will decay on parton a . α_s is a constant of strong interaction. From this equation and some measurements we can then obtain the whole set of PDF.

2.1.2 Hard parts

Hard parts are broken down as

$$\mathcal{H}_{ab}^{jet} = \sum_c \hat{\sigma}_{a+b \rightarrow c} \star J_c + \hat{\sigma}_{ab}^{jet}, \quad (25)$$

where $\hat{\sigma}_{a+b \rightarrow c}(z, Q)$ is a jet independent hard part for producing parton with flavor c and fraction of total transverse momentum $z = \frac{p_{Tc}}{p_T}$, $J_c(z, p_T R, Q)$ is a jet dependent jet function for producing a jet with a jet radius R from parton with flavor c . The last part $\hat{\sigma}_{ab}^{jet}$ is suppressed by R , therefore can be neglected.

If we would like to come to the jet independent cross-section we can overpass from jet function to the fragmentation function D_c^h . Leading to the jet cross-section

$$\frac{d\sigma^{p+p \rightarrow jet+X}}{dp_T d\eta} = \sum_{abc} f_{a/p} \star f_{b/p} \star \sigma_{a+b \rightarrow c}(z, Q) \star D_c^h(z, Q) \quad (26)$$

We can do this because of suppression by high p_T .

D_c^h and J_c functions also meet DGLAP evolution equation

$$Q \frac{dJ_c(z, p_T R, Q)}{dQ} = \sum_d P_{dc}(z) \star J_d(z, p_T R, Q). \quad (27)$$

The benefit of working with jet function J_c is that we can calculate it from pQCD. D_c^h is non-perturbative QCD, but on the other hand, we have to keep in mind the fragmentation function D_c^h is not dependent on final jet. We can obtain D_c^h from $p + p$ collisions data.

2.2 Inclusive jet cross section for heavy-ion collisions

First, we can go from PDFs to nuclear PDFs, but their impact on calculations is small.

The biggest impact has jet function $J_c(z, p_T R, Q)$ from multiple scattering in medium. That being said, we would like to modify this function into the modified jet function $J_c^{med}(z, p_T R, Q)$. As I mentioned in the introduction we use weight function and also we will go from the energy scale Q to the modified energy scale $Q_J = QR$. We get modified jet function

$$J_c^{med}(z, p_T R, Q_J) = W_c(z) \star J_c(z, p_T R, QR), \quad (28)$$

where weight function

$$W_c(z) = \epsilon_c \delta(1 - z) + N_c z^{\alpha_c} (1 - z)^{\beta_c} \quad (29)$$

is in this form, so it can meet certain limits, for example for very peripheral collisions, where $W_c \rightarrow \delta(1 - z)$. The parameters are determined by Monte Carlo simulations.

2.3 Summary

Finally, we get inclusive jet cross-section for heavy-ion collisions

$$\frac{d\sigma^{A+A \rightarrow jet+X}}{dp_T d\eta} = \sum_{abc} f_{a/p} \star f_{b/p} \star \sigma_{a+b \rightarrow c}(z, Q) \star W_c(z) \star J_c(z, p_T R, Q_J). \quad (30)$$

We can put this cross-section into the nuclear modification factor

$$R_{AA}^{jet} = \frac{d\sigma^{A+A \rightarrow jet+X}}{\langle T_{AA} \rangle d\sigma^{p+p \rightarrow jet+X}}, \quad (31)$$

where $\langle T_{AA} \rangle$ is average nuclear overlap function for certain centrality. Finally, we can compare this factorization with measurements.

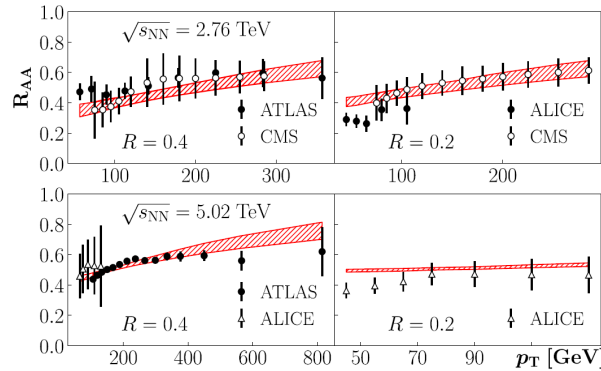


Figure 35: The nuclear modification factor for inclusive jets (0% – 10% centrality) [1]

References

- [1] Jian-Wei Qiu, Felix Ringer, Nobuo Sato, Pia Zurita Factorization of jet cross sections in heavy-ion collisions *arXiv preprint arXiv:1903.01993*, 2019.
- [2] Ringaile Placakyte Parton Distribution Functions *arXiv preprint arXiv:1111.5452*, 2019.

ANISOTROPIC FLOW MEASUREMENTS WITH THE ALICE EXPERIMENT

Daniel Mihatsch

1 Introduction

The aim of my bachelor thesis is studying ultrarelativistic heavy-ion collisions, in which the quark-gluon plasma (QGP) is produced. The QGP is state of matter, in which quarks and gluons, the elementary constituents of nucleons, are deconfined. It is predicted, that whole universe was in this state in early stages of its evolution. So through studying heavy-ion collisions we create our own "little bangs", which allows us to study fundamental properties of all matter around us. One of the measurement methods, which can provide us some information about QGP, is anisotropic flow measurement.

Let's start with brief introduction to QGP evolution, which starts with a collision of two relativistically contracted nuclei (in most cases lead or gold), which interact primarily through gluons. The energy of collision is transferred into newly created medium, which is not in equilibrium, in stage called pre-equilibrium. The medium gradually thermalizes and expands at the same time, firstly in longitudinal and then in transverse direction. After reaching equilibrium, the created matter can be described hydrodynamically and that's why we measure some collective phenomena as flow. During whole process the medium is cooling down and when its temperature decreases below approximately 170 MeV, it passes to next stage of its evolution via phase transition, in which quarks and gluons are merged back into hadrons according to Cooper-Frye mechanism. The produced particles still can interact in inelastic collisions until chemical freeze-out and in elastic collisions until kinetic freeze-out.

The collisions are classified according to their centrality parameterized by impact parameter b , which is basically distance between centers of nuclei. This classification is very important, because central and peripheral collisions are completely different and we cannot compare them with each other. The impact parameter itself cannot be directly observed, so we have to look for other possibilities how to determine centrality. In fact, we usually measure number of hadrons produced in single collision and then we get number of participated nucleons N_{part} (nucleons which undertook at least one elementary collision) and number of binary collisions N_{bin} (overall number of elementary collisions) using the Glauber model [2].

The ALICE is an experiment composed of several different types of detectors located on Large Hadron Collider in the CERN site near Geneva. The experiment is focused on research of QGP and its properties.

2 Anisotropic flow

The initial energy density fluctuations of created matter in transverse plane are converted via hydrodynamics into anisotropic flow of produced particles, which can be described by Fourier series of differential of produced particles N

$$E \frac{d^3 N}{d^3 \mathbf{p}} = \frac{1}{2\pi} \frac{d^2 N}{p_T dp_T dy} \left(1 + 2 \sum_{n=1}^{\infty} v_n \cos [n(\varphi - \Psi_n)] \right), \quad (32)$$

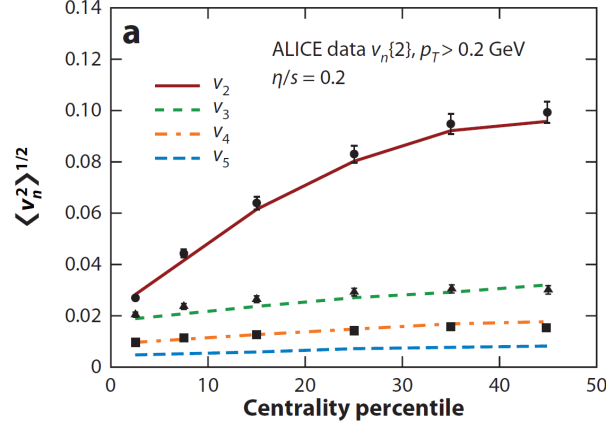


Figure 36: Elliptic flow dependence on centrality and viscosity (η/s) determination based on ALICE data according to [1].

where E is energy of particle, p momentum, p_T transverse momentum, φ azimuthal angle in transverse plane, y rapidity and Ψ_n reaction plane angle. The flow is then characterized by Fourier coefficients

$$v_n(p_T, y) = \langle \langle \cos[n(\varphi - \Psi_n)] \rangle \rangle, \quad (33)$$

where $\langle \langle \dots \rangle \rangle$ means average over all particles in an event and over all events. Particular coefficients are known as directed flow for $n = 1$, elliptic flow for $n = 2$, triangular flow for $n = 3$ and so on, but the most important for our measurements is the second order. As long as we cannot measure reaction plane angles directly, the multiparticle correlations are used

$$v_n^2 = \langle \langle \cos[n(\varphi_1 - \varphi_2)] \rangle \rangle, \quad (34)$$

where φ_1 and φ_2 are angles in transverse plane, in which particular particles were emitted [1].

2.1 Elliptic flow and viscosity

The viscosity is one of the parameters of hydrodynamics used for description of QGP and it can be determined from flow measurements, because it decreases anisotropy of flow in transverse plane. So if we use theoretical hydrodynamic model and fit measured data (v_2), we get viscosity as one of the parameters. This determination is illustrated on Figure 36, which shows elliptic flow dependence on centrality based on ALICE data. The viscosity was determined as $\eta/s = 0.2$, which is very surprising, because it is the lowest viscosity, which has ever been observed. The way, how the value is obtained, still depends on several conditions, for instance what initial conditions are considered or how we model hadronization process. So for exact determination of viscosity, more detailed measurements as dependence of flow on temperature are required.

3 Summary and outlook

Anisotropic flow measurements provide us crucial information about properties of quark-gluon plasma, especially they can be very useful for viscosity determination. Everything so far written in this short introduction to flow measurements is valid for big systems (heavy-ion collisions) and no collective phenomena were expected in small systems (for instance proton-proton collisions). Nevertheless, it turned out, that similar collectivity as in big systems was recently observed also in small systems, which can indicate creation of QGP in these collisions. Short review of this topic will be also part of my bachelor thesis.

References

- [1] Ulrich Heinz and Raimond Snellings. Collective Flow and Viscosity in Relativistic Heavy-Ion Collisions. In *Annu. Rev. Nucl. Part. Sci.* 2013. 63:123–51.
- [2] Raimond Snellings. Elliptic flow: a brief review. In *New J. Phys.* 13 055008, 2011.

PERFORMANCE OF THE UPGRADED ELECTRONICS FOR CHERENKOV AND SCINTILLATOR DETECTORS OF THE PIERRE AUGER OBSERVATORY

Margita Majerčáková

1 Introduction

Cosmic rays are high energy particles that arrive from space outside the Earth atmosphere. They are mostly composed of protons but also from other light nuclei or other particles like electrons, positrons etc. The Pierre Auger Observatory is the largest astroparticle experiment to observe and investigate these particles. Currently, this Observatory is in the process of implementing the upgrade called AugerPrime, which focuses on composition of cosmic rays of ultra high energies. Part of the upgrade is also new electronics, which needs to be tested.

2 AugerPrime

The Auger Prime Observatory is located in Argentina, Mendoza province and it spreads over area of 3000km². Two types of detectors are used, water Cherenkov detectors creating surface array and fluorescence telescopes [2]. Besides these detectors, various improvements and upgrades are implemented here.

AugerPrime is upgrade of the Pierre Auger Observatory currently under deployment. The main part of this upgrade is placement of scintillator detectors on top of each water Cherenkov detector. This combination should improve resolution of muonic and electromagnetic component of cosmic ray and ratio of these components is related to composition of primary cosmic ray [1].

3 New electronics

Electronics used for signal processing of the water Cherenkov detectors needs to be replaced with new version, mainly because of added detectors. This electronics will also have higher sampling frequency and will be faster. This new board is called UUB (Upgraded Unified Board).

The final version of the board is called V3 (third version). First version V1, was produced and then used to determine any flaws. Version V2 was improved too and so the V3 was produced as final version, which is free from defects that V1 and V2 had.

Some characteristics of UUB that are examined are noise and ratio of high gain and low gain channel. These channels amplify signal with different gains, so the range of detected signals can be wider. The ratio should be around 32 for signal from water detector and around 128 for scintillator detector.

3.1 Noise

Noise of the electronics is defined as standard deviation of pedestal. It should be less than 2 ADC counts, so small signals can be detected. Dependence of noise on temperature UUB V1 was measured in laboratory in a temperature chamber. Temperature cycled from -20°C to 70°C . Results are shown in Fig. 37. There can be seen, that noise is approximately 9 ADC counts, which is unsuitable.

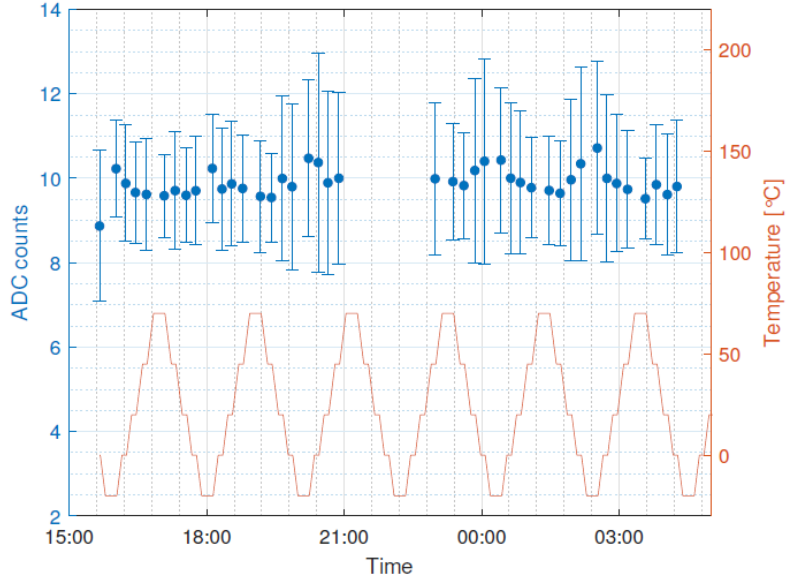


Figure 37: Dependence of noise on temperature, UUB V1.

Noise of UUB V2 was observed from water station in the Observatory, where this version was already implemented. The results for selected months are shown in Fig. 38. Indeed, noise on UUB V2 is significantly smaller than on the previous version and it is around 2 ADC counts.

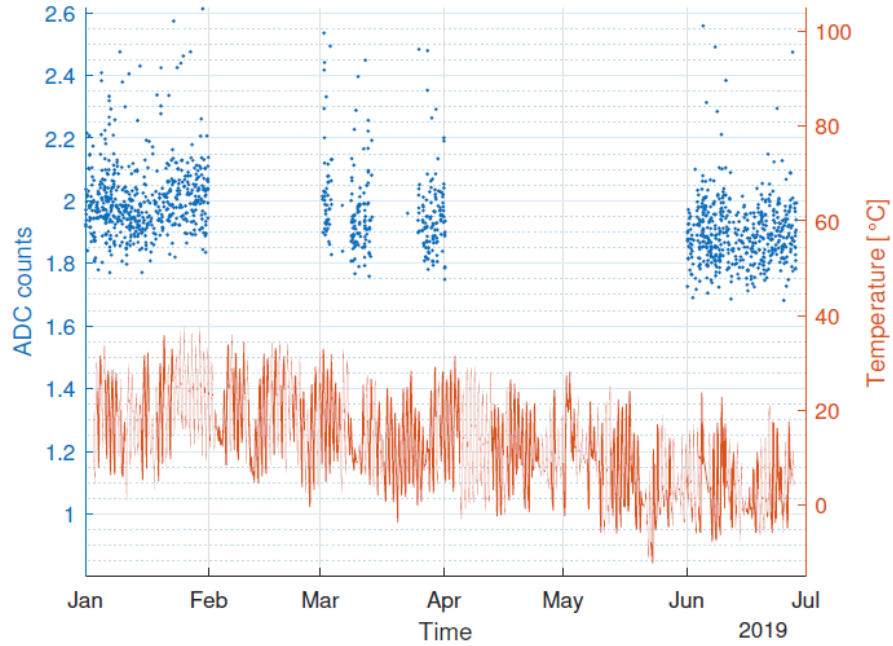


Figure 38: Dependence of noise on temperature, UUB V2.

The second version of UUB has therefore lower noise than the first one. Its temperature dependence is also more constant.

References

- [1] Aab, Alexander, et al. The Pierre Auger Observatory upgrade-preliminary design report. arXiv preprint arXiv:1604.03637 (2016).
- [2] Pierre Auger Collaboration. "The Pierre Auger cosmic ray observatory." Nuclear Instruments and Methods in Physics Research Section A: Accelerators, Spectrometers, Detectors and Associated Equipment 798 (2015): 172-213.

MEASUREMENT OF HBT RADII IN 1.23A GeV Au+Au COLLISIONS FROM URQMD SIMULATIONS

Jakub Štěrba

1 Introduction

Experiment HADES published results of its measurement of two-pion intensity interferometry in central and non-central collisions of Au+Au at 1.23A GeV. Correlations of these pions were fitted by 3-dimensional Gaussian which results were used to produce HBT radii in several bins for mean transversal momentum of pion pair. Our task was to reproduce this measurement for central collisions using UrQMD model.

2 Preparations

Data of simulated collisions of Au+Au at energy of 1.23A GeV at centrality of 0-10% were produced by UrQMD model. From all the particles included in the data, charged pions (saving both +/-) were separated for further use. For the total number of 6.5 million events only 10 - 30 charged pions were filtered for each event.

After this pion separation, the data were prepared to a format acceptable for CRAB.

CRAB (Correlation After Burner) is a program used to generate correlations from semi-classical transport codes. It reads points from phase space of final momentum and point of last interaction of simulated particles. Together with knowledge of impact parameters CRAB generates correlation functions. CRAB is able to implement full Coulomb interactions or strong interactions for an arbitrary number of partial waves, optionally interactions of Breit-Wigner form.

3 HBT radii

Using CRAB 3-dimensional correlation functions were counted in dependence of relative momentum of pair q for individual interval of mean transversal momentum of pair k_T (in range from 87.5 to 237.5 MeV in 25 MeV bins).

3.1 Fitting

Given correlation functions were fitted by Gaussian in form

$$C(q_o, q_s, q_l) = A \cdot e^{-(R_o^2 q_o^2 + R_s^2 q_s^2 + R_l^2 q_l^2)} + 1 \quad (35)$$

where R_o, R_s, R_l are parameters (HBT radii in out, side, long directions) we are looking for and A is a parameter. Once these parameters were established there is a need to multiply the values by $\hbar c$ in order to get the values in fermi units. Results of thus received HBT radii can be seen in Figure 1.

3.2 Scatter plot

To have a closer look how measured area looks like, scatter plot of number of particles in dependence on position in transversal plane was constructed. Firstly, vector of transversal momentum of a particle was turned to *out* direction

for all particles from simulated data set. After that, x position of the particles were boosted to the form $x - \beta_{\perp} t$ where $\beta = \frac{p_T}{p_0}$. As a result contour line histogram was constructed showing number of particles in dependence on their position in boosted transversal plane for every k_T bin.

4 Next steps

Next, positive charged pions shall be processed the same way and comparison with numerically counted variations shall be done.

5 Figures

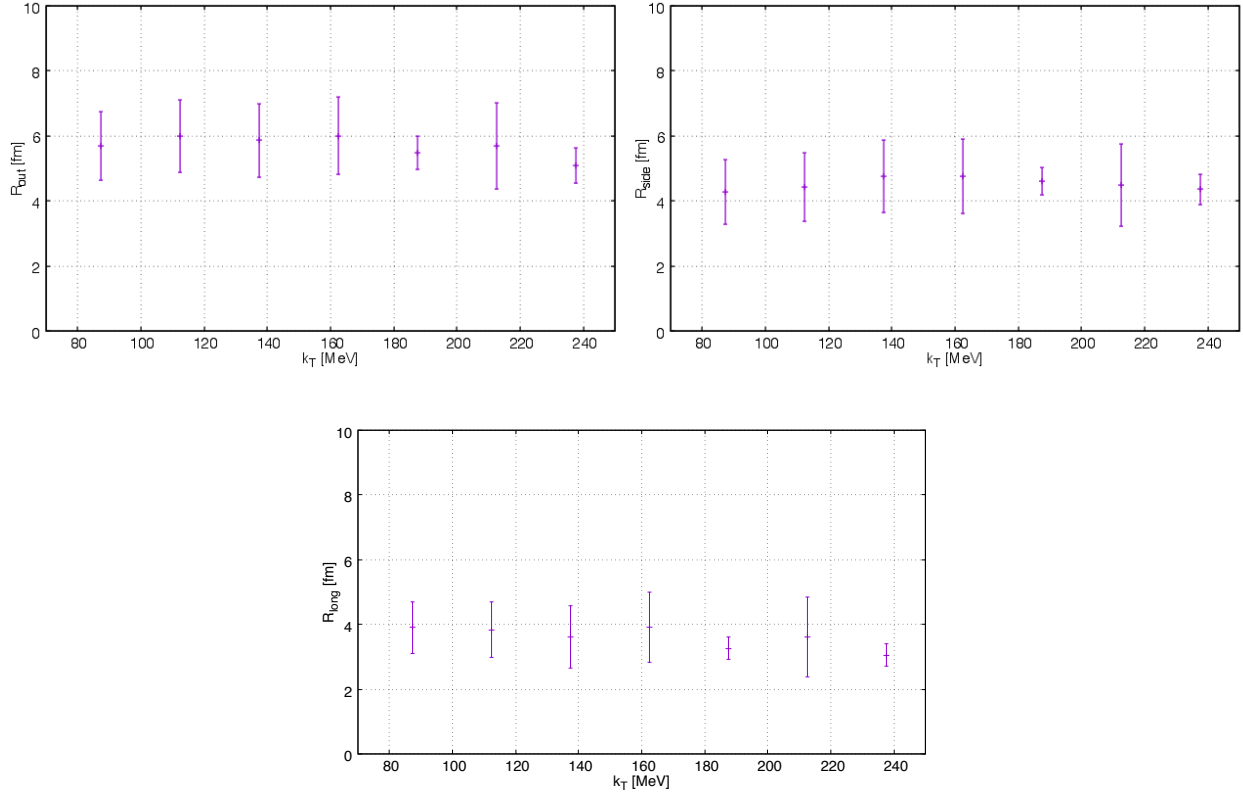


Figure 39: HBT radii received from fits in dependence on k_T in out, side and long directions

References

- [1] M. Bleicher, E. Zabrodin, C. Spieles, S.A. Bass, C. Ernst, S. Soff, H. Weber, H. Stocker and W. Greiner. Relativistic Hadron-Hadron Collisions and the Ultra-Relativistic Quantum Molecular Dynamics Model (UrQMD) In *J. Phys. G25 (1999) 1859–1896*.
- [2] S. A. Bass, M. Belkacem, M. Bleicher, M. Brandstetter, L. Bravina, C. Ernst, L. Gerland, M. Hofmann, S. Hofmann, J. Konopka, G. Mao, L. Neise, S. Soff, C. Spieles, H. Weber, L. A. Winkelmann, H. Stocker, W. Greiner, C. Hartnack, J. Aichelin and N. Amelin. Microscopic Models for Ultrarelativistic Heavy Ion Collisions In *Prog. Part. Nucl. Phys. 41 (1998) 225–370*.
- [3] http://theor.jinr.ru/wpcf2019/files/talks/06/14.talk_Dubna_060619.pdf [cit. 3.12. 2019]

COMPLEXITY OUT OF SIMPLICITY IN ATOMIC NUCLEI

Petr Veselý

There exist approximately 260 stable and 2500 unstable nuclear isotopes starting from the hydrogen up to superheavy elements with mass number $A \approx 290$ [1]. Nuclear structure varies significantly across the nuclear chart and, moreover, even the different energy states of one given isotope can correspond to very diverse structures – there are single-particle or collective excitations [2], rotational and vibrational states [3], so called pygmy [4] or breathing modes [5], phenomena such as backbending [6], wobbling [7] and others. This complexity of states and phenomena arises from simplicity. At least in principle we should be able to describe all mentioned above by studying the nuclear Hamiltonian, for which we only need the knowledge of mutual nucleon-nucleon interactions. However, such goal remains to be one of the most persisting and challenging problems of modern physics.

There are two main long existing obstacles to provide successful theoretical description of atomic nuclei including all their complex energy spectra and dynamical phenomena. First unsolved problem is proper description of interactions among nucleons themselves [8]. Second problem is solution of the nuclear many-body problem [9]. The nuclear many-body problem can be currently solved only approximately within various approaches.

Our considerations in the text above are based on a paradigm that satisfactory description of nuclear structure can be achieved by dividing this task into two separate steps. First, by constructing the potential among nucleons (possibly from the most fundamental theory of strong interactions, Quantum Chromodynamics), and second, by solving nuclear many-body problem in the language of nonrelativistic quantum mechanics with nuclear Hamiltonian constructed from the point-like nucleon potential. However, there arises also a question whether such paradigm is satisfactory approximation of physical reality. This makes the problem of theoretical description of nuclear structure even more demanding. On the other hand it calls for new effort and for search of creative new ideas within the theoretical nuclear physics.

References

- [1] *Interactive Chart of Nuclides*, <https://www.nndc.bnl.gov/nudat2/>
- [2] P. Ring, P. Schuck, *The Nuclear Many-Body Problem*, Springer-Verlag, (1980)
- [3] A. Bohr, B. R. Mottelson, *Nuclear Structure*, vol. II (Benjamin, New York, 1974).
- [4] D. Savran, T. Aumann, A. Zilges, *Prog. Part. Nucl. Phys.* 70, 210 (2013).
- [5] J. P. Blaizot, *Phys. Rep.* 64, 171 (1980).
- [6] P. Aguer, G. Bastint, J. P. Thibaudt, D. Barneoudt, J. Boutet, C. Foinx, *J. Phys. G: Nucl. Phys.* 3, 197, (1977).
- [7] N. Sensharma et al., *Phys. Rev. Lett.* 124, 052501 (2020).
- [8] R. Machleidt, D. R. Entem, *Phys. Rep.* 503, 1 (2011).
- [9] H. S. Köhler, *Nuclear Physics A* 928, 9 (2014).

HEAVY FLAVOR PHYSICS IN HEAVY-ION COLLISIONS

Jakub Češka

1 Introduction

Quarkonia are an unique probe for studying the properties of the quark-gluon plasma (QGP). The research presented in this proceeding focuses on the study of normalised multiplicity yield of the Υ meson in dependence on the normalised event multiplicity in proton-proton collisions at $\sqrt{s_{NN}} = 500$ GeV. The data was produced using various Monte Carlo event generators.

2 Quarkonia

Quarkonia are an bound state of a heavy quark and its corresponding antiquark ($c\bar{c}$ or $b\bar{b}$). They have the so-called 'hidden' charm or beauty. This refers to the fact, that while they contain either c or b quarks, their charm or beauty quantum numbers are zero.

The mechanism of production for quarkonia is not yet well understood. During the production multiple effects come into play. Quarkonia are created via the combination of hard scattering and non-perturbative hadronisation.

Several models intended to explain the event exist. The major models are:

- Color singlet model;
- Color octet model;
- Color evaporation model.

In proton-proton collisions, heavy quarks can be produced during multi-parton interactions. Multi-parton interactions are events, during which in proton-proton collision multiple partons are hard-scattered.

One important property of light quarkonia is their inability to decay via the strong nuclear force. For the quark-antiquark pair it is much more energetically beneficial to form their corresponding 'open' mesons ($D^0 = c\bar{u}$, resp. $B^+ = u\bar{b}$), than to form heavier quarkonia. The production suppression occurs mostly because the lighter quarkonia (e.g. J/Ψ , resp. Υ) are lighter, than double the mass of the corresponding open mesons, and thus the quark-antiquark pair cannot form the two open mesons.

Bottomonia are bound states of the b quark and its antiquark. One particularly interesting branch of the bottomonium family are the $\Upsilon(nS)$ states, as a QGP probe. This family has similar effects, as the J/Ψ has in QGP formalion. [1]

The lightest state, $\Upsilon(1S)$ is the lightest state of the branch and its mass is $m = (9460.30 \pm 0.26)$ MeV. [2] The next state, $\Upsilon(2S)$ has a mass of $m = (10026.26 \pm 0.31)$ MeV. [2] Both of these states were measured in their dielectron decay channel.

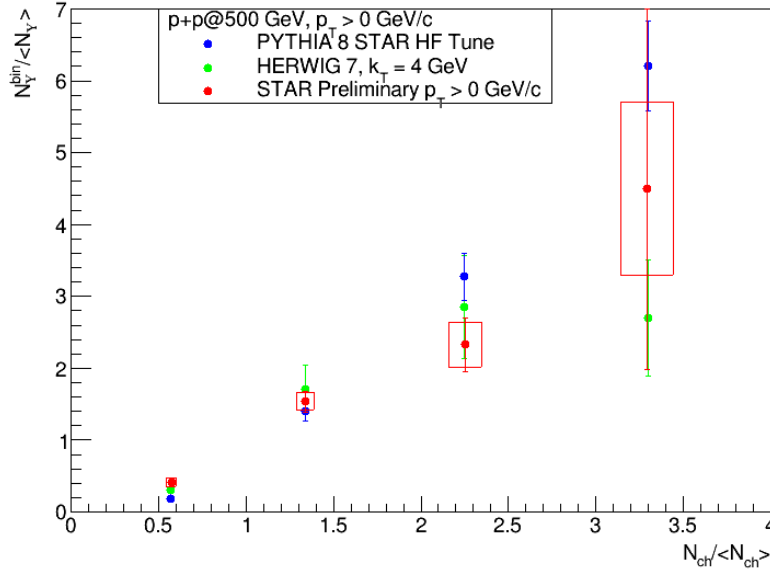


Figure 40: The dependence of normalised Upsilon yield on normalised event multiplicity for PYTHIA and Herwig data, compared to STAR preliminary data. [3]

3 Data generation

PYTHIA is an Monte Carlo event generator utilising the string hadronisation model. For a great benefit to this research, it allows for direct production of Υ mesons via a matrix element. Furthermore, it supports the selection of a particular decay channel for Upsilon.

Herwig is an Monte Carlo event generator using the cluster hadronisation model. Unlike PYTHIA, it does not support direct production of Υ mesons, only the production of $b\bar{b}$ pair. The Upsilon meson can be then created during hadronisation. It too supports the selection of a direct decay channel. One important parameter for Herwig is the 'JetKtCut:MinKT', which specifies the lower limit of a quark's momentum, when it emerges from a matrix element.

For both generators, minimum bias and signal events had to be generated. Minimum bias events serve for establishing a baseline multiplicity, whereas signal events contain the Upsilon mesons themselves. For all particles in both datasets, the cuts of $|\eta| < 1$ and $p_T > 200$ MeV/c were used.

4 Data analysis

The dependence of normalised Upsilon yield ($N_{\Upsilon} / \langle N_{\Upsilon} \rangle$) on normalised events multiplicity ($N_{ch} / \langle N_{ch} \rangle$) was measured.

Fig. (40) shows the dependence of normalised Upsilon yield on normalised event multiplicity for PYTHIA and Herwig data, compared to STAR preliminary data. [3] The Herwig event generator uses the value of 4 GeV/c for the *JetKtCut:MinKT* parameter. Fig. (41) shows the dependence of normalised Upsilon yield on normalised event multiplicity compared for $\Upsilon(1S)$ and $\Upsilon(2S)$ form data generated by PYTHIA event generator.

5 Conclusion

Monte Carlo event generators were used for generating data, in which the properties of Υ mesons in proton-proton collisions could be analysed. The analysed data shows, that when compared to real, preliminary data, the PYTHIA

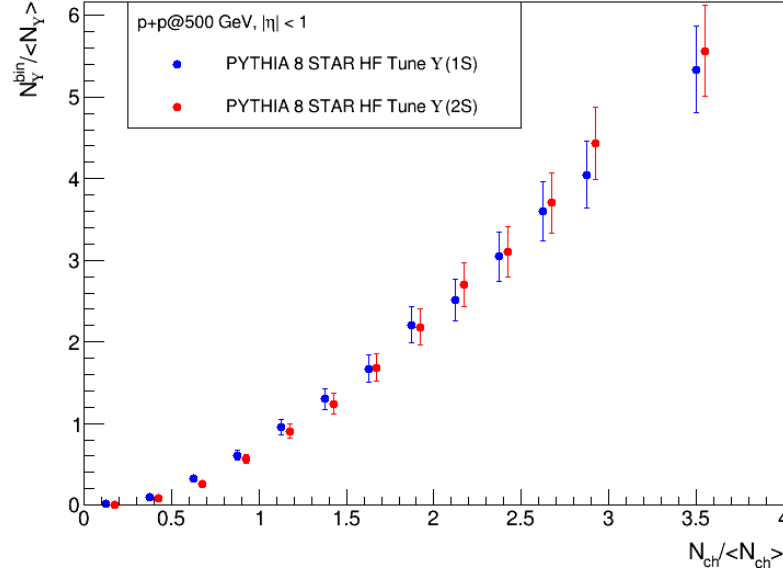


Figure 41: The dependence of normalised Upsilon yield on normalised event multiplicity compared for $\Upsilon(1S)$ and $\Upsilon(2S)$ from data generated by PYTHIA.

event generator correlates with the actual data. The data generated by the Herwig generator does not describe the trend well and more focus shall be laid on this part of the research. The data from PYTHIA furthermore supports the idea, that Upsilon mesons could be produced as a result of multi-parton interactions.

References

- [1] T. Matsui, H. Satz. J/Ψ Suppression by Quark-Gluon Plasma Formation In *Phys.Lett. B178 (1986) 416-422* (1986).
- [2] Particle Data Group (M. Tanabashi *et al.*). Review of Particle Physics In *Phys.Rev. D98 (2018) no.3, 030001* (2018-08-17).
- [3] L. Kosarzewski for the STAR collaboration. Measurements of Υ production in $p + p$ collisions at $\sqrt{s} = 500$ GeV with the STAR experiment At *Polish Workshop on Relativistic Heavy-Ion Collisions, Wroclaw 7.1.2018*.

NUCLEATION AND NANOPARTICLE GROWTH UNDER THE INFLUENCE OF IONIZING RADIATION BETA, GAMMA AND UV-VIS PHOTONS OF VARIOUS WAVELENGTHS

Karolína Šollová

1 Introduction

Nanoparticles are particles with a size of 1 to 100 nm, and compared to larger particles of the same composition, have much larger specific surface area per unit mass, which results in increase of reactivity. Nanoparticles are prepared by several physical and chemical methods, physical methods (top-down), leading to the formation of particles with different diameters. Bottom-up chemical methods use chemical reduction of metal salts, particle size and their unwanted agglomeration is controlled by stabilizers. Nucleation and nanoparticle growth are influenced by several factors including: concentration of nanoparticles in solution, pH of solution and presence of radiation during nucleation.

2 Preparation methods

One of the basic requirements for the preparation of nanomaterials is the size of nanoparticles in the material or solution and their uniformity. Therefore, two basic methods are used during preparation, namely:

- **physical methods - top-down**
 - mechanical breaking of materials into smaller particles up to nanoparticles
- **chemical methods - bottom-up**
 - preparation of nanoparticles from simple precursors at the molecular level
 - growth of nanoparticle structures into larger units (homogeneous or heterogeneous nucleation)

2.1 Stabilization

In most nanomaterials, unwanted agglomeration occurs, both in the final product and during preparation, therefore the particles need to be stabilized by the presence of chemicals. In a liquid medium nanoparticles are stabilized, for example, with surfactants or polymers with hydrophilic or hydrophobic groups. These stabilizers work on the principle of micelle formation. The hydrophilic or hydrophobic groups of polymers or surfactants in solution are oriented around the particle in such a way that the hydrophilic groups point outwardly and hydrophobic inwardly, thereby forming a netlike structure around the nanoparticle. The particles coated in surfactant or polymer do not agglomerate into larger units.

3 Size measurements

Nanoparticle size is measured using two main methods:

- observation and measurement of actual particle size (electron microscopes)
- methods based on the relation of particle behavior to its size

- less accurate methods that assume a spherical particle shape
- the measurement results in a particle size distribution in the sample

3.1 Electron microscopes - TEM/SEM

Electron microscopes display a sample in the form of a photograph.

- **scanning - SEM** - scanning the surface of a sample by electron beam
- **transmission - TEM**
 - the image is formed by a stream of electrons passing through the sample, therefore it is necessary to use very thin samples (10-500 nm)
 - individual particles can be observed and their actual size measured

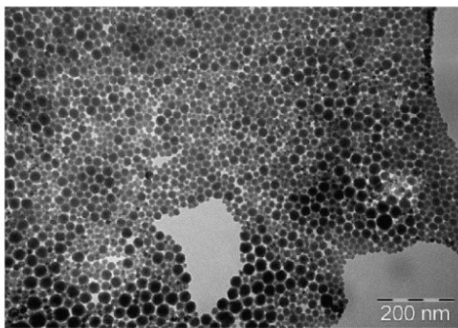
3.2 Dynamic light scattering - DLS

The dynamic light scattering (DLS) method is used to measure spherical particles in colloidal solutions. Particles in solution are irradiated with monochromatic light, which is reflected from their surface and is detected. Due to Brown's motion of the particles, Doppler shift occurs, causing the detected wavelength to be different from the original wavelength. From this wavelength difference, the particle size in the solution can then be determined, but not the size of one specific particle, which results in the size distribution of all particles in solution. The advantage of this method is the non-destructive measurement of particle sizes in solutions, the disadvantage is the inability to accurately measure the actual particle size, since only the hydrodynamic size is measured, which can be influenced by the presence of a stabilizer that can coat the particle.

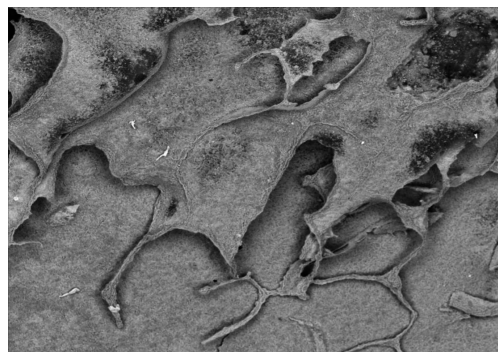
4 Preparation of Core-Shell nanoparticles Si(ZnS)

Core-shell nanoparticles are formed by a carrier particle (the core), which in this case are silicon nanoparticles, and shell with specific properties such as photocatalytic activity of zinc sulfide. In this chapter, step by step preparation will be described:

- **selection of suitable colloidal dispersion of Si**
 - the final size of core-shell particles depends on size of Si carrier particles (measured by DLS)
- **deposition of zinc acetate**
 - appropriate amount of zinc acetate is added to the dispersion
 - the desirable thickness of the future ZnS shell is given by the amount of zinc acetate dissolved in the dispersion of Si
- **rapid freezing and controlled vacuum freeze-drying**
 - the dispersion solution is rapidly frozen and then freeze-dried in low pressure chamber with temperature of -23°C , which enables self-organization of the sublimate into mostly single-layer lamellar structure of Si nanoparticles with a thin coating on zinc acetate, as shown in Figure ??.
- **exposition of the sublimate to gaseous hydrogen sulphide**
 - the lamellar product was exposed to gaseous hydrogen sulfide for 48 hours, so that the whole zinc acetate layer converted to the ZnS coating of Si particles, thus creating the shell
 - Figure ?? shows the surface structure of core-shell nanoparticles Si(ZnS) depicted by SEM



(a) TEM micrograph of lamellar structure of Si nanoparticles with a thin coating of zinc acetate after freeze-drying at -23°C . [2]



(b) SEM micrograph of lamellar structure of core-shell Si(ZnS) nanoparticles.[2]

5 Photocatalysis

Photocatalysis is an accelerated chemical photoreaction, which occurs on the surface of the catalyst. The photocatalyst creates electron-hole pairs, which generate free radicals able to execute further reactions (chain reaction principle). There are many different materials able to perform photocatalysis of different chemical compounds, for example the ZnS is able to decompose organic pollutants in presence of UV light.

6 Conclusion

The main course of my bachelor thesis is to examine the effects of different types of ionizing radiation on nucleation and growth of nanoparticles in conjunction with concentration of nanoparticles in solution, pH of the solution and the presence of stabilizers. And mainly how the dose of the radiation and exposure time affect agglomeration of nanoparticles during nucleation. To determine the results electron microscopy and DLS will be used.

References

- [1] A. Abenini, et al. A review on radiation-induced nucleation and growth of colloidal metallic nanoparticles. *Nanoscale research letters*, 8.1: 474., 2013.
- [2] R.Dvorský, P. Praus, L. Svoboda, D. Matýsek, T. Dropa, J. Trojková, K. Šollová. Preparation of Photocatalytic Silicon Core-shell Nanoparticles Covered by ZnS Shell in Solid-Gas Reaction. *Technical Proceedings of the 2014 NSTI Nanotechnology Conference and Expo, NSTI-Nanotech*, 1, pp. 94-96., 2014.
- [3] B. I. Kharisov, O. V. Kharissova, U. O. Mendez. Radiation synthesis of materials and compounds. *CRC press*, 2016.
- [4] J. Belloni Nucleation, growth and properties of nanoclusters studied by radiation chemistry: application to catalysis. *Catalysis today*, 113.3-4: 141-156., 2006.

MUONS IN COSMIC RAY SHOWERS

Antonín Kravka

1 Introduction - Cosmic rays, cosmic ray showers

Cosmic rays are high-energy particles traversing through space with energies ranging from 10^9eV to 10^{21}eV . These particles consist mainly from atomic nuclei - about 90% are protons (Hydrogen nuclei) and the remaining 10% consist from heavier nuclei and electrons. Since the flux of these particles depends on their energy, it is imperative to study the properties of ultra-high energy cosmic rays (or UHECRs - cosmic rays with energy above 10^{18}eV) using another phenomenon called "extensive air showers".

An air shower is a cascade of particles, that develops when a high energy particle enters the Earth's atmosphere. The particle interacts predominantly with nitrogen and oxygen nuclei, producing secondary particles like pions or kaons. These secondary particles interact (or decay) themselves, thus creating said cascade. Pions are created in 2:1 ratio charged to neutral (there are hundreds of pions created in a 10^{17}eV event), each contributing to a different part of the cascade. Neutral pions immediately decay into two photons, which then create e^+e^- pairs. These electrons and positrons further create photons through the process of bremsstrahlung, creating altogether the electromagnetic component of the cosmic ray shower. The charged pions continue to interact with nuclei in the atmosphere, until their energy is so low that they decay into muons and respective neutrinos.

For a high energy cosmic proton, the reactions look as follows:

$$p_{cr} + N \rightarrow p + N + \frac{1}{3}n\pi^0 + \frac{2}{3}n\pi^\pm, \quad (36)$$

where p_{cr} marks an incoming cosmic ray proton, N represents a nucleus in the atmosphere and n is a total number of pions created,

$$\pi^0 \rightarrow \gamma + \gamma, \quad \gamma + Z \rightarrow Z + e^+ + e^-, \quad e^\pm + Z \rightarrow Z + e^\pm + \gamma, \quad (37)$$

where Z marks the charge of a nucleus present to the reaction (to ensure that the momentum is conserved), and

$$\pi^\pm + N \rightarrow \pi^\pm + N + n\pi, \quad \pi^\pm \rightarrow \mu^\pm + \nu_\mu/\bar{\nu}_\mu. \quad (38)$$

2 Theoretical models

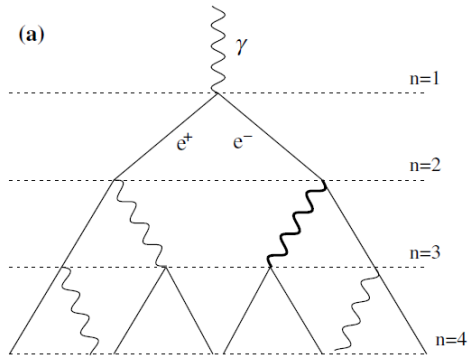
2.1 Heitler's model for electromagnetic cascades

Heitler's model is one of the most basic and very accurate theoretical models regarding electromagnetic cascades. It describes a cascade of particles of the same type with a radiation length of λ (see Fig. 1a). During each interaction, two new particles are created, each with half the parent particle's energy. After n interactions, there are 2^n particles, each with energy of $E = \frac{E_0}{2^n}$, where E_0 is the initial energy of an incoming particle. The number of particles grows, until it reaches a so-called critical energy E_C , when the particle's energy is too low for pair production or bremsstrahlung ($E_C = 85\text{MeV}$ in air). This energy indicates the maximum size of the shower, situated in an atmospheric depth of $X_{max} = \lambda \ln(\frac{E_0}{E_C})$. The model does not describe the decrease in the number of particles, since that would involve computing the energy losses of particles, which are better described by the theory of electromagnetic cascades.

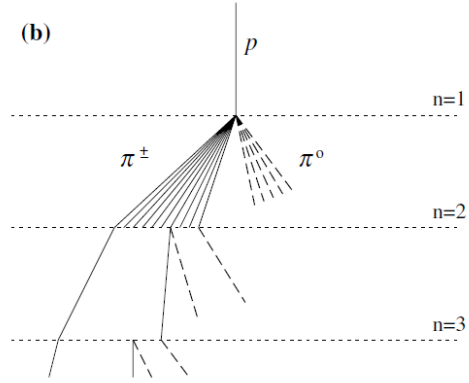
2.2 Generalized Heitler's model for hadronic cascades

The generalized Heitler's model describes the muonic and hadronic component of the cosmic shower. It divides the atmosphere into many layers of thickness $d = \lambda \ln(2)$, where λ is the interaction length of particles (see Fig. 1b). After one interaction length, a particle (for example proton) creates N_{ch} charged and $\frac{1}{2}N_{ch}$ neutral pions (the model does not include other particles as products). There is a valid approximation of $N_{ch} = 10$ for pion kinetic energies ranging from 1 GeV to 10 TeV, based on the fact that the majority of interactions in a shower occur with pion energies of order 100 GeV. While neutral pions initiate an electromagnetic cascade, the charged pions interact further. After n interactions, there are $(N_{ch})^n$ charged pions, each with energy of $E_\pi = \frac{E_0}{(\frac{3}{2}N_{ch})^n}$. After the pions reach a critical energy E_C , they decay into muons (which form the majority of particles we detect at the sea level) and neutrinos or antineutrinos.

The number of muons in the shower is derived as $N_\mu = (\frac{E_0}{E_C})^\beta$, where β ranges between the values 0.85 and 0.92, yielding 0.85 for multiplicity $N_{ch} = 10$ (derived from the model and Monte Carlo simulations of hadronic interactions).



(a) A depiction of an electromagnetic cascade [2].



(b) A depiction of a hadronic cascade [2].

Figure 42: Theoretical models of extensive air showers .

3 Simulation data

Fig. 2 shows a dependence of the mean number of muons detected at 1400 m above sea level (the altitude of the Pierre Auger Observatory) on the initial energy of cosmic protons and Fe nuclei. The nucleus nucleus models of interaction EposLhc, Qsjet01 and Sibyll23c were used for energies ranging from 10^{16} eV to 10^{19} eV.

4 The muon problem

In the data from the Pierre Auger Observatory, there is an abundance of muons comparing to simulations. This phenomenon is shown in Fig. 3, where we take the signal from ground detectors at the Observatory and show its dependence on $DX = X_{ground} - X_{max}$, where X_{ground} is the location of the detectors in atmospheric depth units (DX showing the phase of evolution of the shower). Comparing the data and simulations for protons and Fe nuclei, it is clearly shown, that there are more muons in the data than in the simulations. It is not yet known, what causes this discrepancy, if it is a continual inaccuracy made by the nucleus-nucleus models, or if it may be a new phenomenon regarding hadronic interactions.

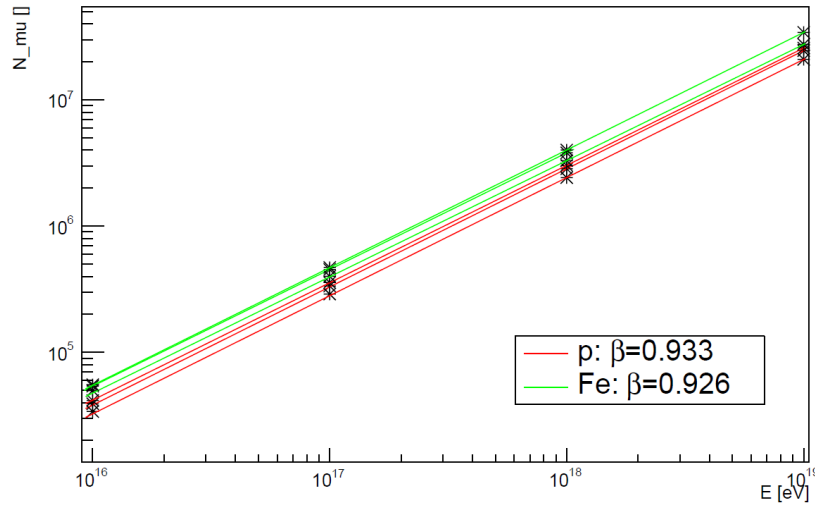


Figure 43: Dependency of the mean number of muons on the initial energy of incoming cosmic rays.

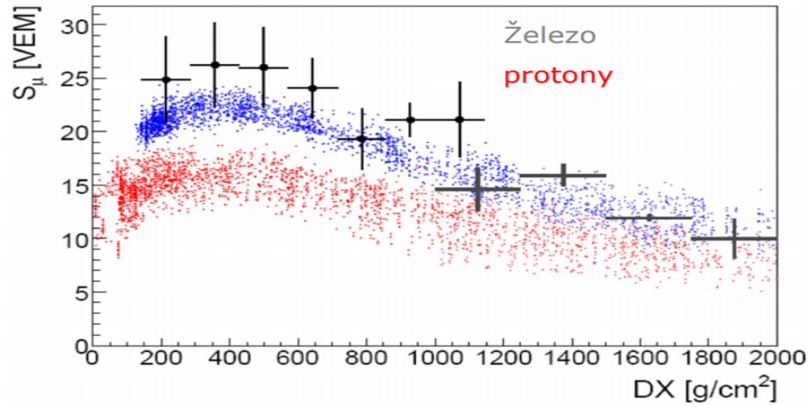


Figure 44: Dependency of the signal from ground detectors on DX [3].

5 Conclusion

The reader was introduced to the basic knowledge of cosmic rays, extensive air showers and basic theoretical models that describe the behavior of different components of a cosmic shower. The data from simulations regarding the number of muons detected at the Pierre Auger Observatory were presented. Regarding the muon problem at the Observatory, there is much hope in the ongoing upgrade of the Pierre Auger Observatory, the AugerPrime, that it will improve its ability to study hadronic interactions at ultrahigh energies, by separately measuring the hadronic and electromagnetic components of extensive air showers in the ground detectors.

References

- [1] A. Aab, et al. [Pierre Auger Collaboration]: Testing Hadronic Interactions at Ultrahigh Energies with Air Showers Measured by the Pierre Auger Observatory, *Phys. Rev. Lett.* 117, 192001, 2016.
- [2] J. Matthews: A Heitler model of extensive air showers, In *Astroparticle Physics* 22, pages 387–397, 2015.
- [3] P. Travníček: Kosmické záření a jeho detekční techniky,
URL: <https://www.fzu.cz/travnick/prednasky/KosmickeZareni/Kosmic.pdf>.

A STUDY OF RADIATION TOLERANCE OF THE MONOLITHIC SILICON DETECTORS

Václav Trličík

1 Magnetosphere

Earth's magnetosphere is an area around the world in which charged particles are affected by magnetic field. In reality it is a region where solar wind particles interact with magnetic field lines. From this idea it is clear that the shape of magnetosphere is in fact not a sphere but very irregular. On the side facing Sun the shape is compressed towards Earth, on the other side it can be very elongated such that it can reach several hundred thousand kilometers. The scheme of magnetosphere and general shape can be seen in Fig.45.

Earth's magnetic field is created when liquid metals (iron and nickel) in Earth's outer core are moving [2]. On the edges where the pressure of magnetic field and the pressure of solar wind equalize occurs very strong radioactive belts called Van Allen belts.

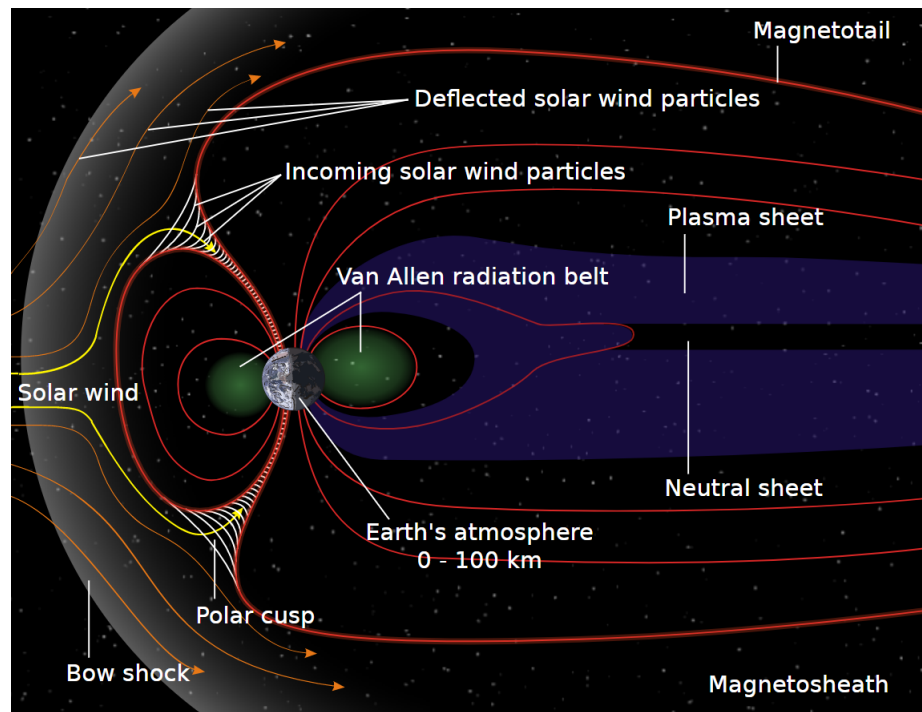


Figure 45: Diagram of Earth's magnetosphere. Picture from [1],NASA.

2 Van Allen radiation belts

Van Allen belts are toroidal-shaped radiation belts around the Earth. Although there are consistently only two of them, another one can be observed in special conditions. First two consist of the energetic charged particles predominantly

originating from the solar winds captured in Earth's magnetic field and from cosmic rays. Third one is mainly ultrarelativistic particles from ejected coronal mass captured in Earth's magnetic field. Scheme of radiation belts with respect to Earth is in Fig.46.

Inner radiation belt (also called proton belt) usually stretches from 650 to almost 10 000 km above the surface but during strong solar flares the lower bound can drop down to 100 km [5]. It contains mainly electrons and energetic protons (several hundreds MeV [6]). These high energy protons are the result of beta decay of neutrons created by the collisions of cosmic rays with the molecules of thermosphere and exosphere.

Outer radiation belt extends from 13 000 to 65 000 km and is made mainly of high energetic electrons (up to 10 MeV)[7].

The inner radiation belt can significantly damage orbiting satellites and is therefore important to study its composition and influences.

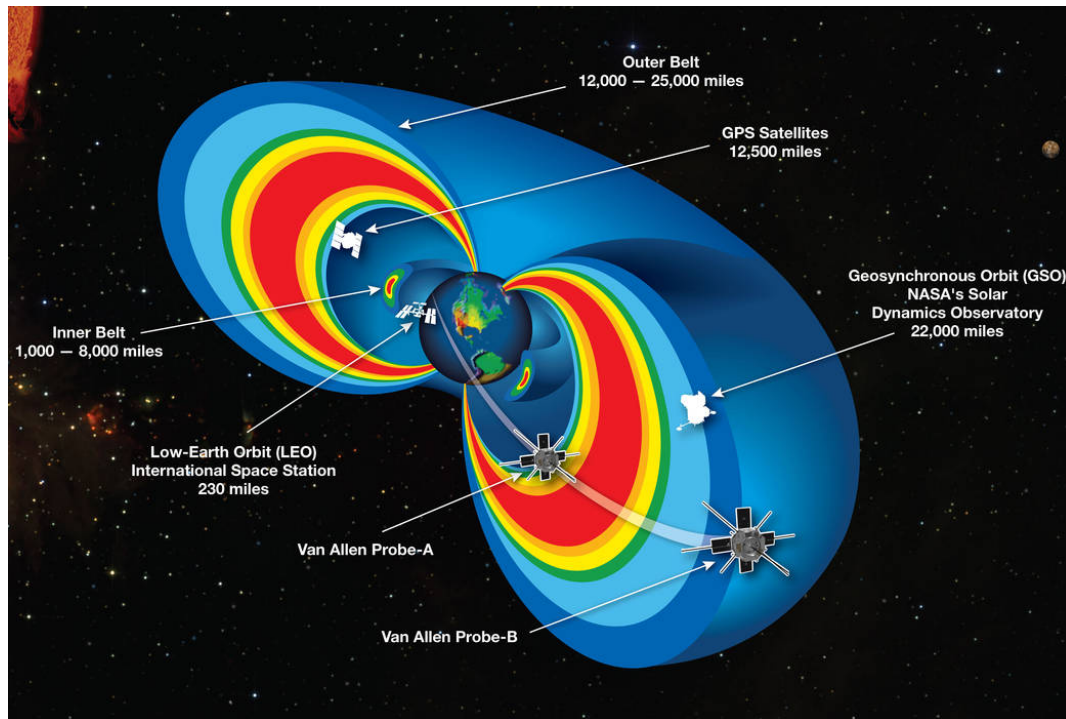


Figure 46: Scheme of Van Allen radiation belts. Picture taken from [8].

3 Sun

Our Sun is the biggest charged particles contributor. Nearby sunspots the Sun's magnetic field lines can generate loops, suddenly change its shape or tear apart. When some of this sudden change occurs the mass under the sunspot can be ejected from the surface to the space. This phenomenon is called coronal mass ejection. These charged particles (electrons, protons but also heavier nuclei) can reach several thousand kilometers per second [9] and if it crosses its path with Earth it can cause geomagnetic storms and satellites malfunctions.

References

- [1] Magnetosphere [online]. [cit. 2020-02-29]. <https://en.wikipedia.org/wiki/Magnetosphere>
- [2] HAUSOEL, A. et al. Local magnetic moments in iron and nickel at ambient and Earth's core conditions. Nat Commun 8, 16062 (2017) doi:10.1038/ncomms16062

- [3] NASA. (2019). Van Allen Probes Spot an Impenetrable Barrier in Space. [online] Available at: <https://www.nasa.gov/content/goddard/van-allen-probes-spot-impenetrable-barrier-in-space> [Accessed 12 Mar. 2019].
- [4] Science.nasa.gov. (2019). Van Allen Probes Discover a New Radiation Belt | Science Mission Directorate. [online] Available at: https://science.nasa.gov/science-news/science-at-nasa/2013/28feb_thirdbelt/ [Accessed 12 Mar. 2019].
- [5] Space Environment Standard ECSS-E-ST-10-04C | ESA Requirements and Standards Division. November 15, 2008, 59. Retrieved 12 Mar. 2019.
- [6] Freden, S. C., and White, R. S. (1960), Particle fluxes in the inner radiation belt, *J. Geophys. Res.*, 65(5), 1377–1383, doi:10.1029/JZ065i005p01377.
- [7] Brautigam, D. H., and Albert, J. M. (2000). Radial diffusion analysis of outer radiation belt electrons during the October 9, 1990, magnetic storm. *Journal of Geophysical Research: Space Physics*, 105, 291-309.
- [8] Zell, Holly. “Radiation Belts with Satellites.” NASA, NASA, 23 Mar. 2015, www.nasa.gov/mission_pages/sunearth/news/gallery/20130228-radiationbelts.html.
- [9] CLIVER, E. W., J. FEYNMAN a H. B. GARRETT. An estimate of the maximum speed of the solar wind, 1938–1989. *Journal of Geophysical Research*. 1990, 95(A10). DOI: 10.1029/JA095iA10p17103. ISSN 0148-0227. Dostupné také z: <http://doi.wiley.com/10.1029/JA095iA10p17103>

COLLECTIVE EFFECTS IN EMISSION OF A SET OF SINGLE-PHOTON EMITTERS

Daniel Babjak

One of the paramount tasks of experimental quantum optics studying the interaction of light and matter on the fundamental level of individual atoms corresponds to demonstration of the ability to efficiently collect optical radiation scattered from single atoms in free space. The presented work deals with possibilities of observation and control of fluorescence emitted from individual atoms and small atomic ensembles using the spatial directivity of light scattered on controllable spatial crystalline structures of positively charged ions.

Realistic collection optics allows for an efficient collection of fluorescence from relatively small spatial angles corresponding to a few percent of the entire emitted dipole radiation at a sufficient working distance. In the present work, we first theoretically analyze feasible directional patterns of the emitted radiation according to the position and orientation of the participating atomic dipoles and then optimize the detectable optical signal for realistic parameters of linear Paul traps. For simplicity, we consider the simplest arrangement of ions crystalized in linear 1D string. Considering the harmonic potential between the trap electrodes and the Coulomb interaction between the charged atoms, we include realistic distances between emitters. The change of the magnetic field in the trapping region allows for setting of the dipole orientations. By considering perfectly coherent scattering, we obtain an idealized pattern of directionality. Selection of the number of ions, frequency of the potential, and other trapping parameters, allow for maximization of the photon collection from linear ion strings.

Experimentally, we focus on the effective minimization of the kinetic energy and spatial jitter of ions using laser Doppler cooling, so that the dense ion structures could be kept in stable crystals. The resulting photon source is investigated by measuring the first and second-order correlation functions on emitted optical field. From the perspective of first order coherence, scattering on localized ions with residual thermal motion can be considered as scattering on thermally moving slits in a multi-slit Young experiment. Phase interference observation allows us to verify the critical condition for directional emission schemes corresponding to the spatial indistinguishability of the scattering emitters within the particular optical detection arrangement. With suitable settings of the excitation and detection parameters, we were able to observe an indistinguishable contribution from several ions to a single detection light mode.

The time resolution corresponding to a fraction of the lifetime of the excited state of the ion allows us to observe principally simultaneous emission from several emitters. In the optical detection arrangement corresponding to the Hanbury-Brown-Twiss scheme for measuring the intensity correlation functions at a single photon level, the photons are split into two detection arms with equal probability using an optical beam splitter. Our preliminary measurements of the second order correlation function in this arrangement on a light emitted by a set of several ions signify the directionality of the emission of light scattered indistinguishably and contributing to a single detection mode. Directionality is manifested by the measured bunching in the observed intensity correlation functions, which is in contrast to the results of measurements on the same sets of emitters but detected in a multi-mode arrangement. The corresponding theoretical description of the emission of contributing photon pairs suggests the emission of a second photon from entangled states of contributing ions prepared by first photon scattering, in close analogy to the schemes dealing with the optical generation of entangled pairs of atomic ensembles.

References

- [1] R. Loudon. *The quantum theory of light*. Oxford University Press, 2000.

- [2] M. A. Nielsen and I. L. Chuang. *Quantum computation and quantum information*. Cambridge University Press, 2010.

COHERENT J/ψ PHOTOPRODUCTION IN ULTRA-PERIPHERAL PB–PB COLLISIONS WITH ALICE AT THE LHC

Roman Lavicka

1 Introduction

Parton density functions (PDFs) of gluons and quarks inside the proton were precisely measured at small Bjorken- x at HERA [1]. The gluon PDF of heavy ions, particularly lead ions, can be investigated in a new kinematic range at the LHC facility.

A large flux of quasi-real photons accompanies the electrically charged accelerated lead ions at the LHC during Pb–Pb data taking giving us a possibility to use ultra-peripheral collisions (UPC) of lead ions to study photon-induced processes. Such collisions have the impact parameter larger than the sum of the nuclei radii and therefore, hadronic processes are suppressed and only photons remain to interact with a target nucleus. In the infinite momentum frame, when the quasi-real photon emitted by one of the lead ions approaches the vicinity of the target nucleus, it may fluctuate into a quark-antiquark pair. This pair interacts strongly with the target and creates a J/ψ meson, which is described here. If all nucleons in the target ion interact coherently as one body, this process is called coherent J/ψ photoproduction.

A measurement of the kinematics of the meson and the cross section of this process [2] is sensitive to the gluon distribution function of the nucleus [3]. The comparison of this cross section to that from photon–proton collisions provides information about the gluon shadowing in the nucleus [4]. Measurements of J/ψ photoproduction in UPC with the ALICE detector [5] allow us to reach Bjorken- x of 10^{-2} in forward and 10^{-3} in central rapidity.

2 J/ψ photoproduction in ultra-peripheral collisions

Collisions of two lead ion beams at $\sqrt{s_{NN}} = 2.76$ TeV were delivered to ALICE by the LHC during Run 1. ALICE investigated these decays in UPC in the forward rapidity region $-3.6 < y < -2.6$ and at mid-rapidity $|y| < 0.9$ [7]. The events described here have a clear signal consisting of J/ψ decaying into two leptons and nothing else. This lepton pair is measured at mid-rapidity with the ITS and the TPC and at forward rapidities with the muon spectrometer (for details see [5, 7]). The analysed samples correspond to an integrated luminosity of about $55 \mu\text{b}^{-1}$ and $23 \mu\text{b}^{-1}$, respectively. The measured cross sections are $d\sigma_{\text{coh } J/\psi}^{\text{UPC}}/dy = (1.00 \pm 0.18(\text{sta.})_{-0.26}^{+0.24}(\text{sys.})) \text{ mb}$ [8] and $d\sigma_{\text{coh } J/\psi}^{\text{UPC}}/dy = (2.38_{-0.24}^{+0.34}(\text{sta.}+\text{sys.})) \text{ mb}$ [9].

The measured cross sections are compared with theoretical models in Fig. 47. The measurement is correctly described with the AB-EPS09 model. In this model the nuclear shadowing prescription is based on the EPS09 parametrisation. Models, which incorporate strong shadowing, are below data. AB-MSTW08, a model which does not include any shadowing, is excluded by the measured data. Other models (see [8, 9] and references therein) overshoot the data at mid-rapidity.

Guzey, Kryshen, Strikman, and Zhalov used these cross sections [10] to put new constraints on the gluon nuclear distribution. They discuss the nuclear suppression factor S_{Pb} , which is defined in Eq. 39, where the measured UPC cross section is put into the nominator and a cross section calculated from the impulse approximation is used in the

denominator. The relation between Bjorken- x , the mass of the J/ψ , $M_{J/\psi}$ and the transferred energy $W_{\gamma p}$ is also shown there.

$$S_{Pb}(W_{\gamma p}) = \left[\frac{\sigma_{\gamma Pb \rightarrow J/\psi Pb}^{exp}(W_{\gamma p})}{\sigma_{\gamma Pb \rightarrow J/\psi Pb}^{IA}(W_{\gamma p})} \right]^{1/2}, x = \frac{M_{J/\psi}^2}{W_{\gamma p}^2}. \quad (39)$$

The impulse approximation is based on photon–proton data and then scaled by the integral over squared lead form-factor. The nuclear shadowing on the gluon distribution can be directly compared to the nuclear suppression factor $S_{Pb}(W_{\gamma p})$ at corresponding Bjorken- x values. The extracted S_{Pb} factor put in front the EPS09 parametrisation. It also agrees with the model based on the leading twist approximation (LTA).

During LHC Run 2, additional collisions at $\sqrt{s_{NN}} = 5.02$ TeV were measured in 2015. Higher energy, much higher integrated luminosity, improved trigger logic and a wider rapidity range due to new subdetectors increased the statistics of the recorded sample 50 times. The preliminary results on the coherent J/ψ cross section measurements are shown in Fig. 48. The increase in the sample size allows us to measure the cross sections in three forward rapidity regions. The results reaffirm the conclusion found in Fig. 47 about the EPS09 parametrisation. In addition, the LTA model, models based on the Color Glass Condensate (CGC) and GG-HS and GS-HS models using sub-nucleon degrees-of-freedom [11] are compared to data. Although it seems that CGC (LM IPSat) describes the best the measured data, the other models cannot be excluded in the forward rapidity region. A new more precise measurement in the central rapidity, which is underway, will decide between models.

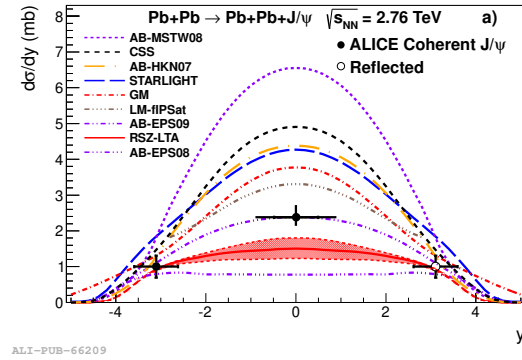


Figure 47: Cross sections at two different rapidities measured by ALICE during LHC Run 1 compared with different models. Taken from [8, 9].

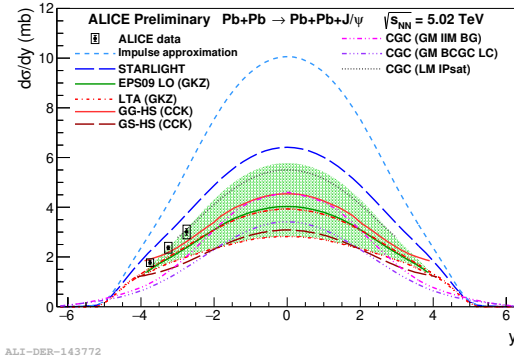


Figure 48: Preliminary results on cross section measurements by ALICE during LHC Run 2 in three forward rapidity regions compared with different models.

3 Conclusion and outlook

The results of Run 1 measurements of J/ψ photoproduction in UPC and peripheral lead–lead collisions by ALICE were presented. The calculations of nuclear suppression factors at different Bjorken- x based on measured data were also shown. Comparison of these measurements with different models and the calculations of S_{Pb} lying below unity are a direct evidence of moderate gluon shadowing in lead nucleus. However, the available data are not precise enough to distinguish amongst the different mechanisms used in the variety of presented models.

The new lead–lead collisions at $\sqrt{s_{NN}} = 5.02$ TeV were recorded in 2015 and are followed by additional measurement in Autumn 2018 in the so-called Run 2. These data are currently being analysed by ALICE and promise an increase of integrated luminosity up to $\sim 1 \text{ nb}^{-1}$ together with better systematic uncertainties.

4 Acknowledgement

This work has been partially supported by the grant 18-07880S of the Czech Science Foundation (GACR).

References

- [1] H. Abramowicz *et al.* [H1 and ZEUS Collaborations], Eur. Phys. J. C **75** (2015) no.12, 580 doi:10.1140/epjc/s10052-015-3710-4 [arXiv:1506.06042 [hep-ex]].
- [2] J. G. Contreras and J. D. Tapia Takaki, Int. J. Mod. Phys. A **30** (2015) 08, 1542012.
- [3] M. G. Ryskin, Z. Phys. C **57**, 89 (1993). ISSN:1431-5858 doi:0.1007/BF01555742
- [4] N. Armesto, J. Phys. G **32** (2006) R367 doi:10.1088/0954-3899/32/11/R01 [hep-ph/0604108].
- [5] K. Aamodt *et al.* [ALICE Collaboration], JINST **3** (2008) S08002.
- [6] J. G. Contreras, Phys. Rev. C **96** (2017) 015203 doi:10.1103/PhysRevC.96.015203
- [7] B. B. Abelev *et al.* [ALICE Collaboration], Int. J. Mod. Phys. A **29** (2014) 1430044 doi:10.1142/S0217751X14300440 [arXiv:1402.4476 [nucl-ex]].
- [8] B. Abelev *et al.* [ALICE Collaboration], Phys. Lett. B **718** (2013) 1273 doi:10.1016/j.physletb.2012.11.059 [arXiv:1209.3715 [nucl-ex]].
- [9] E. Abbas *et al.* [ALICE Collaboration], Eur. Phys. J. C **73** (2013) no.11, 2617 doi:10.1140/epjc/s10052-013-2617-1 [arXiv:1305.1467 [nucl-ex]].
- [10] V. Guzey, E. Kryshen, M. Strikman and M. Zhalov, Phys. Lett. B **726** (2013) 290 doi:10.1016/j.physletb.2013.08.043 [arXiv:1305.1724 [hep-ph]].
- [11] J. Cepila, J. G. Contreras and M. Krelina, Phys. Rev. C **97** (2018) no.2, 024901 doi:10.1103/PhysRevC.97.024901 [arXiv:1711.01855 [hep-ph]].
- [12] J. Adam *et al.* [ALICE Collaboration], Phys. Rev. Lett. **116** (2016) no.22, 222301 doi:10.1103/PhysRevLett.116.222301 [arXiv:1509.08802 [nucl-ex]].
- [13] S. Klein and J. Nystrand, Phys. Rev. C **60** (1999) 014903 doi:10.1103/PhysRevC.60.014903 [hep-ph/9902259].

NONLINEAR DYNAMICS

Tomáš Novák

1 Continuous dynamical systems

Dynamical system is a collection of variables $x_1(t), x_2(t), \dots, x_n(t)$, which depend on the external parameter $t \in \mathbb{R}$ (usually time) and evolution laws are given as a system of first order differential equations. In contrast, discrete dynamical systems has evolution laws in form of recurrence relations.

In general any n^{th} -order scalar differential equation

$$\frac{d^n \xi}{dt^n} = g(t, \xi, \frac{d\xi}{dt}, \dots, \frac{d^{n-1}\xi}{dt^{n-1}})$$

can be transformed into system of $n + 1$ first order differential equations by substitution

$$x_1 = \frac{d^{n-1}\xi}{dt^{n-1}}, \quad x_2 = \frac{d^{n-2}\xi}{dt^{n-2}}, \quad \dots, \quad x_{n+1} = \xi.$$

Then we can write the system of first order differential equations in compact form

$$\dot{\mathbf{x}} = \mathbf{f}(\mathbf{x}, t), \text{ where } \dot{x}_i = f_i(\mathbf{x}, t). \quad (40)$$

If vector function $\mathbf{f}(\mathbf{x}, t)$ is continuously differentiable on $[t_0 - a, t_0 + a] \times D$ ($D \subset \mathbb{R}^n$), then it satisfies *Lipschitz condition*:

$$\|\mathbf{f}(\mathbf{x}_1, t) - \mathbf{f}(\mathbf{x}_2, t)\| \leq L \|\mathbf{x}_1 - \mathbf{x}_2\|,$$

where $\mathbf{x}_1, \mathbf{x}_2 \in D \subset \mathbb{R}^n$ and L is Lipschitz's constant. This condition implies the existence and uniqueness of the solution to the *Cauchy problem*:

$$\dot{\mathbf{x}} = \mathbf{f}(\mathbf{x}, t), \quad \mathbf{x}(t_0) = \mathbf{x}_0, \quad (41)$$

where $\mathbf{x}(t_0) = \mathbf{x}_0$ are an initial conditions. The solution $\mathbf{x}(t)$ of the Cauchy problem (41) depends on the initial conditions \mathbf{x}_0 , so we are explicitly labeling the solution $\mathbf{x}(t)$ as $\mathbf{x}(t, \mathbf{x}_0)$ and calling it *orbit* for initial conditions \mathbf{x}_0 . Now the system of equations (40) is called dynamical system on the *phase space* $D \subset \mathbb{R}^n$.

1.1 Autonomous dynamical systems, critical point and bifurcation

Let's now assume that the vector function $\mathbf{f} = \mathbf{f}(\mathbf{x})$ is not explicit function of time t , then the dynamical system is called *autonomous*. For an autonomous dynamical system we can define *phase portrait* as

$$P = \{\mathbf{x}(t, \mathbf{x}_0) | \mathbf{x}_0 \in D \text{ and } t \in \mathbb{R}\}.$$

A *critical point (stationary point)* \mathbf{x}_s of autonomous dynamical system satisfies $\mathbf{f}(\mathbf{x}_s) = 0$, so for Cauchy problem (41) with $\mathbf{x}_0 = \mathbf{x}_s$ the solution is $\mathbf{x}(t, \mathbf{x}_s) = \mathbf{x}_s$ for all t .

A *bifurcation* of a dynamical system $\dot{\mathbf{x}} = \mathbf{f}(\mathbf{x}, \varepsilon)$ at parameter $\varepsilon = b$ is a change of *topology* of the phase portrait, while changing the parameter ε and reaching the value b .

1.2 Linearization of dynamical system

Taylor series for vector function $\mathbf{f}(\mathbf{x})$ at a critical point \mathbf{x}_s can be expressed as

$$\begin{aligned}\dot{\mathbf{x}} &= \mathbf{f}(\mathbf{x}_s + \mathbf{dx}) = \mathbf{f}(\mathbf{x}_s) + \mathbb{A}\mathbf{dx} + \dots \\ \dot{\mathbf{x}} &= \mathbb{A}\mathbf{dx} + \mathbf{g}(\mathbf{x}_s + \mathbf{dx}),\end{aligned}\tag{42}$$

where vector function $\mathbf{g}(\mathbf{x})$ satisfy condition

$$\lim_{\mathbf{x} \rightarrow \mathbf{x}_s} \frac{\|\mathbf{g}(\mathbf{x})\|}{\|\mathbf{x} - \mathbf{x}_s\|} = 0.$$

Then the vector function $\mathbf{f}(\mathbf{x})$ near the critical point \mathbf{x}_s can be approximated as

$$\dot{\mathbf{x}} = \mathbf{f}(\mathbf{x}_s + \mathbf{dx}) \simeq \mathbb{A}\mathbf{dx}.\tag{43}$$

Linearized dynamical system (43) will help us examine dynamical behaviour of original generally nonlinear system generally nonlinear (42) near critical point \mathbf{x}_s .

From another point of view we can also think of the dynamical system (42) as a perturbed case of the linear dynamical system (43), so

$$\dot{\mathbf{x}} = \mathbb{A}\mathbf{dx} + \varepsilon\mathbf{g}(\mathbf{x}_s + \mathbf{dx}),\tag{44}$$

where $\varepsilon > 0$ is a parameter.

1.3 Linear dynamical system and stability of critical points

Cauchy problem for a linear dynamical system can be written as

$$\dot{\mathbf{x}} = \mathbb{A} \cdot \mathbf{x}, \quad \mathbf{x}(t_0) = \mathbf{x}_0,\tag{45}$$

where $\mathbb{A} \in \mathbb{R}^{n,n}$ is a regular matrix. To solve (45) we need to find an eigenvalues λ_l and an eigenvectors $\boldsymbol{\eta}^l$ of the matrix \mathbb{A} . Using an ansatz $\mathbf{x}(t) = \sum_{l=1}^n c_l \boldsymbol{\eta}^l(t)$ we see that

$$\dot{\mathbf{x}} = \mathbb{A} \cdot \mathbf{x} \rightarrow \sum_{l=1}^n c_l \dot{\boldsymbol{\eta}}^l = \mathbb{A} \cdot \sum_{l=1}^n c_l \boldsymbol{\eta}^l = \sum_{l=1}^n c_l \lambda_l \boldsymbol{\eta}^l.\tag{46}$$

because eigenvectors are orthogonal we get n equations

$$\dot{\boldsymbol{\eta}}^l = \lambda_l \boldsymbol{\eta}^l \implies \boldsymbol{\eta}^l(t) = e^{\lambda_l(t-t_0)} \boldsymbol{\eta}^l(t_0).\tag{47}$$

Solution to the Cauchy problem (45) is

$$\mathbf{x}(t) = \sum_{l=1}^n c_l \boldsymbol{\eta}^l(t) = \sum_{l=1}^n c_l e^{\lambda_l(t-t_0)} \boldsymbol{\eta}^l(t_0).\tag{48}$$

Analyzing $\lambda_l = a_l + ib_l$ we can determine behaviour of the dynamical system in a direction $\boldsymbol{\eta}^l$, if

- $a_l \leq 0$ and $b_l = 0$ then in the direction $\boldsymbol{\eta}^l$ the point $\mathbf{x}_s = \mathbf{0}$ is stable.
- $a_l > 0$ and $b_l = 0$ then in the direction $\boldsymbol{\eta}^l$ the point $\mathbf{x}_s = \mathbf{0}$ is unstable.
- $a_l = 0$ and $b_l \neq 0$ then in the direction $\boldsymbol{\eta}^l$ solution $\mathbf{x}(t)$ oscillates.

Phase portrait near critical point is characterized by combination of eigenvalues λ_l .

Correspondence of dynamical behaviour of linear and nonlinear system depends on real parts of $\lambda_l \in \sigma(\mathbb{A})$. If $\forall l \in \hat{n}; \text{Re}(\lambda_l) \neq 0$ then the correspondence is fulfilled. If the previous condition is not met, we have to use techniques such as *center manifold reduction*, find *Lyapunov function*, etc.

2 Deterministic chaos in Hamiltonian systems

If there exists a scalar function $H = H(\mathbf{q}, \mathbf{p})$ such that equations of motion can be obtained $\forall i \in \hat{n}$

$$p_i = -\frac{dH}{dq_i}; \quad q_i = \frac{dH}{dp_i}, \quad (49)$$

function H is a Hamilton function and the system of equations (49) is the Hamiltonian dynamical system. Nonlinearity can be added to the system through the parameter ε as

$$H = H_{lin} + \varepsilon H_{per} \implies \dot{\mathbf{x}} = \mathbb{A}\mathbf{x} + \varepsilon \mathbf{f}(\mathbf{x}). \quad (50)$$

We can see that nonlinearity in H_{per} is transferred into equations of motion as the derivation is a linear operation.

Term H_{per} can contain a nonlinear dependencies between the generalized coordinates. As the parameter $\varepsilon \neq 0$ rises we may see changes in the phase portrait of the dynamical system as a bifurcation takes place and in some parts of phase portrait phenomenon called *deterministic chaos* can appears. Also for Hamiltonian systems we usually set $H = E$, where $E > 0$ is a constant, then E is another parameter for possible bifurcation.

Deterministic chaos can occurs in a continuous nonlinear dynamical system with more than three degrees of freedom. It is characterized by high sensitivity to change in initial conditions, exponential divergence of near orbits, orbits are captured on a complicated subset of \mathbb{R}^n called *strange attractor* and equations of motion are *non-integrable*.

2.1 KAM theorem

Kolmogorov-Arnold-Moser theorem qualitatively treating transition of periodic and quasiperiodic orbits as a nonlinear perturbation term is added into a linear dynamical system. It states that quasiperiodic orbits *survive* and get slightly deformed, but other periodic orbits changes into a set modeled by fractal *Cantor set*. Also as the energy of a Hamiltonian system increases, the perturbation term becomes more significant. So as we increase parameter $H = E$ or ε in (50) more of Cantor-like sets appears. As the parameter $E \rightarrow 0$ or $\varepsilon \rightarrow 0$, then Lebegues measure of the Canto-like set tends to zero.

For Hamiltonian nonlinear system:

$$\begin{aligned} H &= \frac{1}{2}(q_1^2 + p_1^2) + \frac{1}{2}(q_2^2 + p_2^2) + \varepsilon(q_1^2 q_2 - \frac{1}{3}q_2^3) \\ \implies \dot{p}_1 &= -q_1 - \varepsilon 2q_1 q_2 \\ \dot{q}_1 &= p_1 \\ \dot{p}_2 &= -q_2 + \varepsilon(q_2^2 - q_1^2) \\ \dot{q}_2 &= p_2, \end{aligned} \quad (51)$$

we choose $\varepsilon = 1$. We produced so called *Poincaré section* (intersection with a plane) on Fig. (49) of phase portrait of the dynamical system (51) for two values of energies $E = 1/12$ and $E = 1/8$ by numerically solving the system (51). It is easy to see, that desintegration of the periodic orbits into Cantor-like set takes place, and so phenomenon of deterministic chaos occurs.

References

- [1] VERHULST F., *Nonlinear Differential Equations and Dynamical Systems*. Berlin. Springer-Verlag. 1989.
- [2] HORÁK, J., L. KRLÍN, A. RAIDL. *Deterministický chaos a jeho fyzikální aplikace*. Praha. Academia. 2003.

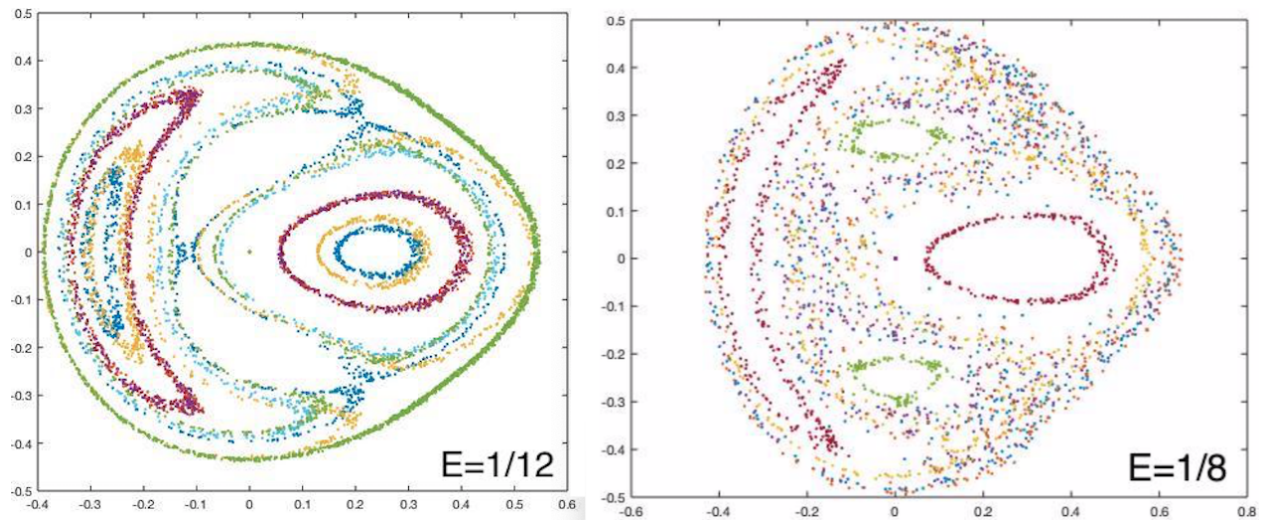


Figure 49: Poincaré section of system (51) for two values of energy $E = 1/12$ and $E = 1/8$.

SYNTHESIS OF ELEMENTS

Pavel Špíšek

1 Introduction

My presentation is separated into three main parts. Firstly, I will say a few words about nucleosynthesis right after the Big Bang and why it cannot explain, how heavier elements were made. Then I will describe what led to discovery of processes, which can explain the rise of heavier elements. The last part focuses on nuclear reactions in stellar environment.

2 Big Bang Nucleosynthesis

According to experiments and measurements conducted in the first half of 20th century it was very likely that our universe was previously in a state with larger density and temperature than it is now. There was a much greater number of high energy photons than neutrons and protons. In this environment of very high temperature (about 10^{12} K) processes



proceeded in both ways. At this temperature the neutron decay



can be neglected, because the half-life of a neutron is just under 15 minutes. Reactions such as $p + n \longrightarrow d + \gamma$ were also possible. However, due to relatively low binding energy of deuterium (2,22 MeV) and large number of high energy photons, deuterons are almost immediately destroyed and cannot participate in other reactions. As the temperature decreases approximately to 10^9 K the ratio of neutrons and protons in the environment freezes. The neutron decay (53) now begins to play a significant role affecting the n/p ratio which changes approximately to 1/7. After the mean energy of photons drops under the binding energy of deuterons, reactions that increase nucleon numbers may occur (β decay, nuclear reactions of light nuclides). However, this process of increasing nucleon numbers is limited. There are no stable nuclides with nucleon numbers 5 and 8, therefore this process cannot explain the origin of heavier elements than ${}^7\text{Li}$. In 1957, two papers were published independently (B2FH and Cameron). They propose a solution to this problem, suggesting that heavier elements can be produced in stellar environments due to nuclear reactions.

3 Description of stars

As mentioned before, only lighter elements could arise from the Big Bang nucleosynthesis, therefore there have to be other processes which can explain origin of heavier elements. These processes are reflected in abundance of elements and isotopes in the universe.

Hertzsprung-Russel diagram To learn about stars, it is useful to define Hertzsprung-Russel diagram. On the x axis of the diagram is the surface temperature and luminosity is on the y axis. It is significant, because it splits stars into categories with similar properties. The diagram can be seen in the Figure 50. The group of stars located on the diagonal of the H-R diagram is very eminent. These stars are called the main sequence stars and can be described as the "young" stars, young meaning that they are in the first phase of burning fuel (hydrogen burning). Our closest

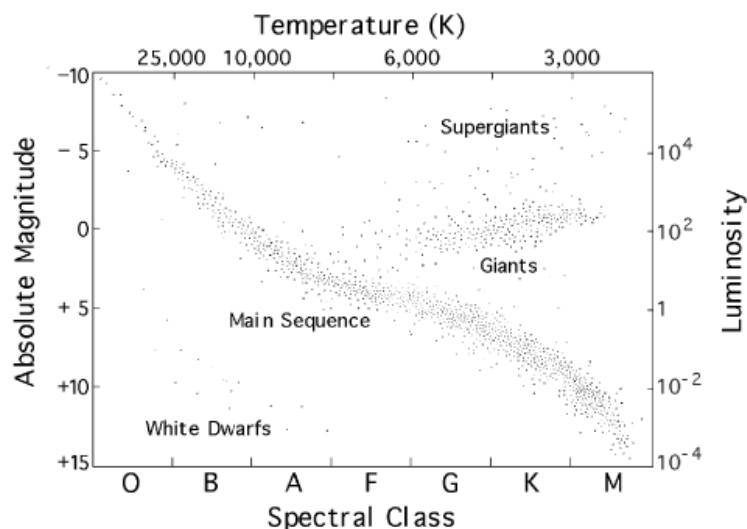


Figure 50: Hertzsprung-Russell diagram splits star to groups with similar properties. Figure shows Main Sequence, the early phase of stars, and later phases white dwarfs, giants, supergiants.

star, the Sun, also belongs in the main sequence. Other groups shown in the Figure 50 are white dwarfs, giants and supergiants. Those are later phases of the life of a star.

The evolution of a star throughout time is a topic on its own, but in a nutshell it is possible to say that stars arise from gas clouds that consist mainly of hydrogen and helium. The clouds shrink when gravitational forces become stronger than the thermal energy of each molecule. At first, the thermal energy, that caused by gravitational forces, is radiated out of the cloud. Then the cloud becomes more and more non-transparent and its energy is preserved inside. The temperature rises to approximately 10^7 K (everything in the life of a star heavily depends on its initial mass). In this moment nuclear reactions can be considered the main source of the star's energy. This first phase is called "hydrogen burning" and it means that four atoms of hydrogen fuse to one atom of helium. It is also this particular moment when star can be seen in H-R diagram on the main sequence. Stars with greater initial mass have greater surface temperature and luminosity. However, because of their large energy requirements, they burn their fuel much faster and move on to the next phase called "helium burning" faster.

4 Nuclear reactions in stellar environment

The pp chain and the CNO cycle are very significant nuclear reactions in the stellar environment. Both reactions take four hydrogen atoms and transform them into one helium atom. We refer to this process as "hydrogen burning", although it is not really burning as we know it. The pp chain is not actually a single reaction but three sequences of nuclear reactions. Every reaction in every sequence was studied in detail. It is interesting that some of the reactions do not have the largest cross section. However, one also needs to consider the reaction rates and the abundances of nuclides. The CNO cycle also fuses four atoms of hydrogen into one helium atom. However, it does not fulfill the condition mentioned above – that high abundance is crucial for processes to happen. In this case elements C, N, O are the catalysts and for example their relative abundance to protons is very low. It means that in with relatively low abundance of these elements in stellar environment it is possible to have processes which significantly contribute to burning of hydrogen.

References

- [1] C.E.Rolfs, *Cauldrons in the Cosmos*, 2005
- [2] C. Iliadis, *Nuclear Physics of Stars*, 2007